PERFORMANCE ENHANCEMENT OF MICROMACHINED THIN-FILM PIEZOELECTRIC-ON-SILICON LATERAL-EXTENSIONAL RESONATORS THROUGH SUBSTRATE AND TETHER MODIFICATIONS

By

BRANDON PAUL HARRINGTON

Bachelor of Science in Computer Engineering
Georgia Institute of Technology
Atlanta, Georgia
2005

Master of Science in Electrical and Computer Engineering
Georgia Institute of Technology
Atlanta, Georgia
2008

Submitted to the Faculty of the
Graduate College of the
Oklahoma State University
in partial fulfillment of
the requirements for
the Degree of
DOCTOR OF PHILOSOPHY
December, 2013

PERFORMANCE ENHANCEMENT OF

MICROMACHINED THIN-FILM PIEZOELECTRIC-ON-

SILICON LATERAL-EXTENSIONAL RESONATORS

THROUGH SUBSTRATE AND TETHER

MODIFICATIONS

Thesis Approved:

Reza Abdolvand

Thesis Adviser

John M. Acken

Chris Hutchens

Jerzy Krasinski

Raman P. Singh

ACKNOWLEDGMENTS

The doctoral journey has been quite an adventure. I would like to thank my loving wife, Barbara Faith Garlington, for her constant support through the process.

Acknowledgements reflect the views of the author and are not endorsed by committee members or Oklahoma State University.

Name: BRANDON PAUL HARRINGTON

Date of Degree: DECEMBER, 2013

Title of Study: PERFORMANCE ENHANCEMENT OF MICROMACHINED THIN-FILM PIEZOELECTRIC-ON-SILICON LATERAL-EXTENSIONAL RESONATORS THROUGH SUBSTRATE AND TETHER MODIFICATIONS

Major Field: ELECTRICAL ENGINEERING

Abstract: Electromechanical resonators have formed the basis of telecommunication circuits for decades through the use of quartz crystal oscillators. Recently, MEMS resonators-based oscillators have become a possible replacement in selective applications for quartz crystal oscillators. The focus of this work is to show the performance of micromachined thin-film piezoelectric-on-silicon resonators can be improved through the design of the substrate-tether interaction. In lower frequency devices, resonators exhibit a significant increase to quality factors through the application of acoustic reflectors etched into the surrounding substrate. Simulation shows that the acoustic reflectors can limit the anchor loss for these devices and experimental results confirm efficacy. For higher frequency resonators, multiple tethers show greater quality factors, lower motional impedance, and improved power handling capabilities.

TABLE OF CONTENTS

ACKNOWLEDGMENTS iii
LIST OF TABLES vii
LIST OF FIGURES viii
NOMENCLATURE xiv
CHAPTER I 1
INTRODUCTION 1
CHAPTER II 3
REVIEW OF LITERATURE 3
Review of recent micromachined piezoelectric resonators publications 7
CHAPTER III 9
METHODOLOGY 9
THEORY 16
Loss 20
CHAPTER V 24
FABRICATION 24
CHAPTER VI 35
IN-PLANE ACOUSTIC REFLECTORS 35
Simulation 40
Acoustic Reflector Results 49
Viscous and squeeze film damping in thin-film piezoelectric-on-silicon resonators with in-plane acoustic reflectors 59
CHAPTER VII 61
MULTIPLE TETHER PAIRS 61
Frequency stability of multi-tether devices. 67
CHAPTER VIII 68

POWER HANDLING OF MULTIPLE TETHER PAIRS 68
CHAPTER IX 80
CONCLUSION 80
Future work 81
CHAPTER X 82
APPENDICES 82
A. Model SEM images of fabricated thin-film piezoelectric-on-silicon (TPoS) resonators. 83
B. Power dissipated and gain compression Python code 88
C. Frequency shift PHP code 95
Chapter XI 100
BIBLIOGRAPHY 100

LIST OF TABLES

Table 1. Piezoelectric transduced micromachined resonators targeting the real-time clock application space sorted by f Q product figure of merit. 7

Table 2. $Q_{unloaded}$ results for 27MHz devices. 50

Table 3. Average measured unloaded quality factors for 110MHz resonators. 57

Table 4. $Q_{unloaded}$ results for third harmonic 110MHz, lateral-extensional, TPoS resonators with tether length of 3λ/8.. 58

LIST OF FIGURES

Figure 1: Cady's frequency standard used two quartz plates to excite a 10cm steel bar for 11km wavelength.. 4

Figure 2. A schematic of a micromachined, lateral-extensional (motion in the y-direction), thin-film piezoelectric-on-silicon resonator. 10

Figure 3. Simulated, deformed fundamental (a) and third order harmonic (b) lateral extensional modes. Blue color denotes regions of contraction (negative strain) while red shows regions of expansion (positive strain) along the axis of vibration (x-axis). 11

Figure 4. A frequency response of the magnitude of S_{21} denoting key resonator parameters....... 12

Figure 5. Manual wafer-level RF probe station. 13

Figure 6. DUT actively being probed by two GSG probes. 14

Figure 7. Janis vacuum probe station for RF measurements 15

Figure 8. Mechanical representation of a mass-spring-damper system under a force, F. 17

Figure 9. Generalized piezoelectric resonator with electric portions (yellow), transduction (green) and a mechanical resonance portion (blue). 18

Figure 10: One port resonator.. 19

Figure 11: Two port resonator with its two parasitic shunt capacitors. 19

Figure 12: Blank SOI wafer (thickness not to scale on any of the schematics) 25

Figure 13. SOI wafer after sputtered films have been deposited 25

Figure 14: Wafer after top electrode dry etch.. 27

Figure 15: Wafer after aluminum nitride wet etch. 28

Figure 16. Cross section of a resonator through the Au pad lift-off step. 29

Figure 17. Resonator through the stack etch process step prior to backside patterning. 30

Figure 18. The wafer after the backside mask has been etched. The wafer is now ready for two deep silicon trench etch steps. 31

Figure 19. The wafer after both silicon trench etches. The wafer is now ready for release. 32

Figure 20. A schematic of the wafer after an alkaline etch of the backside silicon. The top layer is the spun-on protection layer. 33

Figure 21: Final device with a dry back side etch after buffered oxide etch to release the structure. 34

Figure 27. 3D model of a thin-film piezoelectric-on-silicon (TPoS) resonator with acoustic reflectors. 36

Figure 28: Electrical equivalent of resonator-tether-substrate acoustic interaction 38

Figure 29: Changes in the normalized impedance seen by the resonator depending on length and the ratio of load impedance to the characteristic impedance of the tether.................................... 40

Figure 30: 2-D models of third harmonic lateral extensional resonators without (a) and with acoustic reflector trenches showing the resulting perturbation fields. Please note the color intensity in the substrate has been increased to better highlight the perturbation in this region. All unspecified boundaries are strain-free. 42

Figure 31. Perturbation through the center of the 2-D simulation without and with acoustic reflectors. The inset shows a 2-D representation of half of the resonator. The dashed line shows the center of the resonator on both the plot and the inset. 43

Figure 32. A portion of the cross section through the resonator's length to highlight the electrical simulation's boundary conditions. Green lines are the ground planes. Orange and red lines show the electrical input and output planes respectively. The light blue is the piezoelectric layer while

grey is the single crystal silicon. The tan blocks are electrical-only components that have a material resistivity such that the total source impedance and total load impedance are both 50Ω.44

Figure 33. Two 3-D models of one quarter of resonator for coupled-domain simulation showing the pertinent parameters. 46

Figure 34. Simulated $Q_{unloaded}$ for third harmonic 110MHz, lateral-extensional, TPoS resonators with no reflector with different tether lengths. The red line is a least squares sinusoidal fit for the data set. 47

Figure 35: Simulated reverse transmission coefficient, S_{12}, for third harmonic 110MHz, lateral-extensional, TPoS resonators without and with acoustic reflectors. The insets show the strain (color) and the structural deformation near resonant frequency. Both figures have the same deformation and strain (color) scales. 48

Figure 36. 27MHz fundamental lateral extensional mode without acoustic reflectors (a) and with close (b) and far (c) acoustic reflectors. 49

Figure 37. Average measured $Q_{unloaded}$ for 27MHz resonators with error bars denoting highest and lowest recorded for over 20 devices tested. 50

Figure 38. Measured frequency response for the top performing 27MHz reflectors without and with reflectors 51

Figure 22. Average and maximum $Q_{unloaded}$ of fabricated ~490MHz single tether devices with varying device lengths. 52

Figure 23. Average and minimum motional impedance of fabricated ~490MHz, single tether devices with varying device lengths. 53

Figure 24. Average and maximum $Q_{unloaded}$ for ~490MHz resonators with different harmonic orders. 53

Figure 25. Average and minimum motional impedance for ~490MHz resonators with different harmonic orders. 54

Figure 26. Measured frequency responses S_{21} magnitude for higher harmonic order resonators. Larger resonators (higher harmonic mode) have a propensity for strengthen spurious modes..... 55

Figure 39. $Q_{unloaded}$ for simulated and fabricated 110MHz resonators with no acoustic reflectors. Please note that the simulated data shown here is a subset of the data in figure 8....................... 56

Figure 40. The measured frequency responses of the 110MHz resonators exhibiting the highest measured Q (with and without reflector).. 57

Figure 41. Cross-wafer $Q_{unloaded}$ measurements for 110MHz resonators with tether length of 9μm (λ/8) without (black) and with reflectors (red) at 36μm (λ/2). X denotes device locations that were non-functioning for this design... 58

Figure 42. Measured and simulated Qunloaded from third harmonic 110MHz, lateral-extensional, TPoS resonators with acoustic reflectors. 59

Figure 43. Screen capture of a high $Q_{unloaded}$ device as measured in atmosphere. 60

Figure 44. Screen capture of a high $Q_{unloaded}$ as measured under vacuum. 60

Figure 45. Simulated frequency response for 400 MHz designs over a 4 MHz span with different number of tether pairs.. 62

Figure 46. TPoS resonators with one pair (left) and two pair (right) of tethers. 62

Figure 47. Large span frequency responses for 400MHz resonators with one and two pairs of tethers. 63

Figure 48. Measured frequency responses (magnitude and phase) of ~410MHz resonators with one and two pairs of tethers... 64

Figure 49. Average $Q_{unloaded}$ for increasing number of tether pairs on 500MHz resonators.......... 65

Figure 50. Frequency responses for ~1GHz resonators with one and nine pairs of tethers. 66

Figure 51. Temperature response for the ~1GHz TPoS resonator with nine support tethers........ 67

Figure 52. A 27MHz TPoS resonator under varying input power levels. 70

Figure 53. A model of a asymmetric resonance peak from a frequency response. Location of the peak (f_p) and the center (f_r) are noted. 71

Figure 54. As expected with theory, altering the length does not have a strong dependence on power handling capability. 72

Figure 55. Increasing harmonic order shows a distinct improvement in power handling capability. 72

Figure 56. Increasing tether number provides an avenue to increase both the quality factor and power handling capabilities. 73

Figure 57. Power handling capability for 1GHz TPoS resonators with different number of tether pairs. 73

Figure 58. Frequency response for 1GHz resonators. 74

Figure 59. A typical power gain curve showing the 1dB (red) gain compression point at ~28dBm input power as the gain has been desensitized compared to the ideal (dotted blue). 74

Figure 60. Frequency responses of a fifth order 118MHz TPoS resonator with one pair of supports. The blue curve shows the resonator with a -5dB input power. As the power increases to 10dB, the resonator's peak shifts lower and to the right as seen in green. 76

Figure 61. Gain curve for a fifth order 118MHz TPoS resonator with one pair of supports. The device shows definitive gain compression with a P_{-1dB} of ~22dBm 77

Figure 62. Typical gain curve for seventh harmonic 118MHz TPoS resonators with three pairs of tether pairs. The devices exhibit a period of gain expansion before rapid gain compression. 78

Figure 63.The P_{-1dB} gain compression points for 118MHz TPoS resonators. 79

Figure 64. Third harmonic thin-film piezoelectric on silicon resonator with a target frequency of 120MHz. 83

Figure 65. 120MHz, third order thin-film piezoelectric on silicon resonator with acoustic reflectors 84

Figure 66. Fundamental order, 27MHz thin-film piezoelectric on silicon resonator. 84

Figure 67.Fundamental order 27MHz thin-film piezoelectric on silicon resonator with acoustic reflectors positioned too close to the resonator. 84

Figure 68. Fundamental mode 27MHz thin film piezoelectric on silicon resonator with acoustic reflectors at the near optimal position. 85
Figure 69.Seven harmonic, 470MHz thin film on piezoelectric on silicon resonator with one tether pair... 85
Figure 70. Seventh order thin film piezoelectric on silicon resonator with two tether pairs......... 86
Figure 71. Twenty-first harmonic thin film on piezoelectric on silicon resonator targeting 1GHz with one tether pair.. 86
Figure 72. Twenty-first harmonic thin film piezoelectric on silicon resonator with nine tether pairs targeting 1GHz. 87

NOMENCLATURE

S, S_{ik}	Scattering matrix, scattering component with *k* as the input and *i* as the output
$\boldsymbol{\sigma}, \sigma_k$	Stress tensor, stress component
$\boldsymbol{\tau}, \tau_k$	Strain tensor, strain component
ϵ, ϵ_{ij}	Elasticity/stiffness matrix, component
d, d_{ij}	Piezoelectric tensor, piezoelectric component
$\mathbf{E}, E_k$	Electric field, electric field component
$\mathbf{D}, D_n$	Electric displacement field, electric displacement field component
$\varepsilon, \varepsilon_n$	Electric permittivity, electric permittivity component
ρ	Material density
w	Device dimension in direction of strain, longitudinal
l	Device dimension in plane of motion but normal to strain, transverse
t	Device dimension normal to plane of motion, thickness
R_m	Motional impedance
L_m	Motional inductance
C_m, C_0, C_s	Motional capacitance, feed-through capacitance, parasitic capacitance
n	Modal number
f, ω	Frequency and angular frequency
f_n, ω_n	Resonant frequency of mode number, n
ν	Particle velocity
Z_0	Characteristic acoustic impedance
β	Acoustic wavenumber

m_e	Effective mass
γ_e	Effective damping
k_e	Effective spring constant
η	Electromechanical coupling
F	Apparent force
i	Electric current
v	Electric voltage
Q	Resonance quality factor
T	Device temperature
k_B	Boltzmann's constant
$L(\Delta\omega)$	Phase noise-to-carrier ratio
E_{stored}	Energy stored in resonator in a cycle
X_c	Critical vibrational amplitude
D_n	Relative frequency shift
P	Power
G	Apparent power gain
g_n	Polynomial gain component
a	Signal amplitude
t	Time

CHAPTER I

INTRODUCTION

Today, high-frequency acoustic resonators serve as frequency references and filters, integral components of communication electronics. More specifically, piezoelectric resonators have been used in electric circuits since Walter Cady's discovery of accurate, sharp, stable resonance peaks in frequency responses of quartz and Rochelle salt crystals in 1922 [1] . The overall performance of the target application depends greatly on the resonator's intrinsic performance. In sensors, sensitivity can be tied to quality factor and frequency stability [2]. In filter applications, motional impedance and quality factor improve frequency selectivity [3]. Finally in oscillator circuits, quality factor and power handling affect phase noise while lowering motional impedance will reduce the gain requirement for the feedback amplifier [4]. The focus of this work is to show that motional impedance, quality factor, and power handling can be simultaneously improved through careful design of resonator/substrate interaction. Recent previous work on piezoelectric resonators for timing applications (Chapter II) shows that achieving high quality factor with low motional impedance is a difficult feat. Chapter III describes the platform for this body of work, the lateral-extensional, thin-film piezoelectric-on-silicon resonator. In addition, the critical

microwave metrics, namely resonance frequency, quality factor, and motional impedance and how to measure the specific metrics is covered in this chapter. Chapter IV outlines the theory of operation for a general lateral-extensional piezoelectric resonator and partial description of governing loss mechanisms. A step-by-step process flow to fabricate thin-film on piezoelectric-on-silicon resonators is covered extensively in Chapter V. Device design parameters and their limited effect on quality factor are covered in Chapter VI. Chapter VI also outlines a novel substrate modification, in-plane acoustic reflectors, which can greatly improve the quality factor of lateral extensional resonators if positioned properly. However, the motional impedance remains high. Chapter VII shows for the first time that additional support tethers tied to the substrate can drastically improve quality factors simultaneously while reducing the motional impedance in lateral-extensional thin-film piezoelectric on silicon resonators, resulting in the largest reported resonance frequency-quality factor product. The power handling performance, characterized as frequency shift and gain compressions, in the devices with numerous tether pairs are measured for the first time to thin-film piezoelectric-on-silicon lateral extensional resonators in Chapter VIII. The devices with more substrate tethers not only exhibit higher quality factors, lower motional impedance, but can also dissipate larger input power before exhibiting nonlinearity.

Concluding remarks and potential avenues for future work can found in Chapter XI. Appendices containing scanning electron microscope images and computer scripts used in the generation of data are located in Chapter X, while the works cited are listed in Chapter XI.

CHAPTER II

REVIEW OF LITERATURE

In 1881, while exploring the extent of the pyroelectric effect, Jacque and Pierre Curie discovered the direct piezoelectric effect, converting mechanical strain into charge. Subsequently, Gabriel Lippmann postulated the existence of the converse piezoelectric effect, electrical charge into mechanical strain, which the Curie brothers quickly confirmed experimentally a year later. While the first application for a piezoelectric transducer was to generate and sense acoustic waves in sonar, Walter Cady proposed using a piezoelectric resonator as both a frequency-standard and a frequency-stabilizer in 1922 [1] The resonator would soon become a central component in communication circuitry. Cady discovered that geometries and material properties dictate the effective electrical properties of the resonator. To reduce mechanical damping (anchor loss) in his structure, Cady suspended his resonant beam by a metal hook (Figure 1) or used ball bearings for the beam to glide laterally. The result was a relatively stable set of the electrical properties that could be used to standardize communication frequencies in early telephone systems.

K.S. Van Dyke and Warren P. Mason extended Cady's resonator work in 1928 and 1930 [5], [6] respectively and applied it to laterally extensional quartz resonators. Quartz, an abundant single crystal, piezoelectric material would become the default material in communication circuitry.

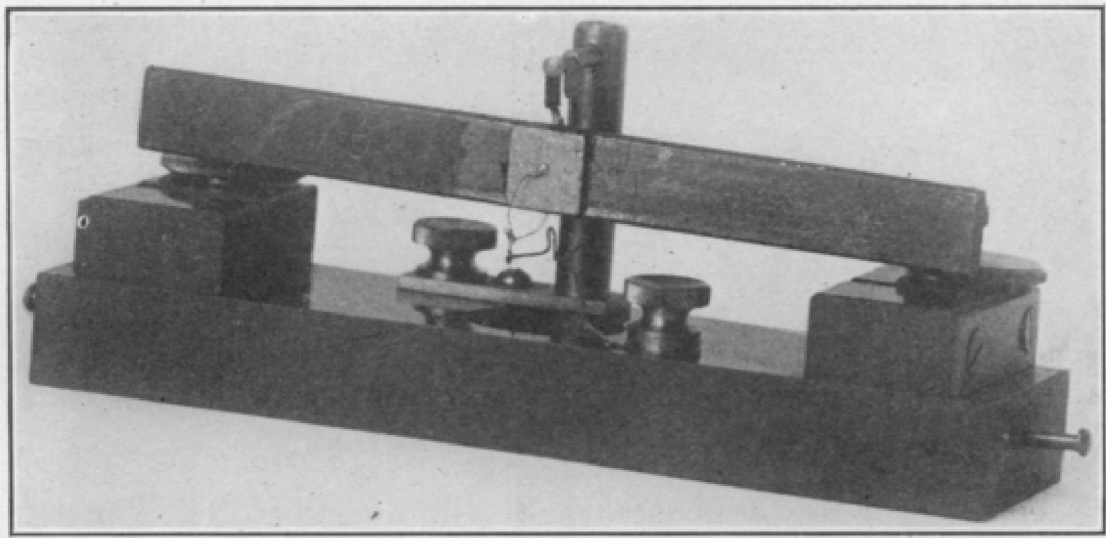

Figure 1: Cady's frequency standard used two quartz plates to excite a 10cm steel bar for 11km wavelength

In more recent times, quartz-based resonators, surface-acoustic wave (SAW) devices, and bulk acoustic wave (BAW) devices are commonly employed to provide the resonator component for oscillator and filter applications. In comparison to purely electrical resonators, acoustic resonators provide higher quality factors with lower insertion loses [7], [8]. In the commercial communications sector, demands on data bandwidth have driven devices to higher and higher frequencies with stricter requirements on tolerances. In 1940, only a few thousand commercial broadcast transmitters existed and therefore larger tolerances were adequate. For GSM, a more modern standard, the frequency error can be up to 0.32 parts per million (ppm) at 900MHz or 0.18ppm at 1800MHz [9]. For the next generation communication, LTE, the requirement has reduced to 0.10ppm [10].

To create quartz resonators, a single slab of quartz is singularized and ground to size. Variation in the singularization results in high resonance frequency variation from piece to piece. To compensate for the variation, the crystal's resonance frequencies are trimmed downward typically by adding mass to the crystals until the frequency drops to the target frequency.

As the drive to push quartz to higher and higher frequencies, the singularization becomes more difficult. The pieces must be machined to precise dimensions and variation in the process becomes more significant as wavelength decreases. To combat the increased variation, even more trimming is required and performance, cost, and throughput all suffer. Therefore as the drive to hit higher frequencies, other approaches such as surface acoustic wave and bulk acoustic wave devices were pursued.

Surface acoustic wave (SAW) devices were an integral component of early mobile phones. Their use as a filter component for both incoming (RX) and outgoing (TX) signals enabled high bandwidth implementations at a very low cost. SAW devices operate by driving and sensing a Rayleigh wave on top surface of a piezoelectric material. They are typically fabricated by taking a cut from a single crystal piezoelectric material such as lithium niobate, lithium tantinate, or quartz. Electrodes are patterned on top of the piezoelectric crystal to define the mode shape and the frequency. However, SAW devices possess limited power handling capabilities and thereby their noise floor.

More recently, bulk acoustic wave (BAW) devices have gained momentum into the mobile phone market. BAW devices use a patterned electrode on top of piezoelectric layer to excite a thickness-extensional mode in the direction of the substrate. The mode's energy is confined through a series of alternating high and low acoustic impedance layers, known as a Bragg reflector. The reflector can either fabricated directly on the substrate as is the case in a solidly mounted resonator (BAW-

SMR) device, or it can be released from the substrate to gain better isolation as in the case of a film bulk acoustic resonator (FBAR).

The operational frequency and generally the performance of the BAW device is dictated by the deposited thin-film materials and their thicknesses, thereby limiting the flexibility for frequency selection. Typically, the piezoelectric materials of choice for BAW are lead zirconium titinate (PZT) or aluminum nitride (AlN). The later has gained quite a bit of momentum due to its environmental stability, relatively low deposition temperature (<500C), and its low loss at radio frequencies. In addition, consistent, uniform depositions of AlN layers have become easier to achieve due to equipment enhancements. Currently many cellular phones use components with an AlN FBAR for their RX/TX filter.

Micromachined lateral extensional devices are a more recent approach to eletromechanical resonator design. Micromachined lateral extensional devices vibrate in the plane of the wafer and offer a few distinct advantages over thickness-mode or SAW devices. Since the frequency is primarily a function of the in-plane device dimensions, multiple devices with different target frequencies within a close proximity can be defined through photolithographic processes [11]. These resonators are typically either capacitive-based [12], [13], [14] or piezoelectric-based [15], [16], [17]. Capacitive designs, whether using a capacitive air-gap [12] or an internal dielectric film [13], [14], rely on the electrostatic force to drive the resonator body, often composed of a single-crystal material, such as single crystal silicon. Capacitive designs are limited at high resonant frequencies due to their inherently small coupling coefficients resulting in their relatively high device impedances. On the other hand, piezoelectric designs exhibit an improved transduction coefficient and have been shown orders of magnitude lower motional impedance as compared to capacitive-based designs [15], [18]. However, the quality factor for piezoelectric resonators is diminished as compared to electrostatic devices [15]. Recently, thin-film piezoelectric-on-silicon resonators, a subset of piezoelectrically-transduced resonators, have

successfully shown an improved quality factor while maintaining very low motional impedances [17]. These micromachined, lateral extensional, thin-film piezoelectric-on-silicon (TPoS) resonators will serve as the platform for this research.

Review of recent micromachined piezoelectric resonators publications

The research of micromachined piezoelectric resonators for timing circuits has been a fairly active topic in recent years (Table 1). Early on, zinc oxide (ZnO) was explored for the piezoelectric layer, but the material has seen interest wane due to high deposition temperature requirements and large intrinsic loss at radio frequencies. The bulk of the research has been now been focused on aluminum nitride (AlN) with or without a single crystal silicon (Si) resonant body. The AlN/Si material combination has the benefit of low piezoelectric layer deposition, possible CMOS compatibility, and an intrinsic low mechanical loss crystalline silicon layer. Other resonant materials have been selected such as silicon dioxide (SiO_2) and nanocrysalline diamond (NCD) for thermal stability and high power handling respectively.

Table 1. Piezoelectric transduced micromachined resonators targeting the real-time clock application space sorted by f Q product figure of merit.

Reference	Fr (Hz)	Q	f Q	Rm (Ω)	Material	Mode
This work	983e6	6700	6.6e12	162	AlN on Si	Lateral extensional
This work	115e6	17300	2.0e12	1400	AlN on Si	Lateral extensional
[19]	496e6	3800	1.9e12	650	AlN on Si	Lateral extensional
[20]	497e6	3800	1.9e12	600	AlN on Si	Lateral extensional
[20]	208e6	7300	1.5e12	80	AlN on Si	Lateral extensional
[21]	2.0e9	700	1.4e12	25	AlN on SiO2	Thickness extensional
[22]	22e6	51000	1.1e12	1500	AlN on Si	Lateral extensional
[19]	467e6	1600	7.4e11	600	ZnO on NCD	Lateral extensional
This work	27e6	23300	6.3e11	257	AlN on Si	Lateral extensional
[23]	107e6	4800	5.1e11	15500	ZnO on Si	Lateral extensional
[22]	26e6	18000	4.7e11	240	AlN on Si	Lateral extensional
[24], [25]	221e6	2100	4.6e11	35	AlN	Lateral extensional
[26]	102e6	1300	1.3e11	1138	AlN on Si	Lateral extensional
[27]	14e6	2300	3.2e10	376	AlN	Lateral extensional
[28]	966e3	20000	1.9e10	200	AlN on Si	Lateral extensional
[29]	1.7e6	6200	1.1e10	2654	ZnO	Flexural

Table 1 shows the performance of recent publications of piezoelectric resonators for timing applications. Included in table are resonators with acoustic reflectors (Chapter VI) and multiple tether pairs (Chapter VII). The resonators utilizing multiple tether pairs (Chapter VII) exhibit the highest frequency-quality factor product of any published piezoelectric transduced resonator. In designing resonators-to-substrate interfaces, the anchor end is commonly assumed to be fixed resulting in a quarter wavelength tether length [23]. Chapter VI shows that anchor loss is the dominate loss mechanism for lower frequency devices. In addition, quarter wavelength tether length can lead to acoustic energy being coupled to the substrate resulting in sub-optimal quality factors.

A second approach to the anchor loss is utilizing thin, compliant spring anchors to convert the lateral-extensional motion to in-plane flexural mode [22], [30]. However, this can lead to strong spurious modes due to the anchor-resonator interaction. The spring configuration can also lead to reduced power handling as self-heating can become significant as the thermal resistance from resonator to substrate is increased [31].

Furthermore, papers which directly address anchor loss often limit their scope to flexural modes [32] and out-of-plane motion [33], [34] which not is not natively applicable to lateral-extensional resonators. The focus of this work is to show novel structures which can address a critical parameters limiting lateral-extensional resonator's performance.

CHAPTER III

METHODOLOGY

In micromachined thin-film piezoelectric-on-silicon devices, piezoelectric transduction is used to excite/sense the resonant mode of the composite structure made from the piezoelectric layer and single crystalline silicon. The low-loss single crystalline resonant body material gives rise to an improved quality factor over a purely piezoelectric resonator [17]. The top electrode pattern is designed such that similarly strained resonance areas are electrically connected. Therefore, both fundamental (Figure 3(a)) and the second overtone (Figure 3(b)) modes of a rectangular block can be excited using the electrode pattern seen in Figure 2, and both modes are utilized in this work. The tethers are commonly placed on the minimum displacement nodes and typically have narrow width in order to minimize their effect on the mode shape. As the device expands and contracts along the device width, the non-zero Poisson's ratios of the structural material originate the displacement along the length and the thickness of the device as seen in Figure 3. The suspended structure provides a confinement for the out-of-plane motion, but the tethers positioned at the device edge on minimum displacement nodes provide a pathway for in-plane elastic energy to

escape. As will be seen later in the simulation section, the tethers act like sources of acoustic waves, which radiate energy into the substrate.

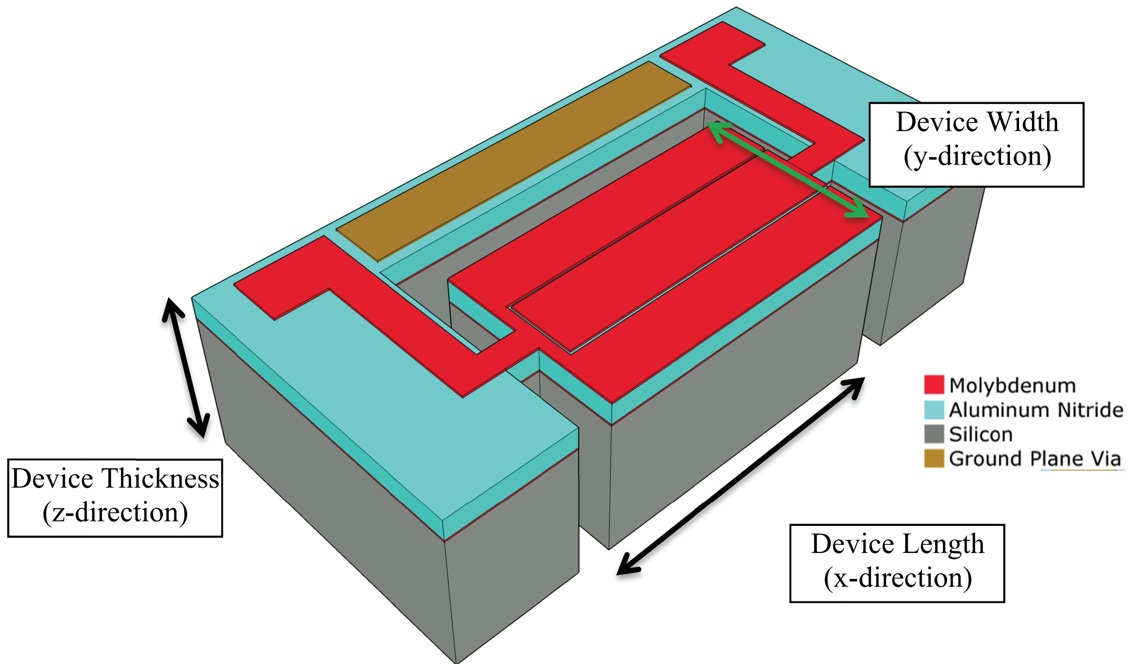

Figure 2. A schematic of a micromachined, lateral-extensional (motion in the y-direction), thin-film piezoelectric-on-silicon resonator.

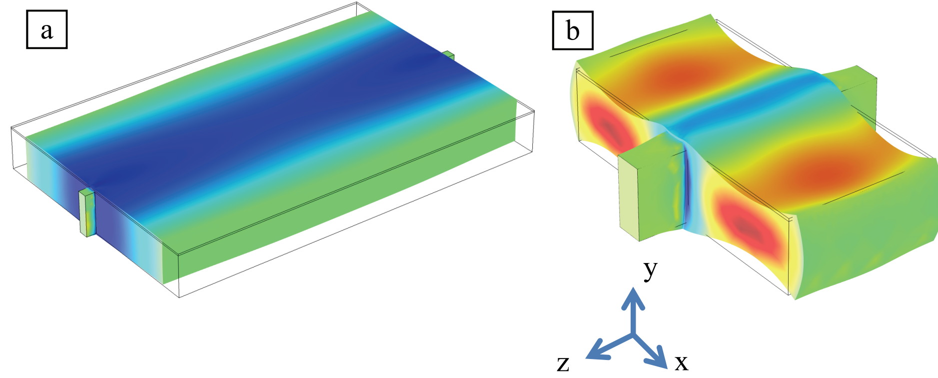

Figure 3. Simulated, deformed fundamental (a) and third order harmonic (b) lateral extensional modes. Blue color denotes regions of contraction (negative strain) while red shows regions of expansion (positive strain) along the axis of vibration (x-axis).

To measure the overall resonator performance, the complex microwave scattering (S) parameters are utilized. Frequency dependent S-parameters can be used to describe port-to-port interaction. For a 2-port device, a 2x2 S-parameter matrix (1) fully describes the operation of the device.

$$\begin{bmatrix} S_{11} & S_{12} \\ S_{21} & S_{22} \end{bmatrix} \tag{1}$$

Notation is standardized on S_{mn} where n is the input port and m is the output port for the measurement. Therefore, S_{11} will be reflection coefficient for port one while S_{21} is the gain from port one to port two. In a linear and consequently reciprocal system, S_{21} is equal to S_{12}. The markers on a typical magnitude of S_{12} (or S_{21}) frequency response seen in Figure 4 describes the position of three critical parameters, resonant frequency, insertion loss, and quality factor. The frequency response shows a very clean, linear response with no nearby spurious modes and no spring softening or spring stiffening peak distortion (Chapter VI).

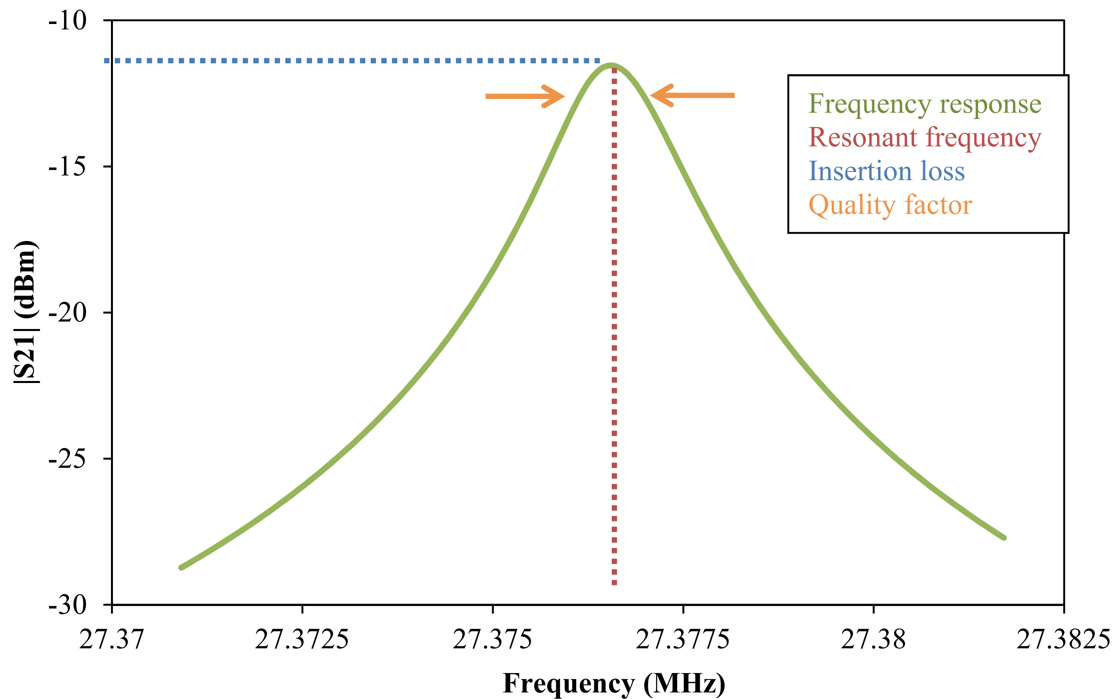

Figure 4. A frequency response of the magnitude of S_{21} denoting key resonator parameters

To measure the S-parameters, a microwave network analyzer can be used. For all measurements in the manuscript, an Agilent Technologies E8358A PNA network analyzer was utilized. Both ports on the network analyzer are specified to have 50Ω impedances. The devices are typically probed at the wafer level using a manual probe station while at room temperature and at atmospheric pressures. The probes used for testing were both Cascade |Z| Probe GS with a 150µm tip-to-tip pitch. The probes approach the pads from opposite directions and share the middle ground pad. The probes are connected through a pair of 50Ω, coaxial SMA cables to channel 1 and channel 2 on an Agilent PNA network analyzer.

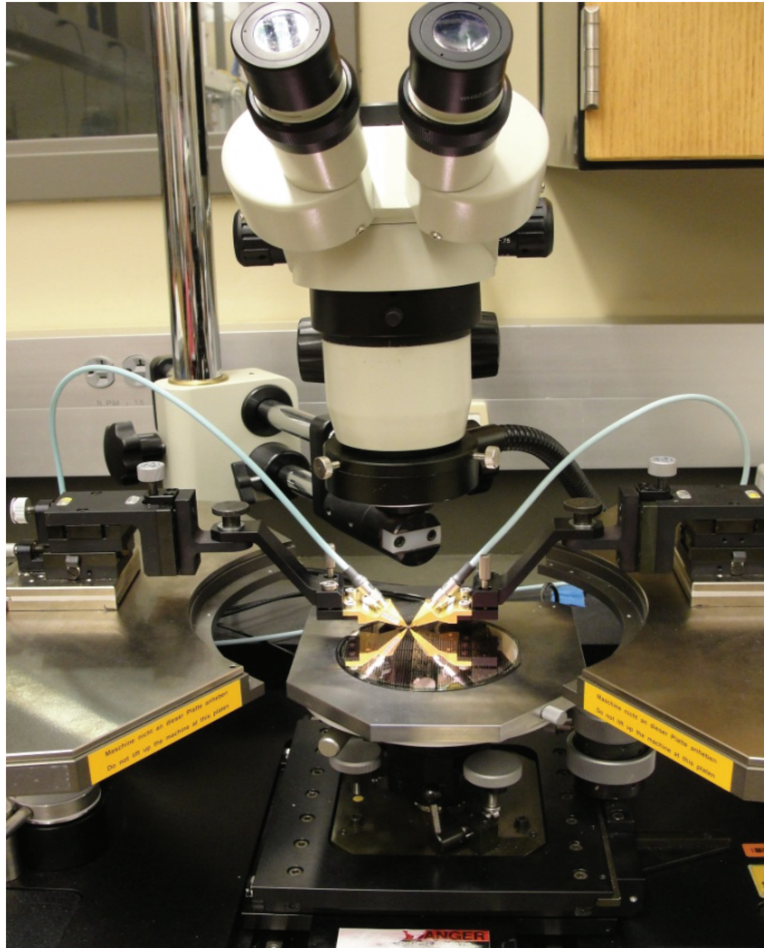

Figure 5. Manual wafer-level RF probe station.

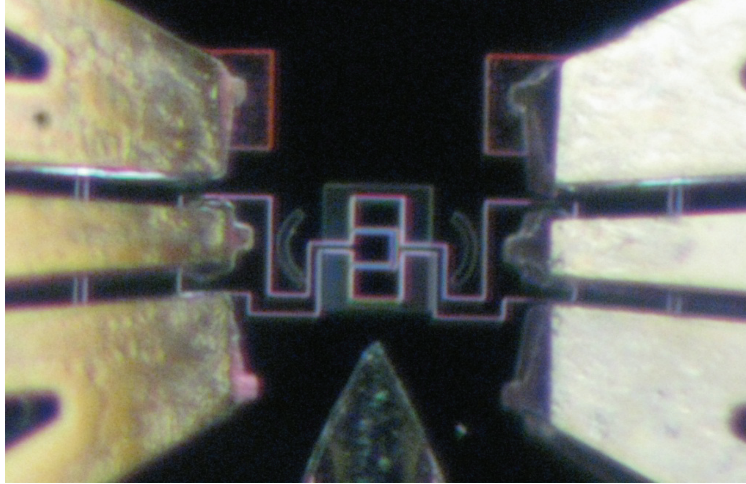

Figure 6. DUT actively being probed by two GSG probes.

For temperature coefficient of frequency (TCF) and low-vacuum measurements, a vacuum probe station (Figure 7) was used. Samples are mounted on a temperature-controlled chuck with clips and the system is pumped down using a small, lab pump. Vacuum pressure is measured with a Pirani gauge with the nominal measurement pressure below 1mTorr. For all TCF measurements, a temperature range of 20C to 120C is used. Liquid nitrogen is flowed through the sample chuck to reach the lower temperatures while a proportional-integral-derivative (PID) controller connected to an integrated heater is used to stabilize the temperature.

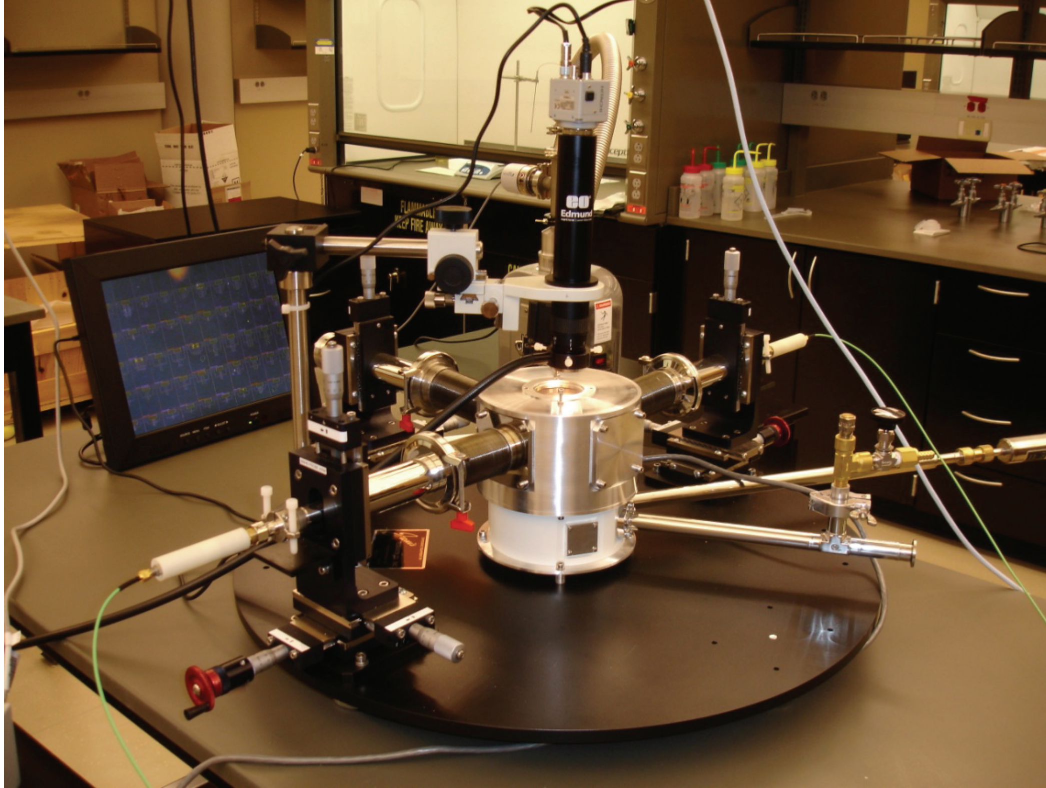

Figure 7. Janis vacuum probe station for RF measurements

To calibrate the probes and the cables, a two-port Short-Open-Load-Thru (SOLT) calibration sample is placed probe station's chuck. The calibration sequence is initiated on the network analyzer for a given frequency range. The corresponding pads on the calibration sample are probed as the network analyzer instructs to contact the shorted, open, loaded, and thru pads. The calibration is verified by repeating the cycle and comparing the measured frequency responses (S_{11}, S_{12}, S_{21}, and S_{22}) to the expected, post calibration responses. If the calibration is unsuccessful, the resonator's frequency response could exhibit improper magnitude or phase.

CHAPTER IV

THEORY

Linear elastic waves in solids are governed by a stress-strain relationship,

$$\boldsymbol{\sigma} = \epsilon \cdot \boldsymbol{\tau} \tag{2}$$

where the stress and strain six component tensors are related by the 6x6 elasticity, or stiffness, matrix. For piezoelectric materials, the equation is expanded to include the piezoelectric component to take the form:

$$\boldsymbol{\sigma} = \epsilon \cdot \boldsymbol{\tau} + d \cdot \mathbf{E} \tag{3}$$

$$\mathbf{D} = d \cdot \mathbf{T} + \varepsilon \cdot \mathbf{E} \tag{4}$$

These two equations now completely define the piezoelectric transduction. In the case that the material is non-piezoelectric, $d = 0$, like single-crystal silicon, the equation resolve to Hooke's law and the linear and unpolarized, dielectric equation. It is through these transduction equations that the force, F, is converted to a corresponding voltage V. In two-port piezoelectric devices, the

transduction can be further abstracted to two coupling coefficients, η_i and η_o, for the input and output respectively. In a composite structure like the TPoS resonators, the coupling coefficients can be difficult to predict due to the complex nature of the film interactions. The design of the electrodes, the target mode, and the material properties and thicknesses all contribute to determine the actual coupling coefficients.

The mechanical motion of a resonator is typically modeled as a mass-spring system with the form:

$$m_e\ddot{x}(t) + \gamma_e\dot{x}(t) + k_e x(t) = F(t) \quad (5)$$

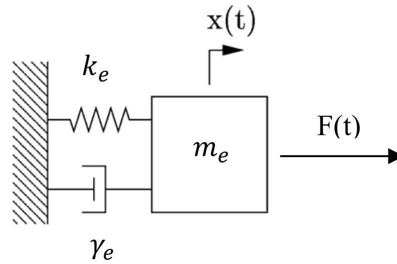

Figure 8. Mechanical representation of a mass-spring-damper system under a force, F.

If the piezoelectric transduction is added to the mechanical resonator, the result is a circuit in Figure 9. Note that under this configuration the phase of the input is at 180 degrees from the output. For resonators where the input and the output electrodes, have matched phases, the direction of one transformer is reversed. C_{s1}, C_{s2}, and C_0 are parasitic capacitors quantifing the interactions between input electrode and the ground plane (C_{s1}), the output electrode and the ground plane (C_{s2}), and the input and output electrodes (C_0). In practice, these are difficult to predict and therefore require the resonantor's fabrication and subsequent measurement.

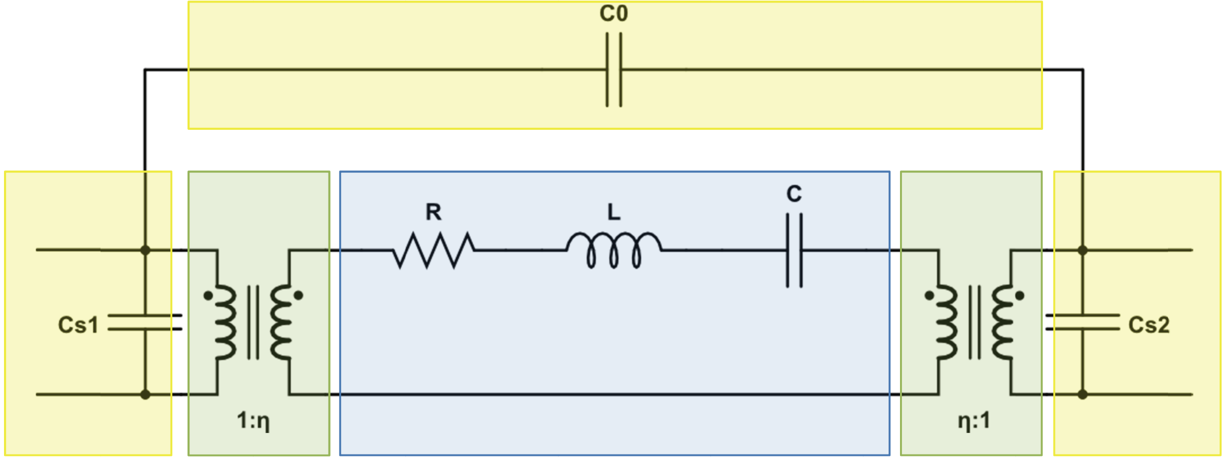

Figure 9. Generalized piezoelectric resonator with electric portions (yellow), transduction (green) and a mechanical resonance portion (blue).

Through the electromechanical coupling, η, the electrical form is written as:

$$L_m \frac{\partial i}{\partial t} + R_m i + \frac{1}{C_m} \int i \, \partial t = v \tag{6}$$

$$f_r = \frac{1}{2\pi} \sqrt{\frac{k}{m}} = \frac{1}{2\pi \sqrt{L_m C_m}} \tag{7}$$

If the input and the output coupling coefficients are assumed to be the same, the effective motional inductance and capacitance of the resonator:

$$m_e = \frac{\rho w t l}{2} = \frac{m_{resonator}}{2} \tag{8}$$

$$k_e = \frac{\pi^2}{2} \frac{w t n^2}{l E_f} \tag{9}$$

$$\gamma_e = \frac{2\pi f_r m_e}{Q} \tag{10}$$

$$L_m = \frac{m_e}{\eta^2} \tag{11}$$

$$C_m = \frac{\eta^2}{k_e} \tag{12}$$

$$R_m = \frac{\gamma_e}{\eta^2} \tag{13}$$

From these parameters, the middle portion of circuit in Figure 9 can be simplified to a one-port resonator, modeled as a modified Butterworth-Van Dyke (mBVD) circuit as seen in Figure 10.

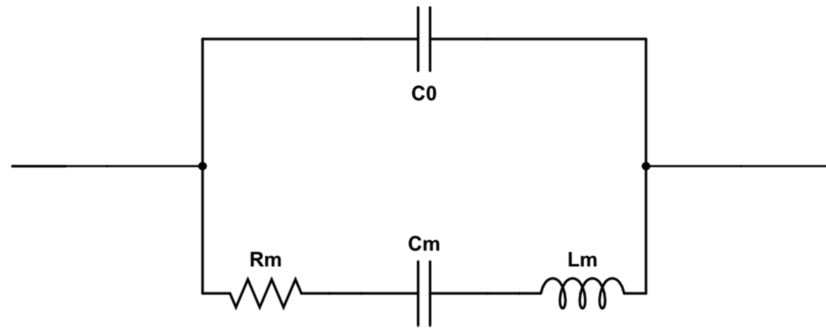

Figure 10: One port resonator

The model can be extended further to include the parasitic shunt capacitors (C_{s1} and C_{s2}) and in turn, making it a two port device. Frequency responses similar to Figure 4 can be captured using a circuit simulator.

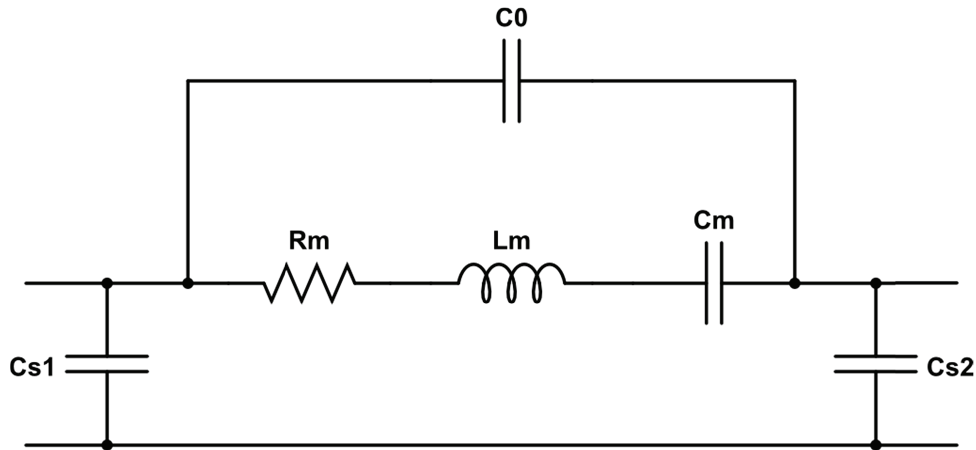

Figure 11: Two port resonator with its two parasitic shunt capacitors.

Loss

As mentioned previously, quality factor is a critical resonator parameter. Quality factor (Q) is defined as:

$$Q = 2\pi \frac{Energy\ stored\ per\ cycle}{Energy\ lost\ per\ cycle} = \frac{\sqrt{k_e}}{\gamma} = \frac{1}{R_m}\sqrt{\frac{L_m}{C_m}} \tag{14}$$

One avenue to improve the quality factor is to increase motional capacitance while the loss remains constant. To increase the motional capacitance there are a few avenues such as increasing actuation and resonant area, but each can prove difficult to keep the loss constant and keep spurious modes from becoming significant. Therefore the performance increase from these changes can to be limited as seen in the beginning of Chapter IV. The other direction to improve Q is to reduce loss, which has a stronger relation to quality factor. The overall Q can be written as the parallel combination of Qs of different components

$$1/Q_{Total} = \sum_i 1/Q_i \tag{15}$$

In this fashion, it can be seen that a singular component can easily limit the overall quality factor of the device. In RF piezoelectric-on-silicon resonators, there are several avenues for loss as explain subsequently.

Thermal elastic dissipation (TED)

Thermal elastic dissipation (TED) [35], [36], [37], [38] is the outcome of internal friction from the sustained vibration. Areas of compression and rarefaction, dictated by mode shape and acoustic wavelength, describe spatially the "hot" and "cold" regions respectfully. Thermal currents between these regions work to equalize the regions resulting in loss. Therefore, in simple lateral extensional resonators, the magnitude of TED can be estimated solely with the operational frequency and the resonant material. Quality factors for TED for lateral extensional silicon

resonators have been calculated to be >1e5 in the frequency region of interest [39]. Work has been done to improve TED in bar resonators by adding etch holes to the resonant structure to increase the separation between the "hot" and "cold" regions but the resulting differs from a simple lateral extensional mode [40].

Squeeze-film damping

Squeeze-film damping [41] [42] is a large contributor to loss in many different MEMS architectures [43], [44], [45]. In capacitive resonators, small transduction gaps can give rise to significant squeeze-film damping. The phenomenon exists as the motion of the device causes a significant volume of air to displace within a confined space. Since the gaps do not play a role in the transduction in the TPoS architecture, they can be widened such that squeeze-film damping is not a notable contributor to the overall loss.

Viscous damping

As the resonator vibrates, the surrounding medium is displaced. The medium has some internal frictional forces that lead to loss. In lateral extensional resonators, since the cross-sectional area of the movement and the order of displacement are both relatively small and the medium is easily displaced, the viscous damping is low. The magnitude of viscous damping and squeeze-film damping can be measured by probing the devices while under vacuum as seen in later sections.

Interfacial damping

In a composite resonator like the thin-film piezoelectric-on-silicon resonator, the interface between the piezoelectric layer and the resonant material should be examined for interfacial damping. Interfacial damping occurs from when the materials on either side of the interface have differing density and stiffness thereby having different acoustic velocities [46]. To reduce this damping, the material stack in the TPoS resonator is chosen such that the acoustic velocities are similar thereby reducing this loss factor.

Ohmic losses

As the components in piezoelectric MEMS resonators are of significantly small size, ohmic losses can be a contributor to the overall loss. The sheet resistance, wire length, and wire cross section govern the wire factor. Even those the metal interconnects are thin, the overall resistance can be kept low through low-resistance materials and short wire lengths. The largest contributor to ohmic loss is at the contact pads. To lessen the ohmic loss at the bond pads, the bond pads are coated with a thin layer of gold.

Piezoelectric and dielectric losses

As (2) shows the piezoelectric and dielectric constants effect the mechanical and electrical displacements. Since these constants can have loss components (usually denoted as imaginary components of the complex constants), the applied electric field can be reduced. For aluminum nitride, the lossy components in both the piezoelectric and dielectric constants are low at radio frequencies [47].

Anchor loss

Anchor loss [42], [48], [49], [50], also referred to as attachment or clamping loss, is the quantification of the elastic energy leaving the resonator through the structural elements connecting it to a frame. Even though the anchors/tethers are optimally positioned at the resonator's modal nodes for the target frequency, some periodic displacement still occurs at these points. As a resonator vibrates it exerts force on the tether causing acoustic energy to travel down the tether and to subsequently be transmitted into the substrate. Due to the discontinuity in the acoustic impedance on the path from the tether to the substrate, a portion of the wave is reflected at the tether end and is returned to the resonator while the rest is radiated into the substrate as an elastic wave. Without any additional reflective surface, namely an acoustic reflector, the radiated elastic wave is unable to return to the resonator, and consequently, that energy is lost. Use of an acoustic reflector is practiced extensively in solidly-mounted thickness-mode resonators [51],

[52]. In the thickness-mode resonators, a Bragg reflector consisting of alternative high and low acoustic velocity materials, with one-quarter acoustic wavelength thickness, is positioned under the resonant stack to confine the energy. Recently, resonators with planar acoustic reflectors, namely Bragg reflectors and mesa-isolated structures, were examined to mitigate spurious modes and to increase the quality factor [53], [54]. In Chapter VI, the application of planar acoustic reflectors in micromachined lateral-extensional resonators is investigated for the first time.

CHAPTER V

FABRICATION

Micromachined devices are fabricated utilizing either bulk micromachining and/or surface micromachining techniques. In bulk micromachining, the substrate is etched to form a structural component comprised of the substrate material. The substrate, typically single crystal silicon, offers known material parameters with little processing overhead. However, bulk micromachining limits the material selection and the complexity.

In contrast, surface micromachining relies on additional layers deposited on the substrate and subsequently patterned. Deposited layers can introduce operational variability due to limited deposition and etching process control. Additional layers can provide functionality not inherit to the substrate such as piezoelectricity. For the TPoS resonators, both bulk and surface micromachining processes are utilized. Bulk micromachining defines the resonant body while surface micromachining establishes the electrode configuration and the piezoelectric transduction.

The process begins with silicon-on-insulator (SOI) wafers (Figure 12), which are composed of two single crystal silicon layers, the device layer and the handle layer, separated by a buried

silicon oxide (BOX) layer. The silicon device layer thickness will govern the thickness of the resonant body. The performance as shown in later chapters is shown to be dependent on the resonator thickness. The wafers are sent to an outside source have the piezoelectric stack sputtered (Figure 13) using a proprietary process [55].

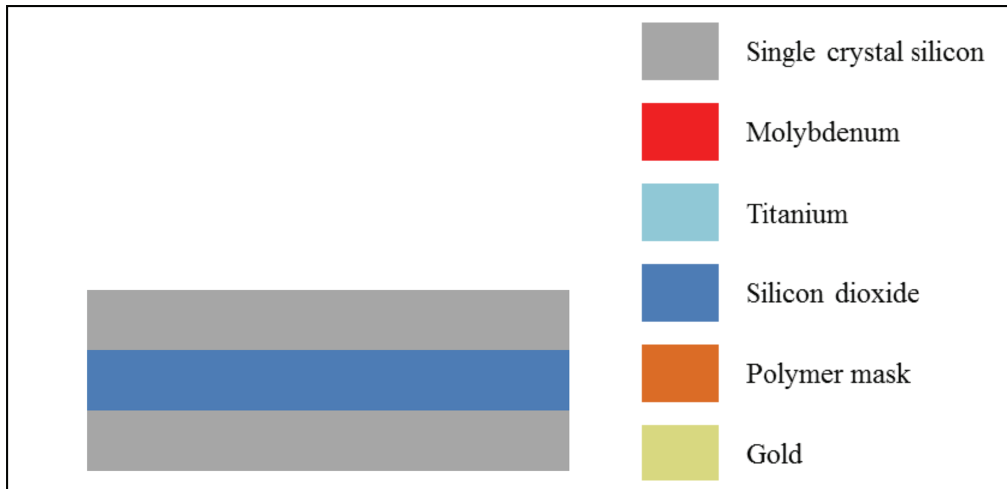

Figure 12: Blank SOI wafer (thickness not to scale on any of the schematics)

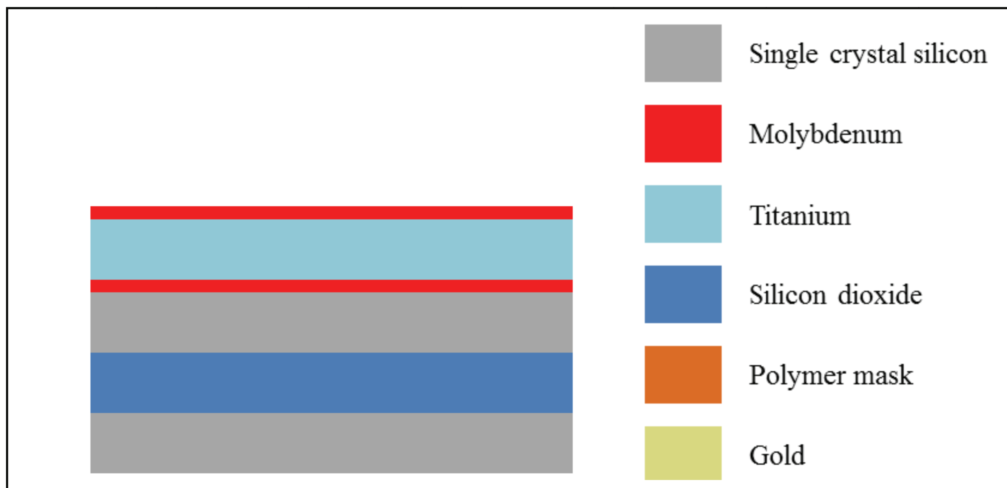

Figure 13. SOI wafer after sputtered films have been deposited

Surface micromachining steps form the actuation structure. First the top metal layer, molybdenum (Mo) is patterned with a photoresist mask, often called a soft mask, in sulfur hexafluoride (SF_6)

and oxygen (O_2) plasma in an inductively coupled plasma (ICP) reactive ion etcher (RIE). The etch stops on the aluminum nitride (AlN) since the etch rate of the AlN in a SF_6/O_2 plasma is significantly small. The photoresist mask is removed with acetone in an ultrasonic shaker and the wafer is rinsed with isopropanol then deionized water. The wafer is baked on a hotplate at 110C. After the soft mask is removed, a hard mask composed of 500nm of silicon dioxide deposited using plasma enhanced chemical vapor deposition (PECVD) is placed on the top of the wafer. During the wafer transfer, the platen temperature must be lowered to 200C to prevent the oxidation of the top molybdenum electrode in atmospheric environment. Once under vacuum, the platen temperature can increase and stabilizes at the deposition temperature of 250C. To deposit SiO_2, a plasma of silane, (SiH_4) and nitrous oxide (N_2O) in a 1Torr atmosphere of helium (He) and nitrogen (N_2) is created above the wafer. The hard mask is patterned in a similar fashion to the top molybdenum layer using a soft mask and an ICP with a trifluoromethane, CHF_3, plasma. The underlying AlN provides an excellent etch stop layer for the CHF_3 dry etch. However, as the CHF_3 etch proceeds it deposits a thin polymer on the sidewall and on the AlN layer. If the polymer is not removed from the sidewall and the top of the AlN, it will be released and deposited on the wafer as the hard mask is removed. To remove the polymer, a dry O_2 etch is used. The oxygen etch is available since the top molybdenum electrodes are covered with the silicon dioxide hard mask and the bottom electrodes are still covered with aluminum nitride. Otherwise, the oxygen plasma will oxidize the Mo electrodes thereby destroying the sample.

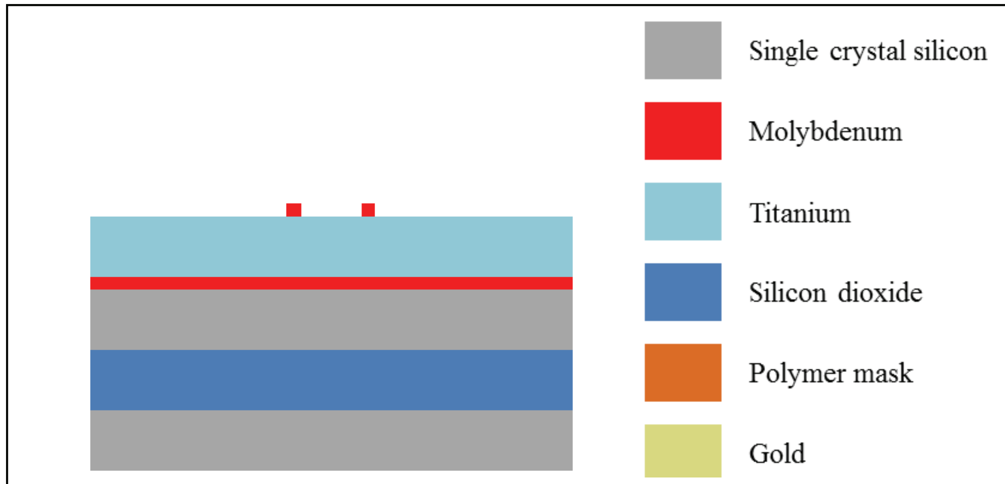

Figure 14: Wafer after top electrode dry etch

To gain access to the bottom electrode, the exposed aluminum nitride (AlN) layer is removed in a heated basic solution usually a mixture of potassium hydroxide (KOH), or tetramethylammonium hydroxide (TMAH), and deionized (DI) water at a ratio of approximately 1:4 (basic:water) at 85C. The wet etch takes only a minute to remove 1µm of AlN and stop on the bottom molybdenum layer. If the wafer is in the solution for too long, two problems will arise. First the basic solution will migrate through pinholes in the bottom Mo layer and begin attacking the underlying silicon substrate. This can lead to delamination of the molybdenum layer and destruction of the sample. Second, the solution will roughen the backside of the wafer. The roughened wafer side can pose a problem in further lithography steps. Adding a thin silicon dioxide hard mask on the backside of the wafer can mitigate the second risk. The silicon dioxide can be added immediately after the top hard mask is deposited. Both hard masks are removed by submerging the wafer in a bath of buffered oxide etch, a mixture of ammonium fluoride (NH_4F) and hydrofluoric acid (HF), for 2 minutes. The buffering salt, ammonium fluoride, provides a stable etch rate for silicon dioxide in hydrofluoric acid.

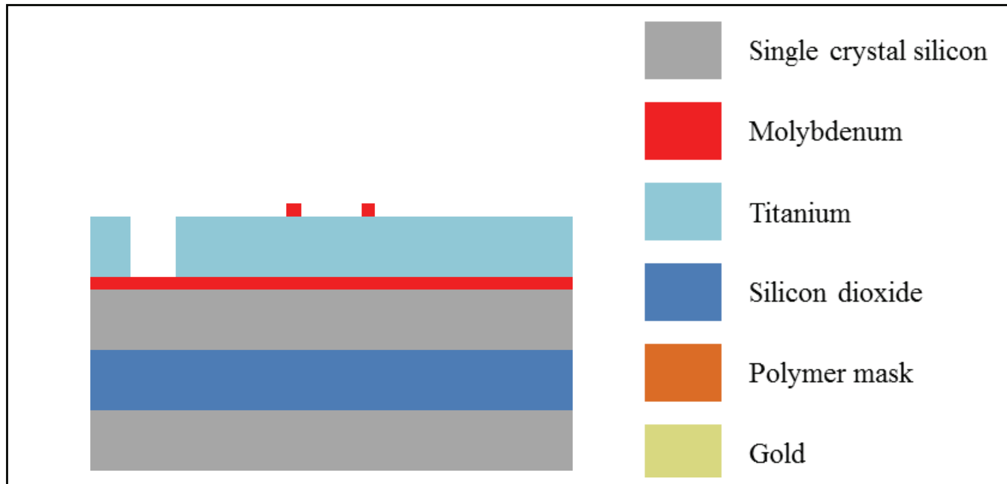

Figure 15: Wafer after aluminum nitride wet etch.

To promote electrical contact and reduce contact losses during probing, gold (Au) must be overlaid on top of molybdenum testing pads where the probes will land. If the Au is not present, the molybdenum will oxidize over time and continual probing becomes more difficult. To pattern the gold, a lift-off step is used. A photoresist mask is patterned using a standard photolithography procedure. After which a thin layer (10nm) of chromium (Cr) and the layer (100nm) of gold is deposited using sputtering. Without the adhesive layer of chromium, the gold will flake off when mechanically probed as its adhesion to molybdenum is fairly poor. Typically this process is done in a high-vacuum evaporation system due in part to its point-source nature. With a point source, sidewall coverage by the evaporated metal will be minimal. These gaps provide a break in the film to ease of the metal's removal from the top of the photoresist mask. When an evaporator is unavailable, a sputterer can be used so long as the throw distance, the distance from the source to the wafer, is sufficiently large (approximating point source) and the deposition time is low (to reduce sidewall amount). The photoresist mask is removed using an ultrasonic cleaner and acetone. The gold deposited on the unexposed photoresist areas will lift-off while the gold in the areas where the photoresist was developed away, in this case the probe pads, will remain.

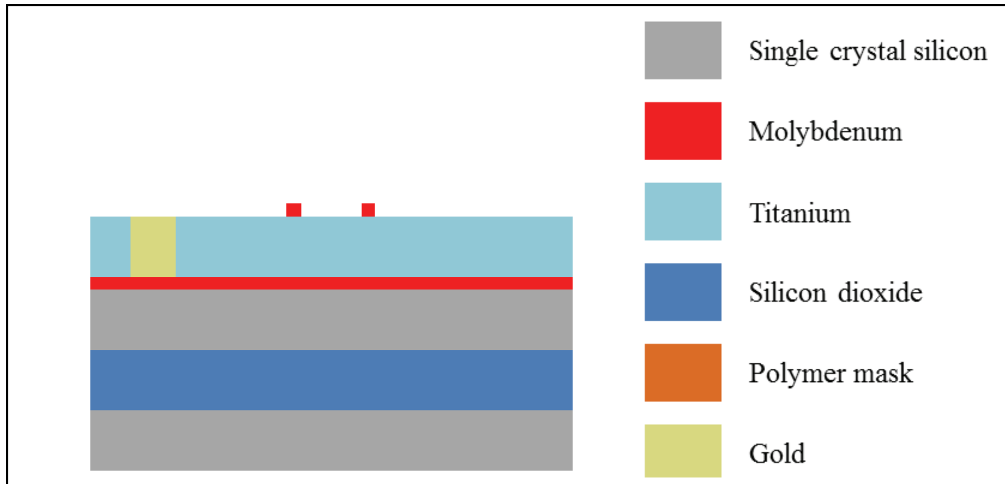

Figure 16. Cross section of a resonator through the Au pad lift-off step.

Next, a thick (~3-5μm) silicon dioxide hard mask is deposited on both sides of the wafer. The top the mask must be significantly thick to survive the topside AlN plasma etch and the subsequent topside deep silicon trench etch. The selectivity of AlN to SiO_2 and Si to SiO_2 is approximately 2:1 and 10:1 respectively. Some process margin and overetch should be accounted so a thicker-than-calculated silicon dioxide mask is used. The topside hard mask is etched similar to the previous hard mask with a thicker photoresist (~5μm). The thicker resist and thick hard mask make it more difficult to correctly transfer small features from the photomask to the wafer. Due to this, the minimal feature size for the top-side mask is ~5μm. After the hard mask is etched and the soft mask is removed with an ultrasonic acetone bath, the exposed AlN is etched with in chlorine (Cl_2) plasma. A significant amount of process margin must be built into this etch. If the etch is incomplete and the process proceeds, any remaining AlN becomes a high selectivity mask for the next etch steps creating processes irregularities. The dry etch can continue through the bottom Mo electrode but should be stopped before it continues into the device silicon layer. For silicon, the Cl_2 etch is relatively isotropic, when compared to the Bosch process, and will ruin the resonator body's sidewalls if left to proceed for a long time.

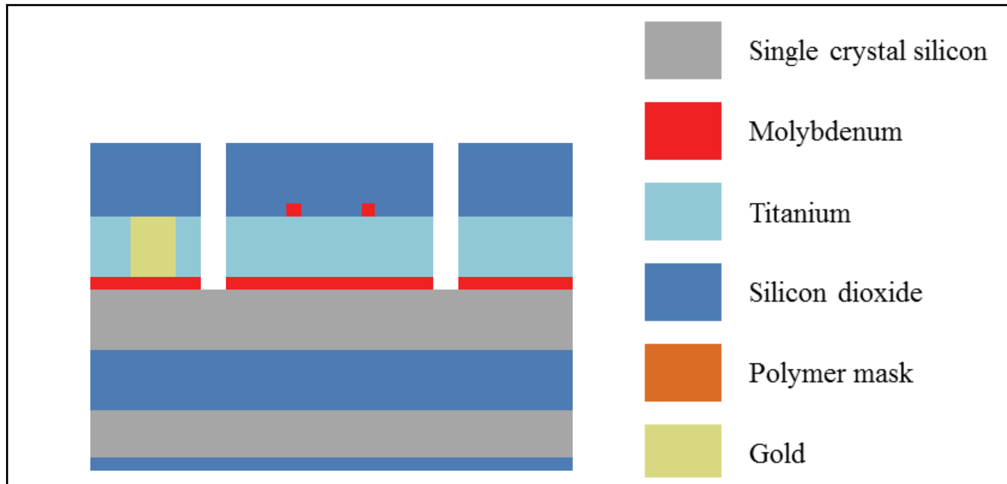

Figure 17. Resonator through the stack etch process step prior to backside patterning.

Once the top AlN is etched, hard mask for the etch cavities is patterned. The backside can etched using a dry Bosch process or a wet KOH process. Since the etch cavities must be etch from the backside, a mask aligner with backside microscopes is used to ensure the mask on the backside lines up correctly to the mask on the front. Unfortunately the process relies on bookmarked alignment marks instead of actively aligning in-situ. Due to this procedure, a possibly translational alignment error of upwards of 5µm can occur, and the mask drawings allow for this error. The backside SiO_2 mask is etched with a $CF_4/0_2$ plasma like previous hard masks. Unlike previous steps though, the remaining photoresist is not removed for the dry Bosch process etch and will provide the initial protection for the deep silicon trench etch. Since the handle wafers are typically 400-600µm thick and the selectivity in the Bosch process for $Si:SiO_2$ is around 100:1, the thick 4µm backside hard mask is insufficient to handle the long deep silicon trench etch. The remaining photoresist provides the added masking layer to etch through the handle layer silicon without losing the integrity of the masked regions.

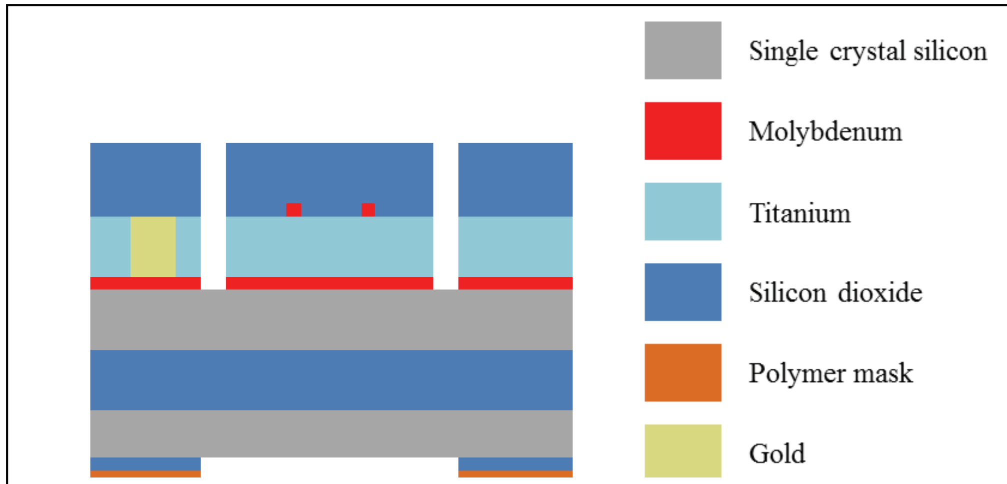

Figure 18. The wafer after the backside mask has been etched. The wafer is now ready for two deep silicon trench etch steps.

For the silicon trench etching, two different recipes are used for the top and the bottom exposed silicon. For top silicon etch it is critical that the etching stops on the buried oxide layer without notching. Notching, also known as footing, occurs when the etch process reaches the buried oxide. The ions from the etching plasma are accelerated by the generated DC bias are embedded in the buried oxide layer and create a charged surface in the insulator. The surface charge then causes reactive species to deflect sideways at the insulator and begin etching the silicon laterally. To counteract the notching, a low frequency (380kHz) pulsed RF generator is used instead of a typical high frequency (13.56MHz) power supply for the applied platen power [56]. The pulsed supply allows the embedded charge on the buried oxide to be dissipated and prevents the reactive species' deflection. Switching to the lower frequency though reduces the etch rate and thereby restricts its use from the bottom silicon etch.

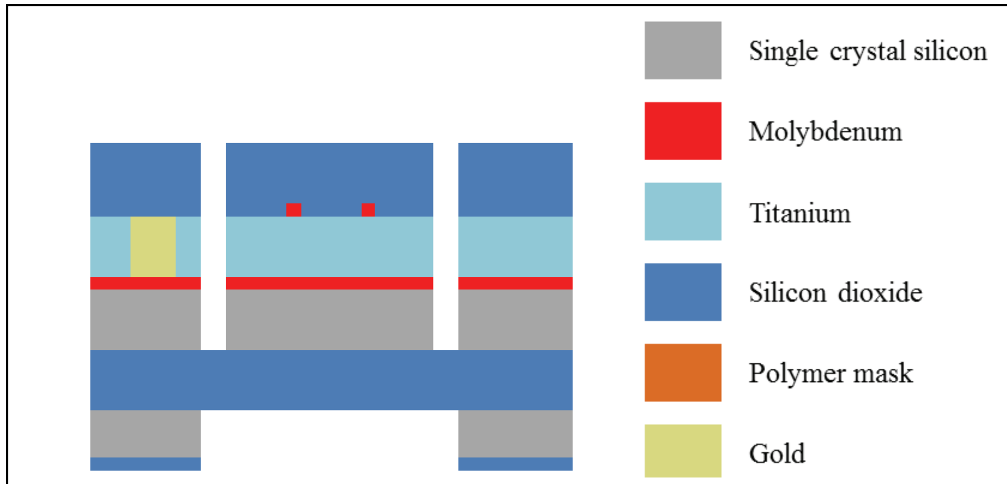

Figure 19. The wafer after both silicon trench etches. The wafer is now ready for release.

In the case of a wet alkaline etch, the etch window is larger than the dry etch due to its specific anisotropic nature. For a wet alkaline etch, the etch rate for the <111> silicon plane is significantly slower than the etch rate in the <100> or the <110> direction. The result is a 54-degree etch-profile. To etch through a 400µm single crystal silicon handle layer, an additional 235µm buffer around the desired etch window must be added. This greatly reduces the prospective good die per wafer.

To utilize the wet alkaline etch for this process first, the front side of the wafer must be protected. A polymer that is resistant to alkaline chemicals, Brewer Science's Protek B3 is spun on. The thickness of the polymer protection is controlled by spin speed with a maximum thickness of around 5µm. This thickness also sets the limit for how deep trenches can be and therefore how thick the resonant silicon body can be. The polymer must have no breaks in its coverage otherwise the wet etchant will have a pathway to etch the topside. However with a deep (out-of-plane dimension) trench (approximately equal to the polymer thickness), the spun-on polymer is unable to provide adequate protection on the sidewalls of the trench. To circumvent the limit on the depth of the trenches, narrow trenches (in-plane dimension), approximately equal to the thickness of the polymer are utilized in the place of normally wide trenches. In this configuration,

the polymer is viscous enough to flow across the small gap evenly and therefore have no breaks in its film. In addition to the topside, the edge of the wafer must be protected or otherwise the top protection layer will begin to peel at the wafer's periphery. While for industrial applications the edge is protected during the spin process through a backside edge coating technique, this process was unavailable for the resonators fabricated for this work. Instead, the wafers' edges were carefully coated manually by carefully hand rotating through a dish of the polymer. Certainly the thickness of this edge layer is unable to be controlled but since only the wafer's edge is coated in this manner, any process nonuniformities, residue or thermal stress from thick polymer, occur far from the target devices. Once the wafer is prepared, 90C 15% TMAH in deionized water by volume bath is used to etch the handle single crystal silicon. To etch 400um, the wafer remains in the etchant for approximately thirteen hours. After the wet alkaline etch (Figure 20), the wafer is rinsed in deionized water, and the wafer protection is removed in a bath of Shipley 1165 resist stripper heated to 85C for twenty minutes. The wafer is then rinsed with isopropanol and deionized water.

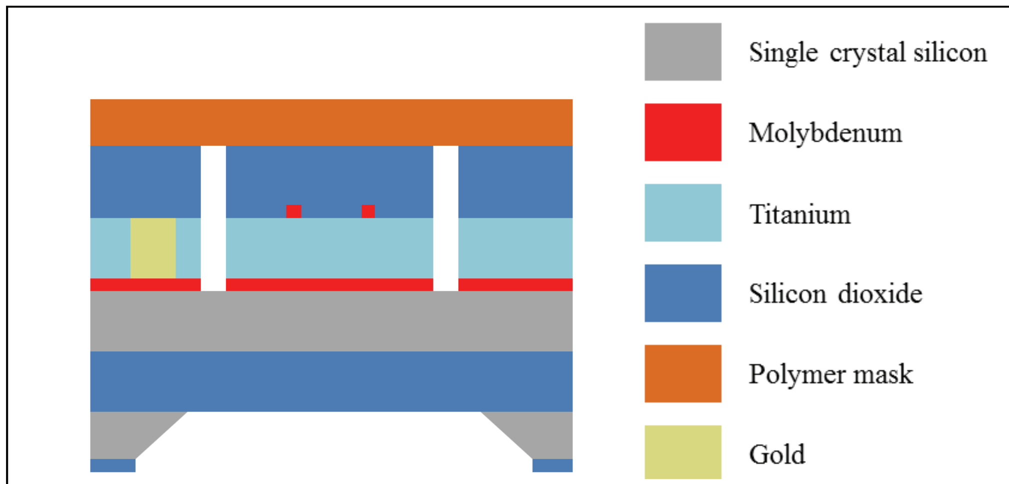

Figure 20. A schematic of the wafer after an alkaline etch of the backside silicon. The top layer is the spun-on protection layer.

The final step for the wafer processing is a buffered oxide etch for ten minutes at room temperature. During this hydrofluoric acid based etch, both the top oxide hard mask and the buried oxide layer are removed, exposing the gold probe pads and fully releasing the single crystal silicon device layer. The wafer is dipped into two successive deionized water baths to rinse. The wafer is gently dried with a nitrogen gun. The wafer is heated to 85C for 5 minutes to remove excess water and visually inspected with a microscope to ensure all silicon dioxide has been removed and the devices have been released. SEM images of a few model devices can be seen in Appendix A.

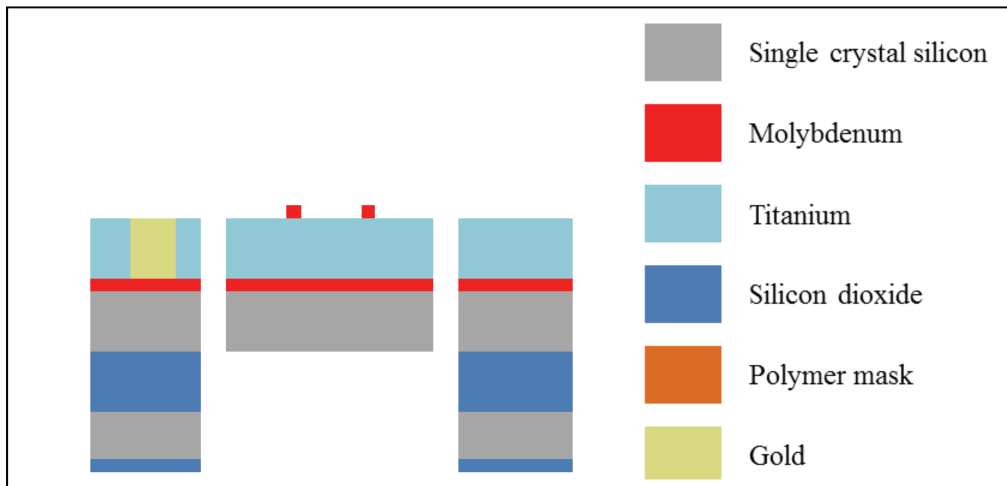

Figure 21: Final device with a dry back side etch after buffered oxide etch to release the structure.

CHAPTER VI

IN-PLANE ACOUSTIC REFLECTORS

In this work, a novel technique to further improve the quality factor of TPoS resonators through the minimization of anchor loss is proposed. In order to enhance the confinement of elastic energy, and consequently improve the quality factor, a pair of properly shaped trenches is etched into the substrate at a fixed distance from the TPoS resonator. Seen in Figure 22, the acoustic reflector trench, around an in-plane resonator, will provide confinement for the normally lost energy. The acoustic reflectors supply an additional surface for the outward propagating wave to reflect and return to the resonator. The quality factor will be improved as the amount of energy leaving the system per cycle is reduced. Simulations and measurements presented in this manuscript support the efficiency of this method.

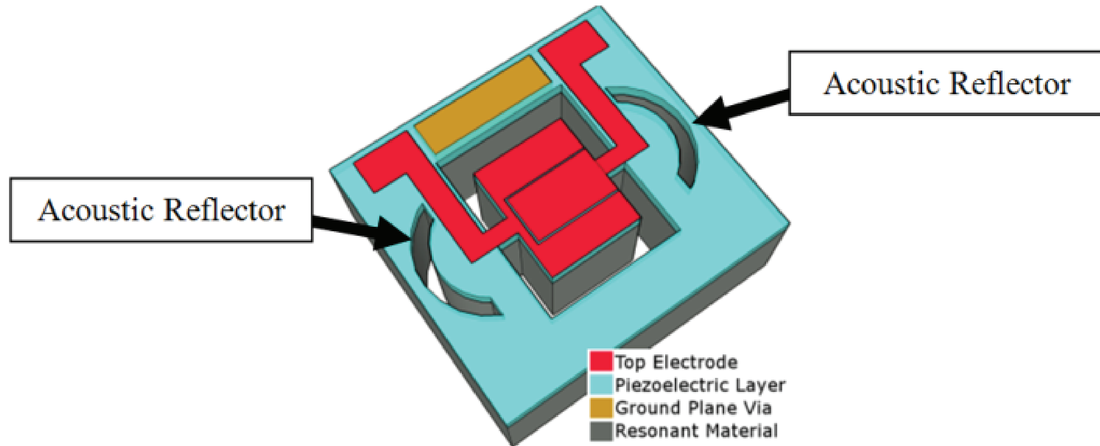

Figure 22. 3D model of a thin-film piezoelectric-on-silicon (TPoS) resonator with acoustic reflectors.

While there has been limited research on anchor loss, the focus has been primarily on out-of-plane loss [19] or flexural-mode in-plane resonators [16,18]. In-plane bulk compression waves resulting from an axially excited tether are mostly unexplored [10,32]. Designs with this mode of anchor loss, such as lateral-extensional resonators, have relied on one-quarter acoustic wavelength tether lengths to reduce effective anchor loss based on the assumption that the substrate is an ideal fixed boundary [15], [57]. However, this assumption is not an accurate approximation, and elastic waves are in-fact propagating into the substrate, thereby making quarter wavelength tether lengths insufficient. If this otherwise lost acoustic energy can be contained and prevented from radiating into the substrate, the resonator's performance will improve.

The proposed acoustic reflector trenches added around the resonator in this work must match the shape of the wavefront that will impinge on the trench. If the wavefront is not matched, the wave will be partially scattered, and the quality factor enhancement will not be optimum. In addition, proper positioning must be found so the wave returns to the resonator in-phase such that destructive interference with the resonator's motion is avoided.

The resonator's high quality factors (Q) and small size make them an ideal candidate for several existing and future applications [58]. Since higher Q can result in greater stability in oscillator circuits [4], improved resolution in resonant sensors [2], and higher selectivity in filters [3], enhancing Q is of great importance.

To model the anchor loss as a one dimensional (1-D) system, first the resonator is assumed to be an ideal acoustic source connected through the tether to the substrate which acts as an acoustic load impedance. In general, the acoustic impedance (Z) is defined as the ratio of the pressure (p) to the velocity (v) (particle velocity in 1-D, volume velocity in 3-D) as shown in equation (1) [59].

$$Z = {}^{\rho}/_{\upsilon} \tag{16}$$

Much like the electrical equivalent, the acoustic impedance can be a complex number where the real portion describes the dissipative element and the imaginary portion signifies the storage component. Now, if the tether width and thickness are significantly smaller than the acoustic wavelength, the longitudinal wave traveling down the tether can be modeled as the displacement in the one-dimensional system [60]. This simplified configuration is equivalent to the electrical circuit shown in Figure 23 and the minimization of acoustic loss is equivalent to designing the mechanical structure such that the impedance seen by the source (resonator) is zero (the resonator end of the tether is free to move).

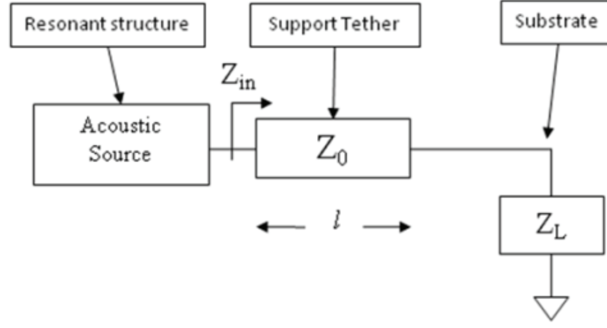

Figure 23: Electrical equivalent of resonator-tether-substrate acoustic interaction

Suppose the substrate end of the tether is fixed and allows no movement (the load impedance is infinity). Complete in-phase reflection would occur when the tether length is a quarter acoustic wavelength, or λ/4. In other words, the quarter acoustic wavelength transforms the infinite impedance of the substrate to zero impedance at the source. This phenomenon is common in electrical transmission lines and can be described using the equation below [61]:

$$Z_{in}(l)=Z_0\frac{Z_L+jZ_0\tan(\beta l)}{Z_0+jZ_L\tan(\beta l)} \tag{17}$$

where is the substrate acoustic impedance, Z_0 is the tether characteristic acoustic impedance, Z_{in} is the acoustic impedance seen by the resonator, β is the wavenumber, l is the length of the tether. If the substrate is fixed equation (2) reduces to:

$$Z_{in}(l)=-jZ_0\cot(\beta l) \tag{18}$$

and Z_{in} is zero at $\cot(\lambda/2)$ or $l = \lambda/4$. The opposite case of zero impedance at the substrate results in:

$$Z_{in}(l)=jZ_0\tan(\beta l) \tag{19}$$

and the impedance seen by the resonator is zero at $\tan(\lambda)$ or $l = \lambda/2$. In these two ideal cases, no energy would be dissipated into the substrate and complete energy reflection back into the resonator will occur.

In reality, the acoustic impedance of the substrate is a complex number comprised of both dissipative and reactive components. Therefore, complete reflection is not achievable through tether design and also the optimal tether length may not occur at $\lambda/4$. However, the energy loss can be mitigated by creating in-plane reflectors in the substrate. To create in-plane reflectors, a trench can simply be etched into the substrate. The air interface at the trench provides a very small (approximately zero) acoustic impedance which could be transformed to a near zero or near infinite impedance at the tether-end of the substrate based on the distance from the tether. Therefore, the basic design rule in order to substantially reduce Z_L is to position the trench at $\lambda/2$ from the tether. On the contrary, if the trench is positioned at $\lambda/4$ from the tether a substantial increase in acoustic impedance will be seen. For each one of these cases, the tether length can be tuned to create very low impedance at the resonator. In the case where Z_L is very large the lowest impedance seen at the source still occurs at tether lengths of odd multiples of $\lambda/4$. For the case in which the substrate impedance is small, the minimum Z_{in} occurs at the tether lengths of even multiples of $\lambda/4$, seen in Figure 24. It should be mentioned that the aforementioned design rules are only accurate if the energy dissipation is negligible (Z_L is purely reactive) which doesn't necessarily hold.

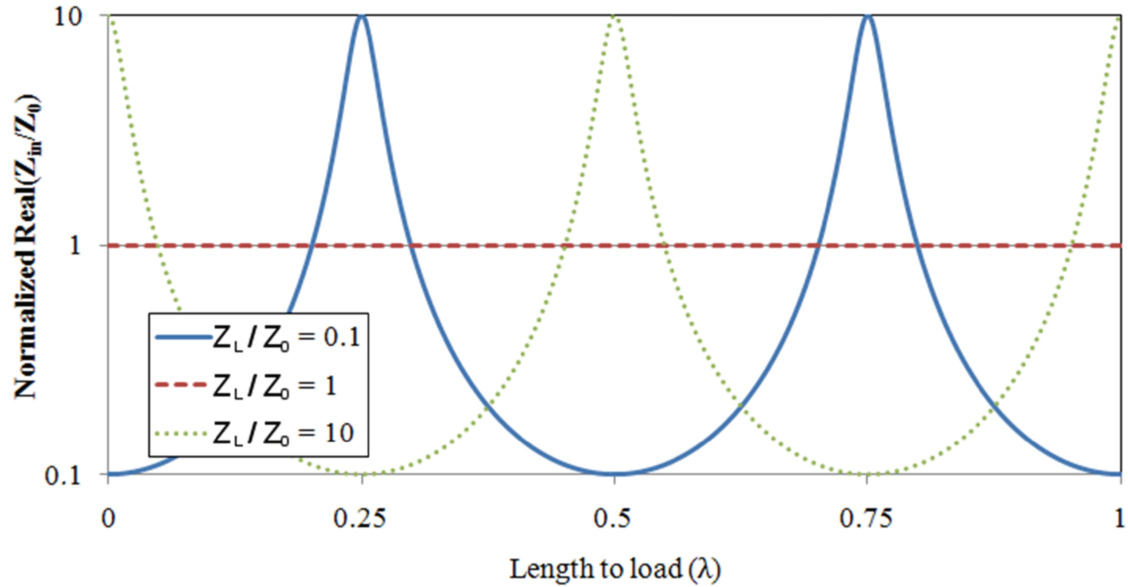

Figure 24: Changes in the normalized impedance seen by the resonator depending on length and the ratio of load impedance to the characteristic impedance of the tether.

For low frequencies at which the wavelength is relatively large compared to the tether dimensions, choosing odd multiples of $\lambda/_4$ for the tether length is not practical because the structural integrity of the device would be compromised. Therefore, we can choose very short tether lengths (close to zero) and place the reflector at $\lambda/_2$ away from the tether. For high frequencies, care should be taken in extending the results of this discussion since at that point the size of the tether is close to the wavelength and the 1-D treatment of the problem does not necessarily hold. Nevertheless, either a short tether ($\lambda/_8$) or one equal to $\lambda/_2$ with the reflector positioned at $\lambda/_2$ will be shown to provide ample improvement in Q at relatively high frequencies (110MHz).

Simulation

While the simplified 1-D analysis can provide a generalized guide, a more complex model from two-dimensional (2-D) and three-dimensional (3-D) simulations is required to design the acoustic

reflector's shape and distance from the resonator's tether. To estimate the efficacy of the acoustic reflectors, a 2-D wave simulation and a 3-D coupled domain piezoelectric simulation were performed in COMSOL Multiphysics. While the 2-D simulation is less demanding computationally, it is meant to provide quick insight in comparison to the taxing, detailed frequency response achieved by the more complex 3-D model.

4.1. 2-D acoustic wave simulation

In this study, the resonators with dimensions 108μm (width) and 54μm (length) are attached with tether lengths of 9μm, 18μm, and 27μm, to large semi-circular substrates without (Figure 25 (a)), and with (Figure 25 (b)) reflector trenches. The time-harmonic Helmholtz plane-wave equation$-\nabla\cdot(\nabla u)-k^2u$ =0 (20) and boundary conditions (12-15) govern the simulation [62].

$$-\nabla\cdot(\nabla u)-k^2u\;=0 \tag{20}$$

$$-\nabla\cdot(\nabla u)=0 \tag{21}$$

$$n\cdot(\nabla u)+iku\;=2ik \tag{22}$$

$$n\cdot(\nabla u)+iku\;=0 \tag{23}$$

In the above equations, u is the perturbation, k is the wave number, and n is the normal direction from the boundary. The strain-free boundaries, defined by (13), confine the acoustic energy created by the acoustic line source given in (14) seen in Figure 25. The boundary across from the acoustic source will reflect the acoustic wave, setting up the standing wave that defines the mode shape, therefore allowing only one source to be sufficient. The only loss mechanism in this simulation is the absorptive boundary, taking the form of (15). Any acoustic wave impinging on this surface is lost and not returned to the system. In assuming an isotropic and linear acoustic medium, the structural material's complexities are abstracted into only a single parameter,

acoustic wavelength, λ. Then, to establish a third harmonic lateral extensional resonance inside the simulated device, the acoustic wavelength is selected to be 2/3 of the device's width, in Figure 25.

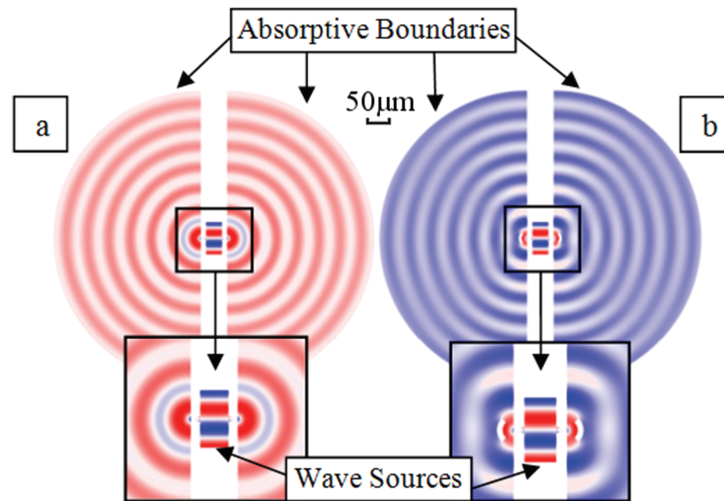

Figure 25: 2-D models of third harmonic lateral extensional resonators without (a) and with acoustic reflector trenches showing the resulting perturbation fields. Please note the color intensity in the substrate has been increased to better highlight the perturbation in this region. All unspecified boundaries are strain-free.

Once a wave is generated inside the simulated resonator, acoustic energy radiates out through the tethers, which results in the circular outward propagating perturbation fields shown in Figure 25 The inset highlights the perturbation field in the resonator and its proximity. The acoustic wave propagating into the substrate takes the form of a circular plane wave centered at the end of the tether. To gauge the effectiveness of the acoustic reflectors, the displacement of the nodes through the middle cross-section line of the model for different resonator designs are plotted in figure 26. The design with reflectors shows the effect of constructive and destructive interference as the reflected waves are returned in-phase and out-of-phase, respectively. The largest standing wave is seen in the design with a reflector distanced a half wavelength to the resonator's tether.

The amplitude of the perturbation is also significantly smaller in the substrate for the device with reflector.

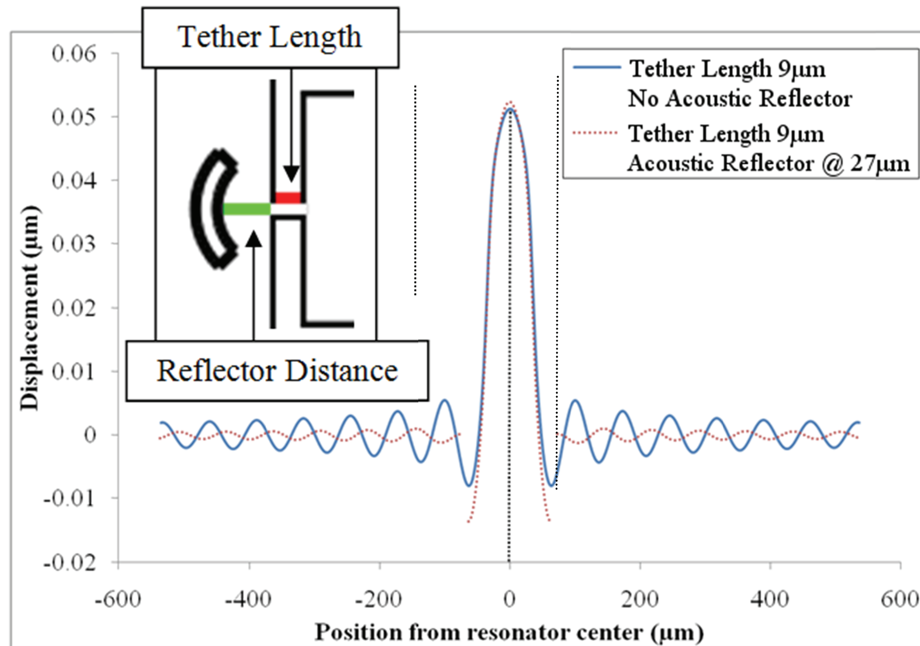

Figure 26. Perturbation through the center of the 2-D simulation without and with acoustic reflectors. The inset shows a 2-D representation of half of the resonator. The dashed line shows the center of the resonator on both the plot and the inset.

4.2. 3-D coupled domain simulation

To further reinforce the predicted behavior for the acoustic reflectors, a more complex simulation model including the stack of piezoelectric on silicon was built using COMSOL Multiphysics. In this study, two domains, structural mechanics and electrical, were coupled using a piezoelectric layer, namely aluminum nitride. The resonator, tethers and the substrate are composed of anisotropic silicon and rotated to the desired (100) orientation. Since piezoelectric aluminum nitride is significantly thinner (1μm) compared to the silicon thickness (25μm) the mesh density in the interface region is substantially increased. Therefore, to prevent further computation and memory requirement inflation, the aluminum nitride is only covering the resonator region as

opposed to the entire structure. Using the dimensions of 108µm (width) and 54µm (length) for the single-crystal silicon structure, the simulated third harmonic lateral-extensional resonance frequency is approximately 110MHz.

Two sources of loss were included in the model: electrical loss and a perfect matching layer (PML) to mimic anchor loss. For the electrical loss, the electrode resistivities were selected such that their impedance matches the target 50Ω series source and load termination impedances. By selecting the top boundary of the input electrode as the source plane, the resistance seen by the resonator back to the device is 50Ω. Likewise, if the bottom boundaries of the output electrodes are selected as the measurement planes while grounding the output electrodes' top boundaries, the 50Ω load will be in series with the resonator.

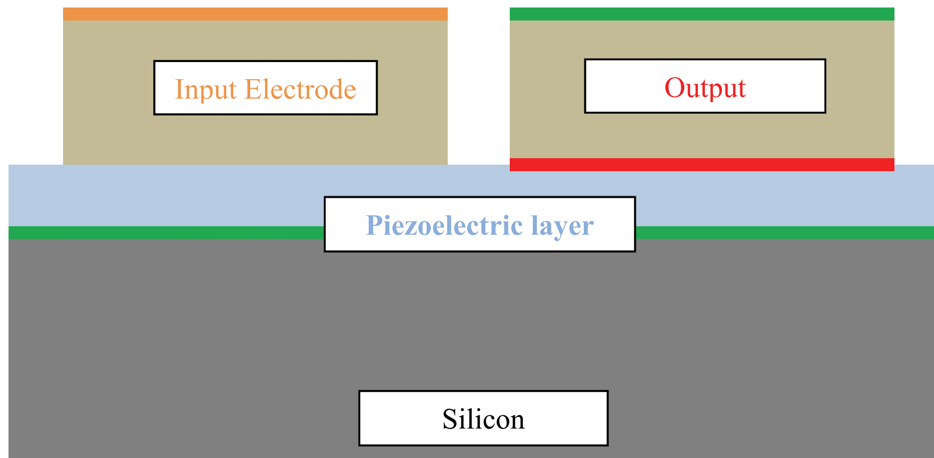

Figure 27. A portion of the cross section through the resonator's length to highlight the electrical simulation's boundary conditions. Green lines are the ground planes. Orange and red lines show the electrical input and output planes respectively. The light blue is the piezoelectric layer while grey is the single crystal silicon. The tan blocks are electrical-only components that have a material resistivity such that the total source impedance and total load impedance are both 50Ω.

To model anchor loss, the substrate is terminated with a PML as seen in figure 28. The PML was initially applied to electromagnetic problems [63] but has been extended to elastic structures and

more recently used to characterize out-of-plane anchor loss in a disk resonator [64]. To design the PML, a complex-valued change of coordinates will be applied to the anisotropic silicon's material properties to create a material that will attenuate any wave from that medium using:

$$\epsilon_{PML} = \tilde{\epsilon}_{Si} \det(\Lambda) \tag{24}$$

$$\rho_{PML} = \tilde{\rho}_{Si} \det(\Lambda) \tag{25}$$

where ϵ_{PML} and ρ_{PML} is the perfectly matched layer material's elasticity matrix and density respectively, $\tilde{\epsilon}_{Si}$ and $\tilde{\rho}_{Si}$ are coordinate transformations of the original silicon properties, and Λ is the Jacobian [64]. The coordinate transformations contain the absorptive coefficient, α, which along with the PML length must be chosen to minimize the reflection coefficient at the boundary. As a wave travels through the PML, the wave's energy is absorbed gradually and is ultimately reduced to zero. If the decay is too strong, the wave will be diminished too quickly. The result is that PML's effective acoustic impedance will be substantially different than the substrate, and a reflection will occur at the PML-substrate interface. If the decay is too weak, the wave will bounce off of the opposite PML boundary and return to the system. Both of these cases will lead to a significant increase in spurious modes in the simulation and greatly affect the accuracy of the frequency response [64]. With a properly chosen α and PML length (e.g. 3 and 10μm respectively for the 110MHz simulations) a substantial portion of any wave impinging upon the PML interface is lost from the system, creating the effect of an infinite substrate.

To reduce memory and computation requirements of the simulation, only one quarter of the resonator and substrate is simulated, as seen in figure 28. The inherent symmetries in the third harmonic lateral-extensional mode allow mirrored boundary conditions along quartered slices. A frequency sweep is performed with a source voltage of 1V on the center, input electrode while the output voltage is read from the outer electrode. The quality factor is then calculated by dividing

the peak frequency by -3dB bandwidth of the reverse transmission coefficient, S_{12}. Tether lengths and reflector distances were iterated using Matlab to drive the COMSOL simulations.

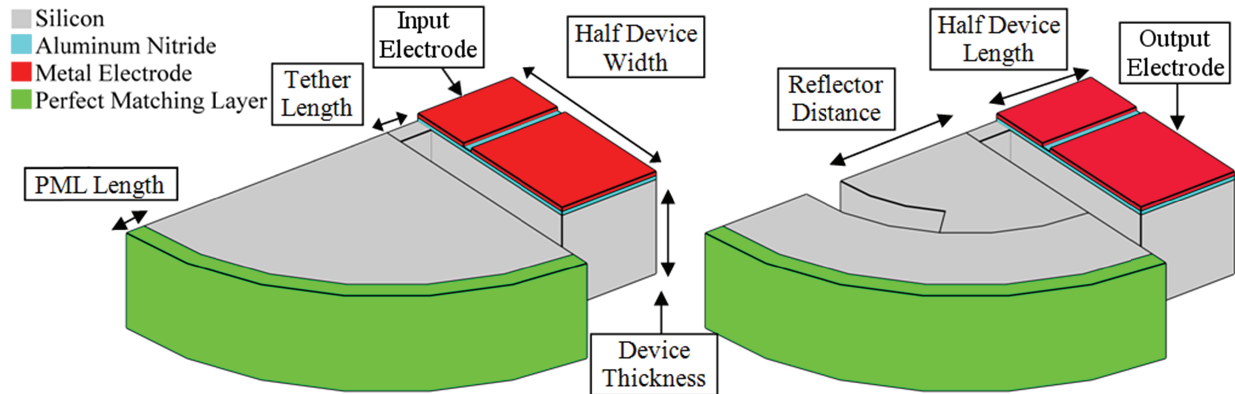

Figure 28. Two 3-D models of one quarter of resonator for coupled-domain simulation showing the pertinent parameters.

Multiple simulations with iterated tether lengths run to find the maximum $Q_{unloaded}$ on the basic design (no acoustic reflector added). The resulted plot is shown in figure 29, and it is observed that the best performance is at slightly less than 0.2λ and not at the conventional $\lambda/4$ with a maximum simulated quality factor of less than 10000. Considering that the conventional optimum tether length of $\lambda/4$ is calculated based on the unrealistic assumption that the substrate-tether boundary is perfectly fixed with no motion, the result of optimal tether length not at $\lambda/4$, can be expected. It should be noted that in all simulations, the trend of the quality factor is significant not the absolute value since the resonator's damping is affected by several loss mechanisms that are not considered in the results.

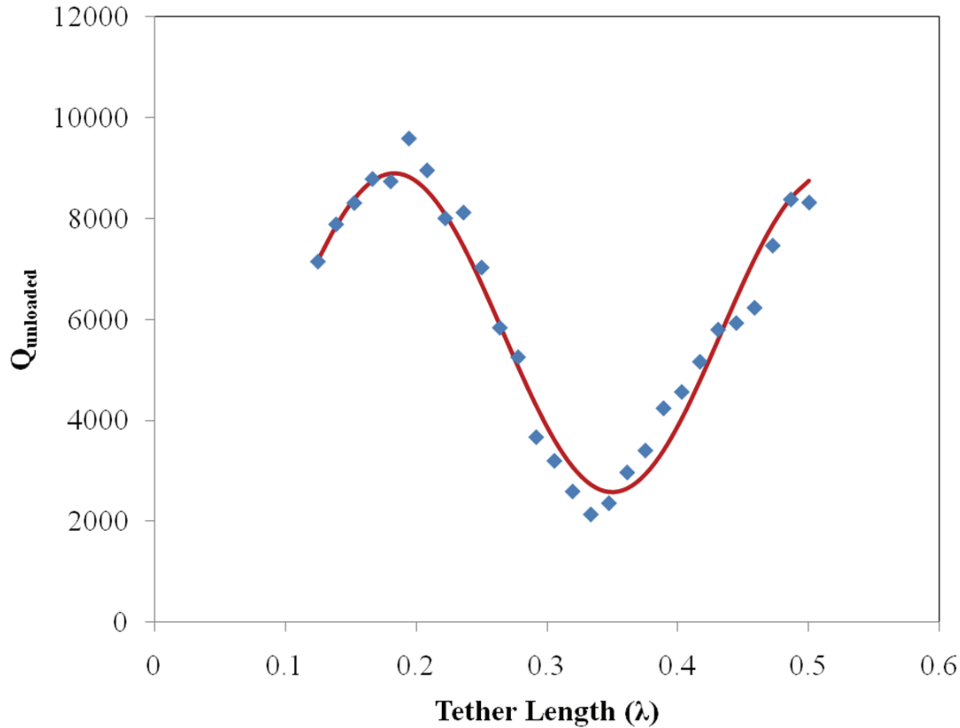

Figure 29. Simulated $Q_{unloaded}$ for third harmonic 110MHz, lateral-extensional, TPoS resonators with no reflector with different tether lengths. The red line is a least squares sinusoidal fit for the data set.

The simulated frequency responses of the basic design (no reflector) and of the two designs in which the reflector is placed at λ/4 and λ/2 from the tether are plotted in Figure 30. The simulated device has the same dimensions as the one used for 2-D analysis and the tether length is 9µm (λ/8). The corresponding mode shapes for the basic and optimum designs are also shown in the inset pictures. As seen the maximum deformation (strain) is significantly less in the basic design relative to the device with properly positioned acoustic reflector. The reflector is confining the wave and preventing it from impinging on the PML that would otherwise absorb it. Consequently, the frequency response shows substantial improvement in the quality factor in the design that incorporates the acoustic reflector positioned at λ/2. However, the use of an acoustic reflector at the wrong distance, λ/4, can diminish Q when compared to the base design.

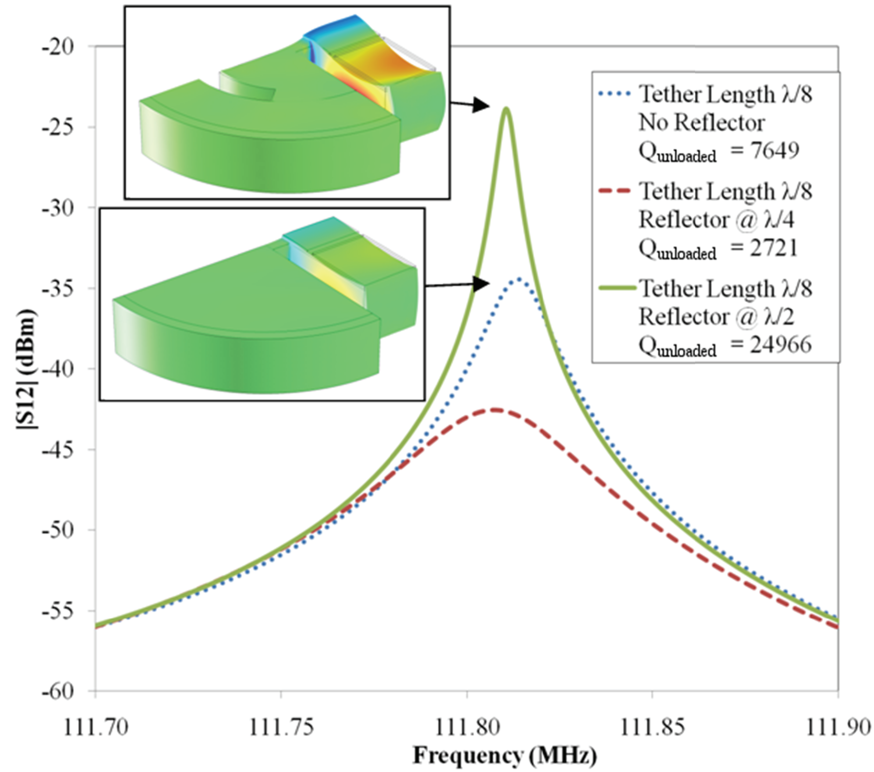

Figure 30: Simulated reverse transmission coefficient, S_{12}, for third harmonic 110MHz, lateral-extensional, TPoS resonators without and with acoustic reflectors. The insets show the strain (color) and the structural deformation near resonant frequency. Both figures have the same deformation and strain (color) scales.

Acoustic Reflector Results

As seen in the previous section, the modifications to the resonator-substrate interaction can leave to performance enhancements. However for lower frequency devices, this approach is limited. Since acoustic wavelength for lower frequencies can be large, increasing the device width or length can be take up significant about of area on the device. To enhance the performance of the larger devices, adding acoustic reflectors is taken.

5.3. 27MHz Resonators

To examine the acoustic reflectors at relatively low frequency where the support dimensions are significantly smaller than wavelength, first harmonic 27MHz resonators without acoustic reflectors (a) and with acoustic reflectors (b and c) were fabricated in close proximity of each other (figure 31). For a 27MHz fundamental mode resonator, the dimensions of 156μm (width), 234μm (length), and 30μm (thickness) are used.

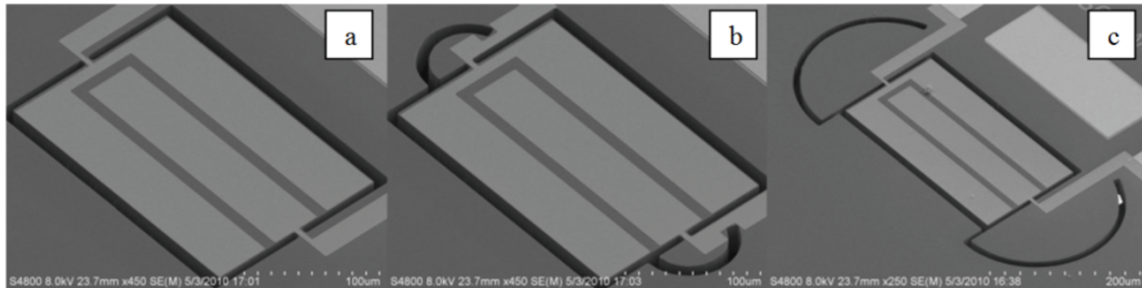

Figure 31. 27MHz fundamental lateral extensional mode without acoustic reflectors (a) and with close (b) and far (c) acoustic reflectors.

This configuration was arrayed around the wafer and resulted in 20 completed devices of each type. The relatively large acoustic wavelength (312μm) provided ample room to measure resonators with distances to their acoustic reflectors much less than a wavelength, λ/20 or ~16μm, as well as 2λ/5 or ~120μm. The tether dimensions, 6μm length and width, were significantly less than the wavelength which effectively allowed the tether to act as an acoustic point source and

thereby more closely following the theoretical transmission-line model seen in Section 3. The performances of all operating devices were collected to gain statistical information on the effectiveness of the acoustic reflectors as seen in table 1 and figure 32.

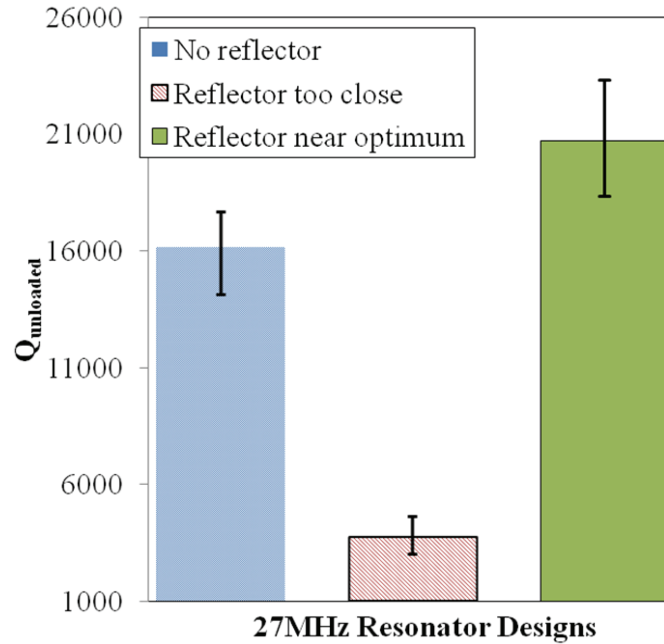

Figure 32. Average measured $Q_{unloaded}$ for 27MHz resonators with error bars denoting highest and lowest recorded for over 20 devices tested.

Table 2. $Q_{unloaded}$ results for 27MHz devices.

Device	Top Performance		Average		Coefficient of variation	
Base 27MHz (no reflector)	17665		16167		0.0626	
With reflector spaced @ λ/20	4571	(-74.1%)[a]	3472	(-77.3%)[a]	0.1340	(114%)[a]
With reflector spaced @ 2λ/5	23326	(32.0%)[a]	20709	(28.1%)[a]	0.0680	(8.6%)[a]

[a] Percent increase compared to the base resonator

When the reflectors were placed at the predicted near-optimum distance, 2λ/5, the result was on average $Q_{unloaded}$ enhancement of over 25%. However, if the reflectors were placed at the wrong distance, λ/20, the result is a detriment to the $Q_{unloaded}$ of over 80% seen in figure 33. The reflector returns the acoustic energy out-of-phase to the device and thereby has a negative effect on the

device. In addition, the coefficient of variation, defined by the standard deviation divided by the mean, for the $Q_{unloaded}$ increased as well. This is expected since the processing can unwillingly adjust the width of the acoustic reflector, pushing it effectively closer or further away from the resonator. Coefficient of variation was used instead of standard deviation to normalize data and remove the negative bias against higher quality factors.

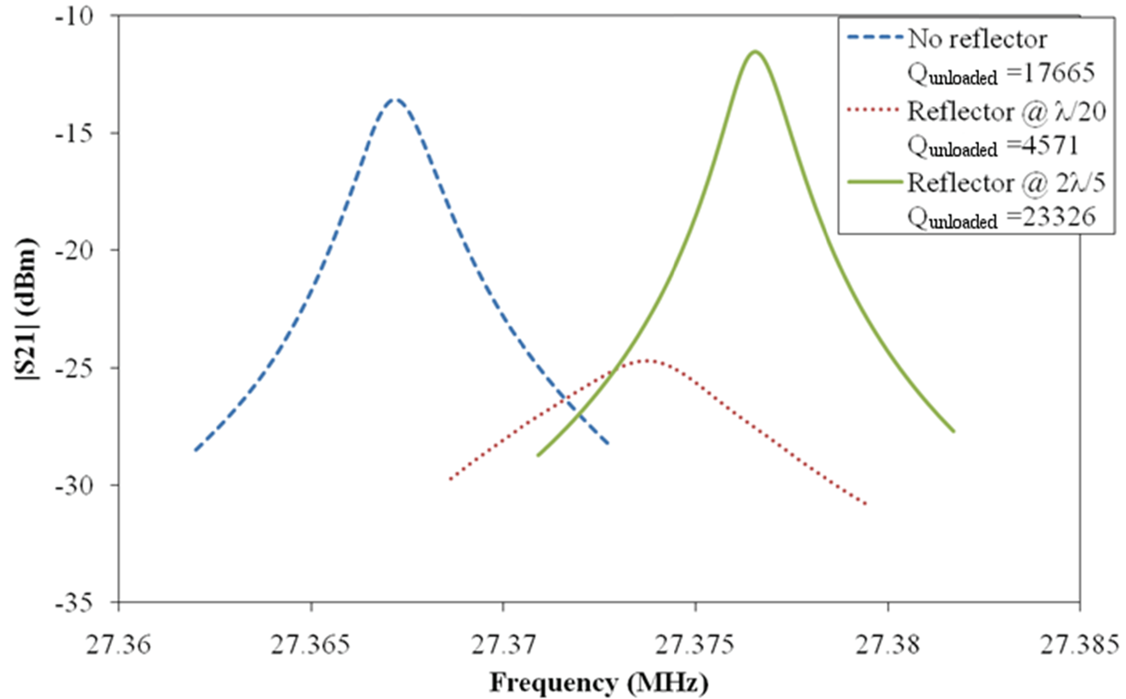

Figure 33. Measured frequency response for the top performing 27MHz reflectors without and with reflectors

5.4. 110MHz Resonators

The third harmonic 110MHz resonators were fabricated on an SOI wafer with 25µm thick device-layer. Like the 27MHz devices, the 110MHz resonators were processed on one wafer with resonator designs repeating in multiple dies across whole area. The combined yield for the 110MHz devices was >83% and all designs had at least 12 individual functional devices while most had 24.

5.4.1. Basic design.

The devices with different resonator sizes, either by extended the device length, or by increasing the harmonic order (device width), were fabricated and multiple devices were tested on a semi-automatic probe tester. Over fifteen devices of each type were tested to gauge their performance. The average and maximums were then plotted to analyze the trends. In the figures below, the $Q_{unloaded}$ gradually increases as the length of the device increases. The figure also shows a repetitive nature of maximums occurring near quarter wavelengths while minimums occur near half wavelengths as expected by the eigenmode. The motional impedance shows a similar trend. This agrees well with (8), the motional impedance, R_m, decreases with increasing device length as well as increasing harmonic order.

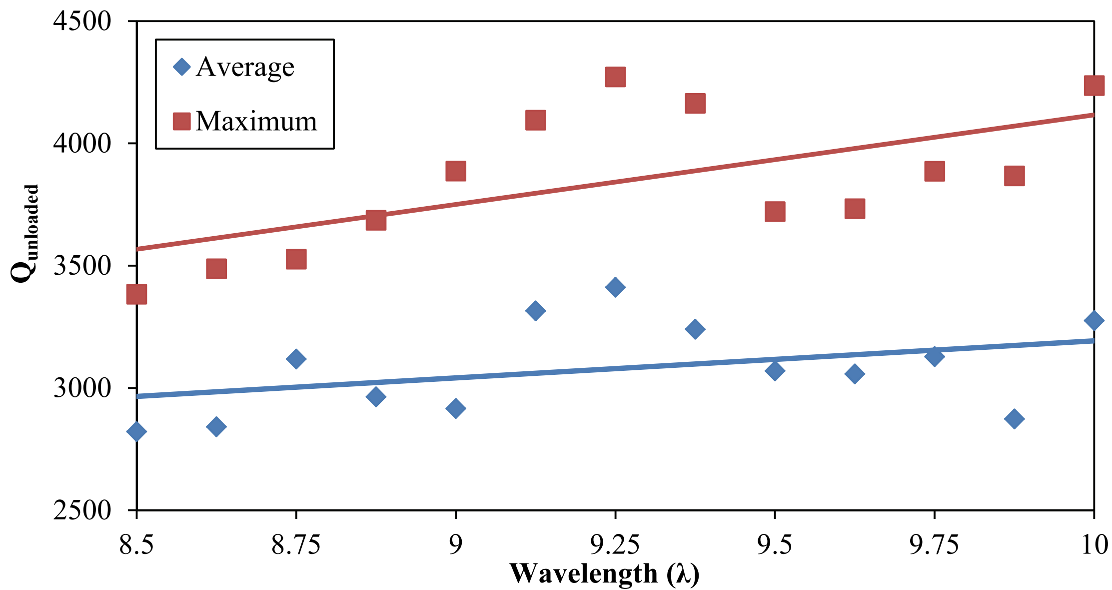

Figure 34. Average and maximum $Q_{unloaded}$ of fabricated ~490MHz single tether devices with varying device lengths.

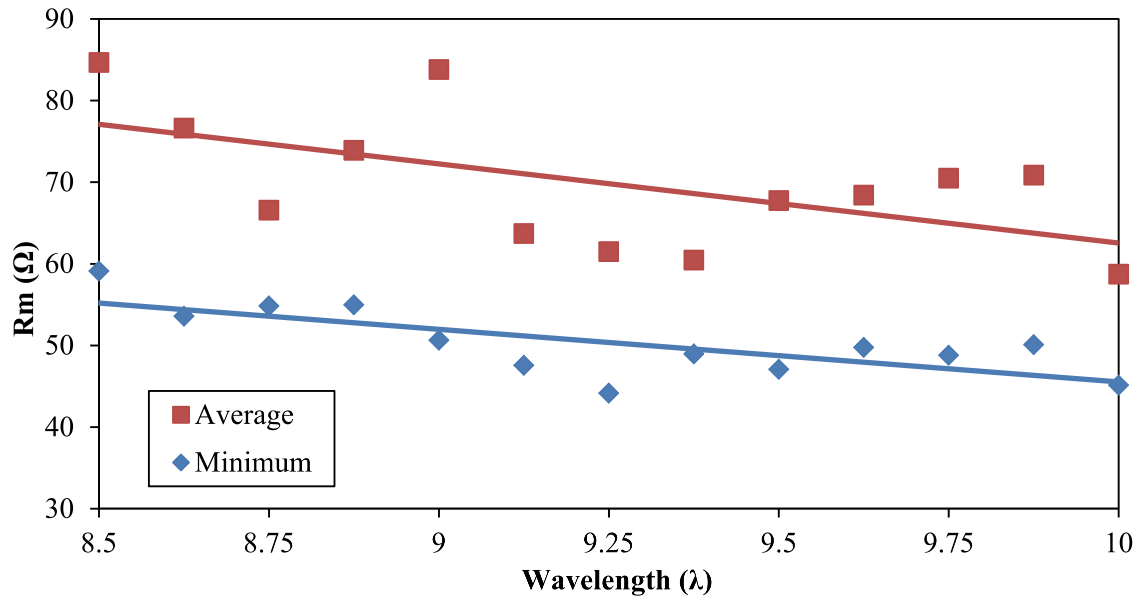

Figure 35. Average and minimum motional impedance of fabricated ~490MHz, single tether devices with varying device lengths.

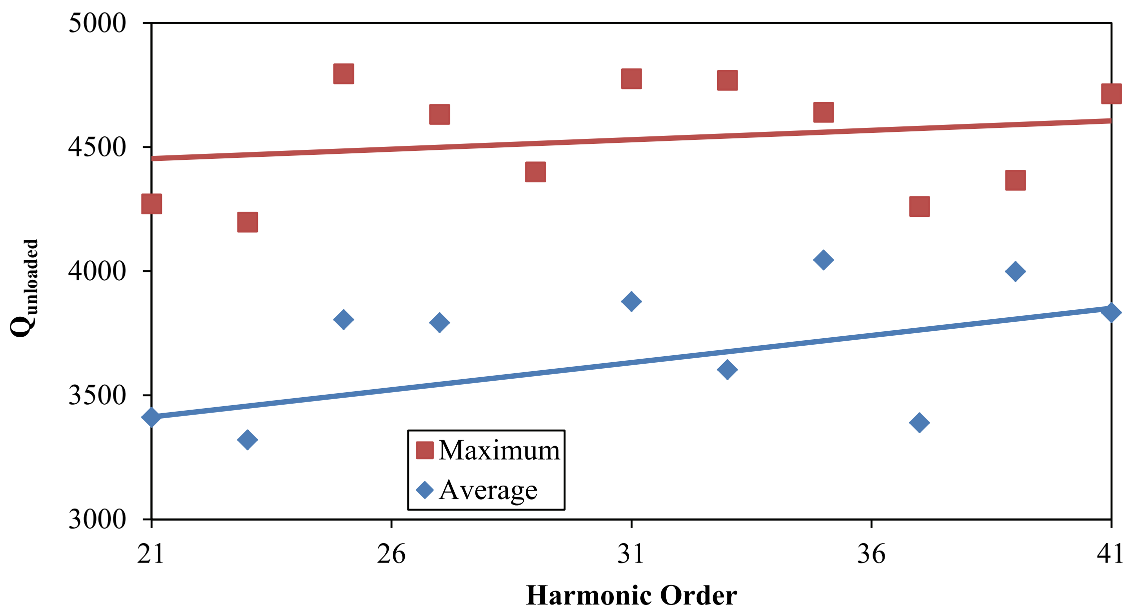

Figure 36. Average and maximum $Q_{unloaded}$ for ~490MHz resonators with different harmonic orders.

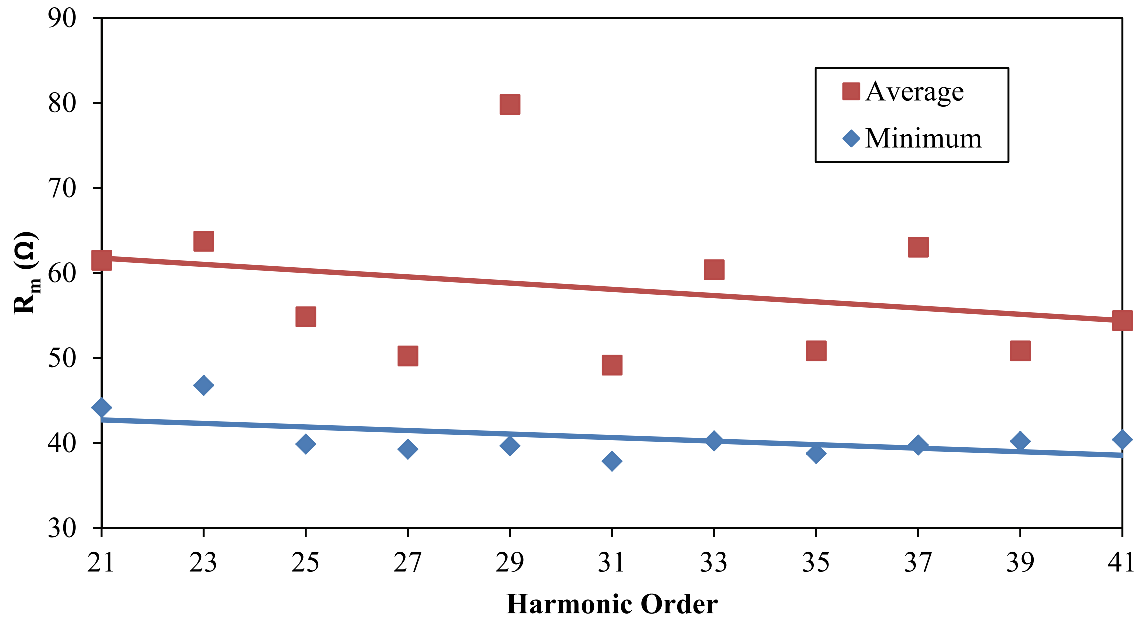

Figure 37. Average and minimum motional impedance for ~490MHz resonators with different harmonic orders.

At first glance the pathway to gain low motional impedance and higher $Q_{unloaded}$, is to increase resonator size either by harmonic order (width increase) or device length. This is not without difficulties though as seen in Figure 38. As the resonator size increases, there is an opportunity for more resonances to exist around the target frequency. The device with a ~4λ length can have lower motional impedance than a design with a ~2λ length, it also has a higher risk for spurious modes as seen in Figure 38. Without mode isolation circuitry, this spurious mode could affect the oscillator's stability.

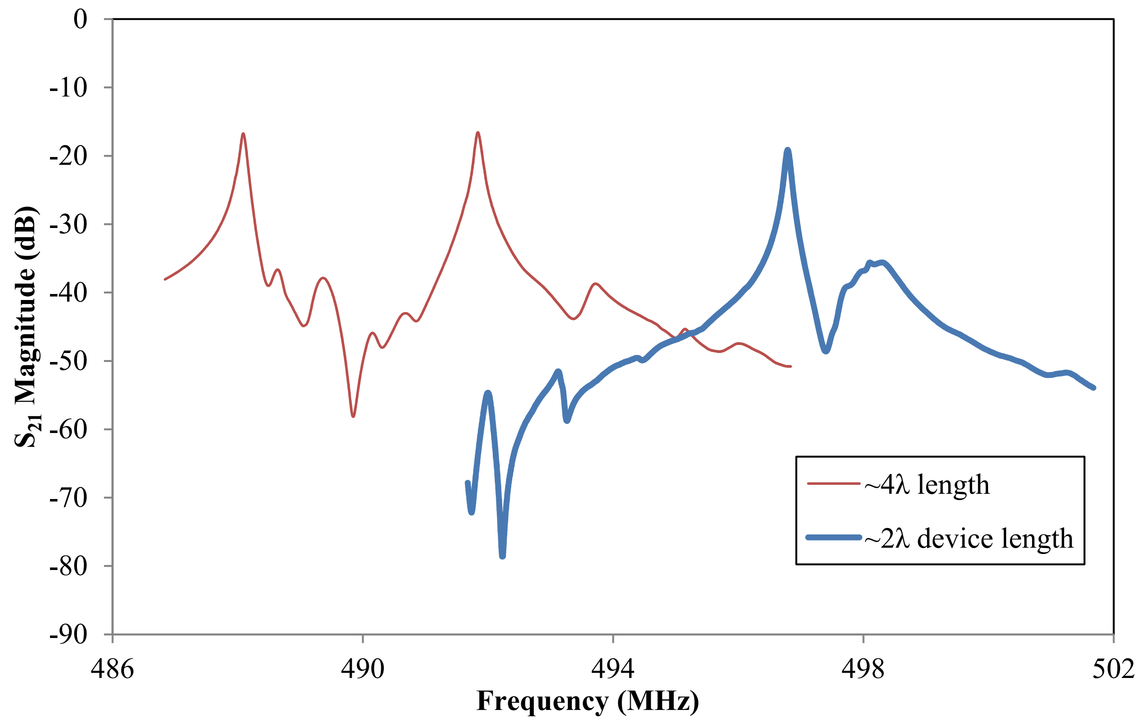

Figure 38. Measured frequency responses S_{21} magnitude for higher harmonic order resonators. Larger resonators (higher harmonic mode) have a propensity for strengthen spurious modes.

The tether lengths were designed at 9µm (λ/8 wavelength), 18µm (λ/4), and 27µm (3λ/8). If the substrate were an ideal infinite impedance, the 18µm (λ/4) tether would show the best performance. However, as seen in figure 39, the best performance for simulated and fabricated resonators was found for a tether length of 9µm (λ/8). This trend is in agreement with the 3-D COMSOL simulation seen in figure 39. Since the simulation does not contain all potential loss mechanisms, the simulated Q is higher than that of the measured devices.

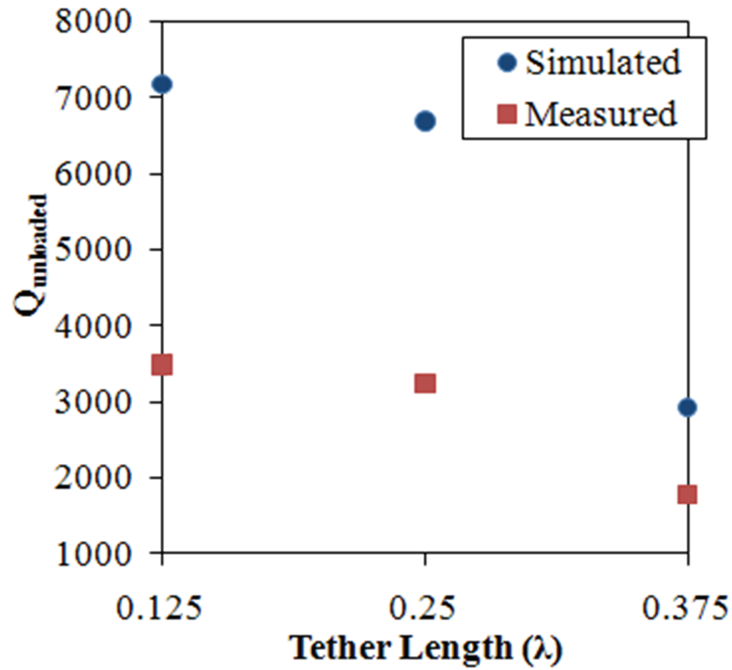

Figure 39. $Q_{unloaded}$ for simulated and fabricated 110MHz resonators with no acoustic reflectors. Please note that the simulated data shown here is a subset of the data in figure 8.

5.4.2. Designs with acoustic reflector. The reflector distance to tether was iterated by quarter-wavelength along with the previous eighth-wavelength iteration for the tether resulting in nine unique resonators. Twenty-one operating resonators of each design were measured to examine the efficacy of the proposed acoustic resonators. Two high quality factor frequency responses, one from a resonator without acoustic reflectors and one from a resonator with acoustic reflectors, are shown in figure 40. The measured characteristics for the average quality factors for each unique design are seen in table 2.

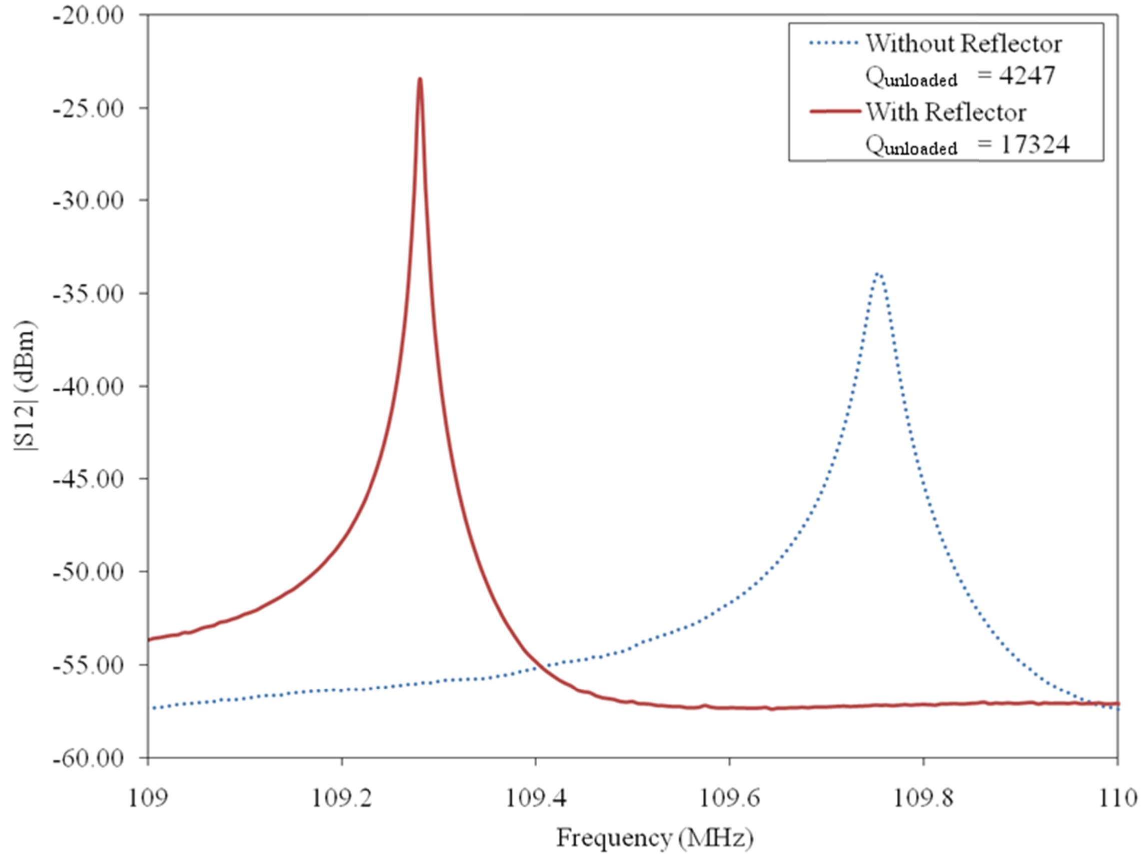

Figure 40. The measured frequency responses of the 110MHz resonators exhibiting the highest measured Q (with and without reflector).

Table 3. Average measured unloaded quality factors for 110MHz resonators.

Tether length (μm)	No acoustic reflector	Reflector distance to tether (μm) [a] 18 (λ/4)	36 (λ/2)	54 (3λ/4)
9 (λ/8)	3492	1475	15531	4676
18 (λ/4)	3247	5023	3788	4613
27 (3λ/8)	1818	3326	12042	1969

[a] Lengths expressed in acoustic wavelength are given in parentheses.

For each tether length there was at least one reflector design that improved performance, with the greatest performance enhancement of 562% seen for the tether length of 27μm (3λ/8) where the average $Q_{unloaded}$ for the basic design is 1818 but increases to 12042 with the addition of reflectors positioned at 36μm (λ/2) from the tether. Also, the addition of the acoustic reflector only

increased the covariation in the quality factor by 21%, meaning that even while the quality factor improved significantly, this improvement did not vary greatly. In figure 41, a plot of the measured resonators with tether length of 9µm (λ/8) are plotted on a wafer diagram and the consistent increase for all dies when a reflector is added at 36µm (λ/2) is shown. Table 3 shows the statistical data for the 27µm (3λ/8) tether length, which showed the greatest improvement with a reflector positioned 36µm (λ/2) wavelengths away from the resonator.

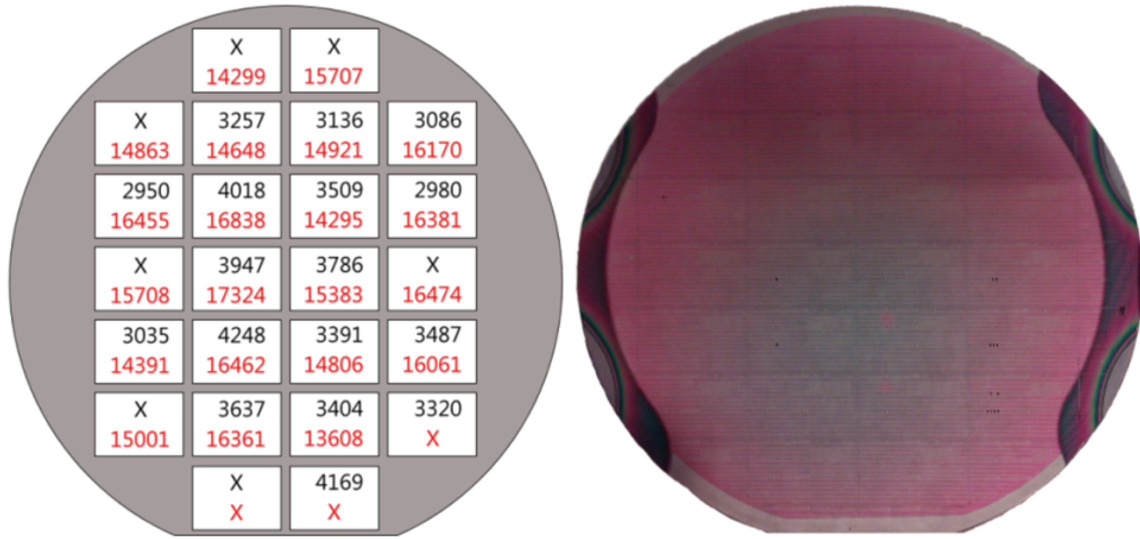

Figure 41. Cross-wafer $Q_{unloaded}$ measurements for 110MHz resonators with tether length of 9µm (λ/8) without (black) and with reflectors (red) at 36µm (λ/2). X denotes device locations that were non-functioning for this design.

Table 4. $Q_{unloaded}$ results for third harmonic 110MHz, lateral-extensional, TPoS resonators with tether length of 3λ/8.

Device	Top Performance		Average		Coefficient of variation	
Base 110MHz (no reflector)	2215		1818		0.145	
With Reflector @ λ/4	4815	(117%)[a]	3326	(83%)[a]	0.207	(43%)[a]
With Reflector @ λ/2	16204	(632%)[a]	12042	(562%)[a]	0.175	(21%)[a]
With Reflector @ 3λ/4	2314	(4.5%)[a]	1969	(8.3%)[a]	0.119	(-18%)[a]

[a] Increase as compared to base resonator

Shown in figure 42, the experimental data is compared with the coupled-field simulation. Dashed lines signify simulation results while solid lines denote measurements. Similar color lines and marker types are to be compared to each other. The simulated data follows the measured data's trend quite well. The limited number of loss mechanisms that were modeled could explain the optimistic quality factor estimated by the simulation. In addition, the trend inversion in the 18μm (λ/4) data as compared to the other anchor lengths shows the predicted quarter wavelength impedance transformation.

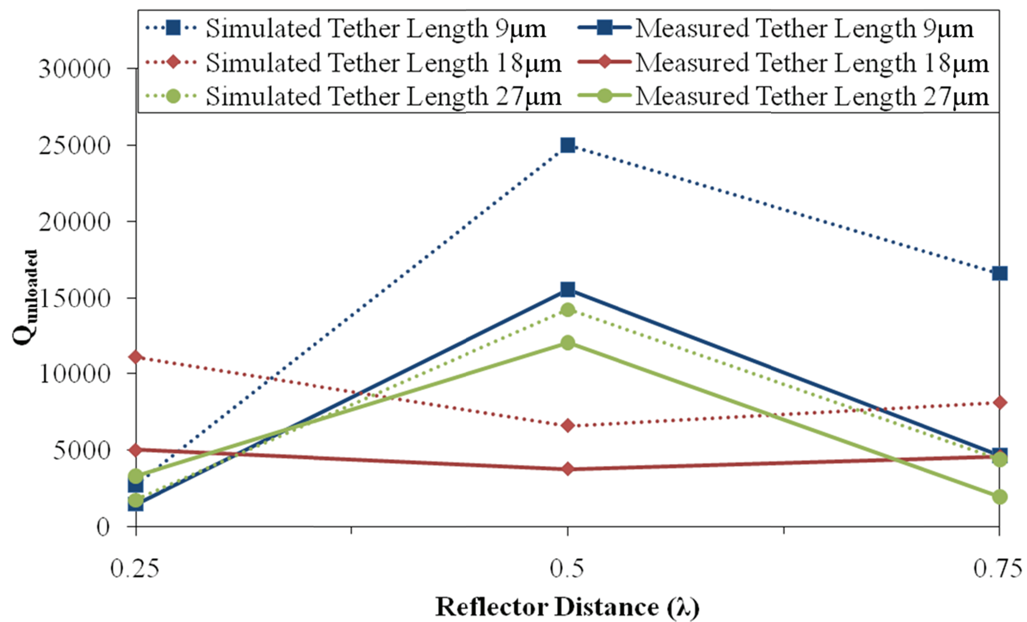

Figure 42. Measured and simulated Qunloaded from third harmonic 110MHz, lateral-extensional, TPoS resonators with acoustic reflectors.

Viscous and squeeze film damping in thin-film piezoelectric-on-silicon resonators with in-plane acoustic reflectors

To measure the magnitude of damping from the result of atmospheric conditions, high quality factor resonators were placed in the vacuum probe station pictured in Figure 7. The resonators' frequency response was recorded while at atmospheric pressure and again when the chamber was

evacuated down to 10mTorr. The two resulting responses are seen in Figure 43 and Figure 44 respectively. The quality factor improvement from atmospheric pressure (13183) to vacuum (16116) was ~22%. The slight increase is attributed to a lower air-resonator interaction under vacuum. In comparison, for capacitive resonators, the effect can be orders of magnitude [45].

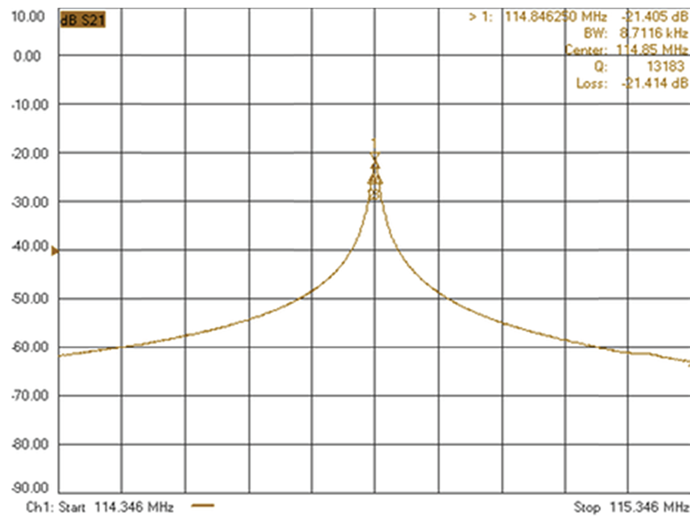

Figure 43. Screen capture of a high $Q_{unloaded}$ device as measured in atmosphere.

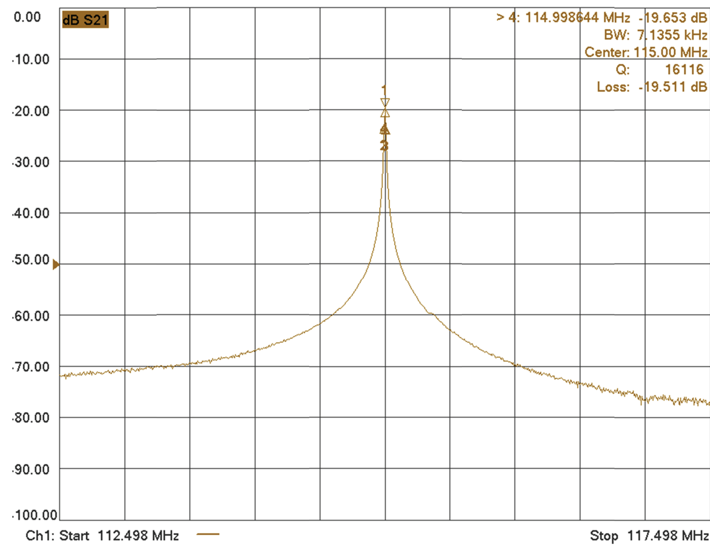

Figure 44. Screen capture of a high $Q_{unloaded}$ as measured under vacuum.

CHAPTER VII

MULTIPLE TETHER PAIRS

To examine the spurious modes in the high frequency TPoS resonators, a coupled-domain simulation was developed in COMSOL Multiphysics. The device was composed of single crystal silicon rotated to the <110> direction below an aluminum nitride piezoelectric layer. Metal electrodes, existent only in the simulated electrical domain, were placed above the aluminum nitride layer to provide the electrical interconnect for the piezoelectric. The device is connected to the silicon substrate by pairs of anchors. To analyze the suppression of spurious modes, simulations with one pair and two pairs of anchors were computed. Extending the device past two was significantly difficult since the acoustic wavelength, and thereby the simulated feature size, was small. Figure 45 shows the result of the simulation. In the blue frequency response, multiple resonances can be seen around the target frequency. These spurious modes could be incorrectly locked-in by the oscillator circuit, resulting in an improper oscillation frequency. With the addition pair of tethers, the magnitude of the spurious modes is suppressed, decreasing the likelihood that the device will lock-in to an incorrect mode.

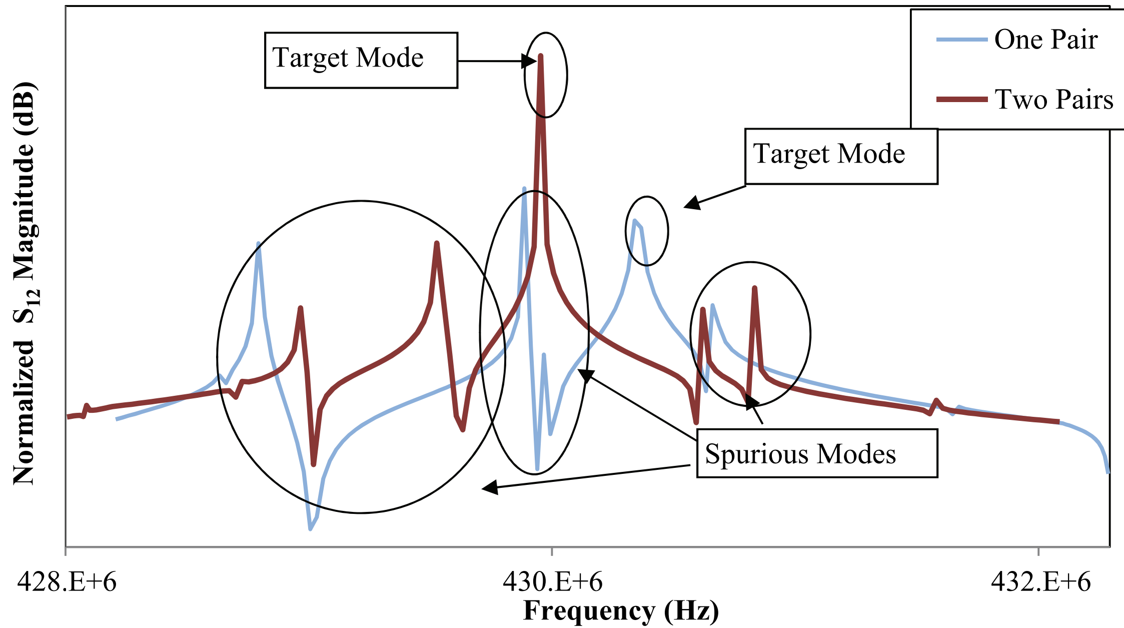

Figure 45. Simulated frequency response for 400 MHz designs over a 4 MHz span with different number of tether pairs.

The approach taken to reduce the spurious modes is to add additional tethers at nodes along the device length (Figure 46). The additional tethers serve to further constrain the resonator's motion and ultimately reduce the number and strength of the nearby spurious modes.

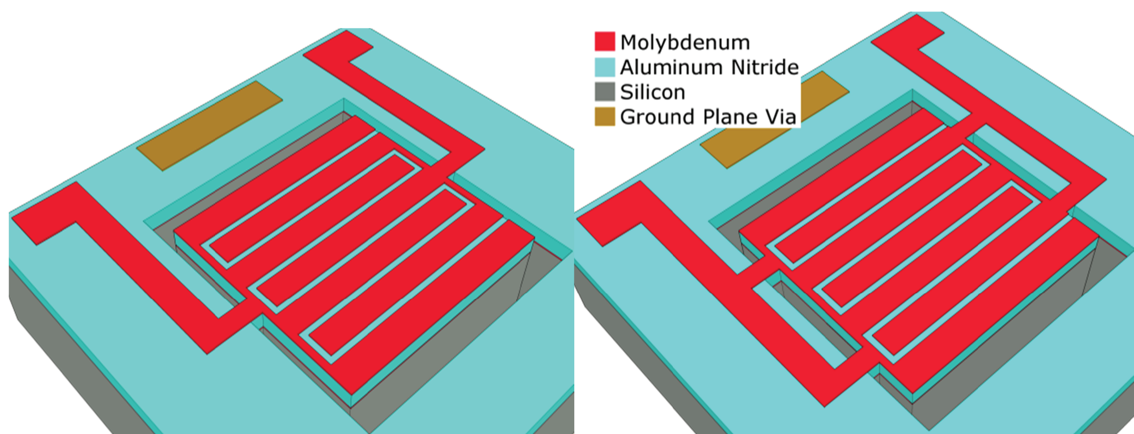

Figure 46. TPoS resonators with one pair (left) and two pair (right) of tethers.

Devices operating around 400MHz with a 7th harmonic order were designed with one and two pairs of tethers and significantly long (>5λ) lengths. Two frequency responses are shown in Figure 47 where the one pair of tether designs exhibits larger spurious modes as well as reduced performance.

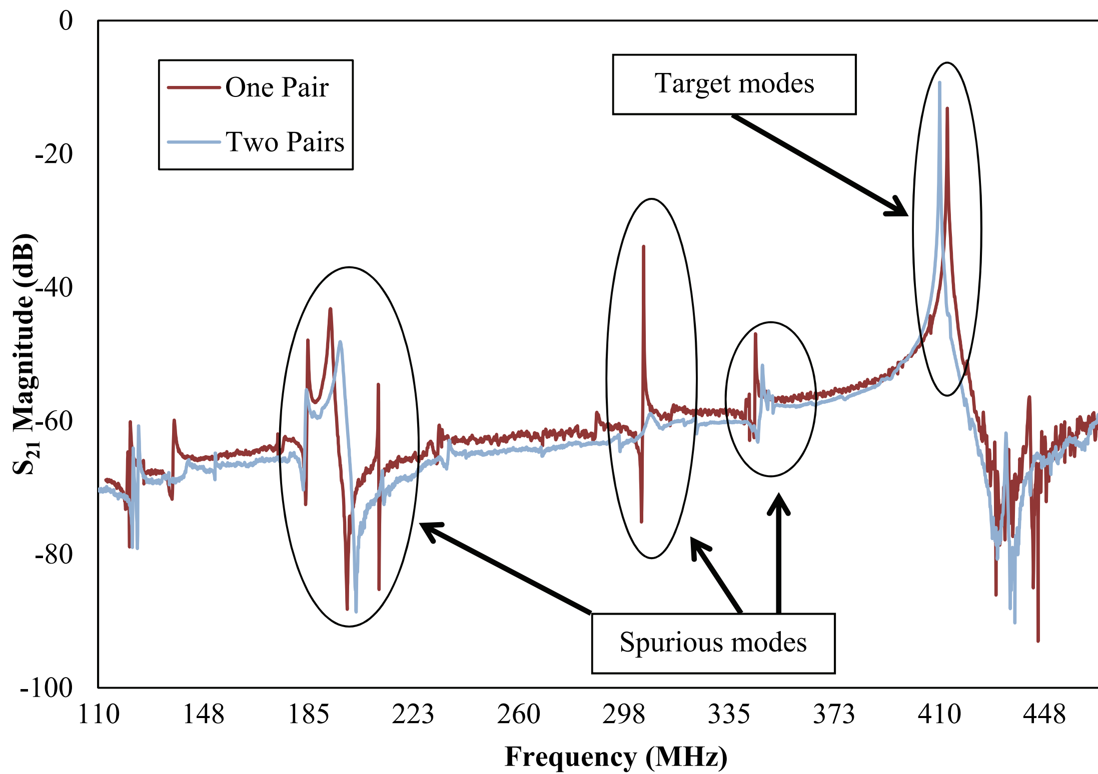

Figure 47. Large span frequency responses for 400MHz resonators with one and two pairs of tethers.

Upon closer inspection of the target mode, near resonance distortion can be seen on the one pair of tethers. Since the resonant body is greater than a wavelength in the length direction, there is the possibility for a degenerate mode close to the target mode. With two pairs of tethers, the distortion is no longer present, showing the suppression of this degenerate mode (Figure 48). In addition the performance of the resonator has improved. The motional impedance has decreased by 46% while the $Q_{unloaded}$ has increased by 57%.

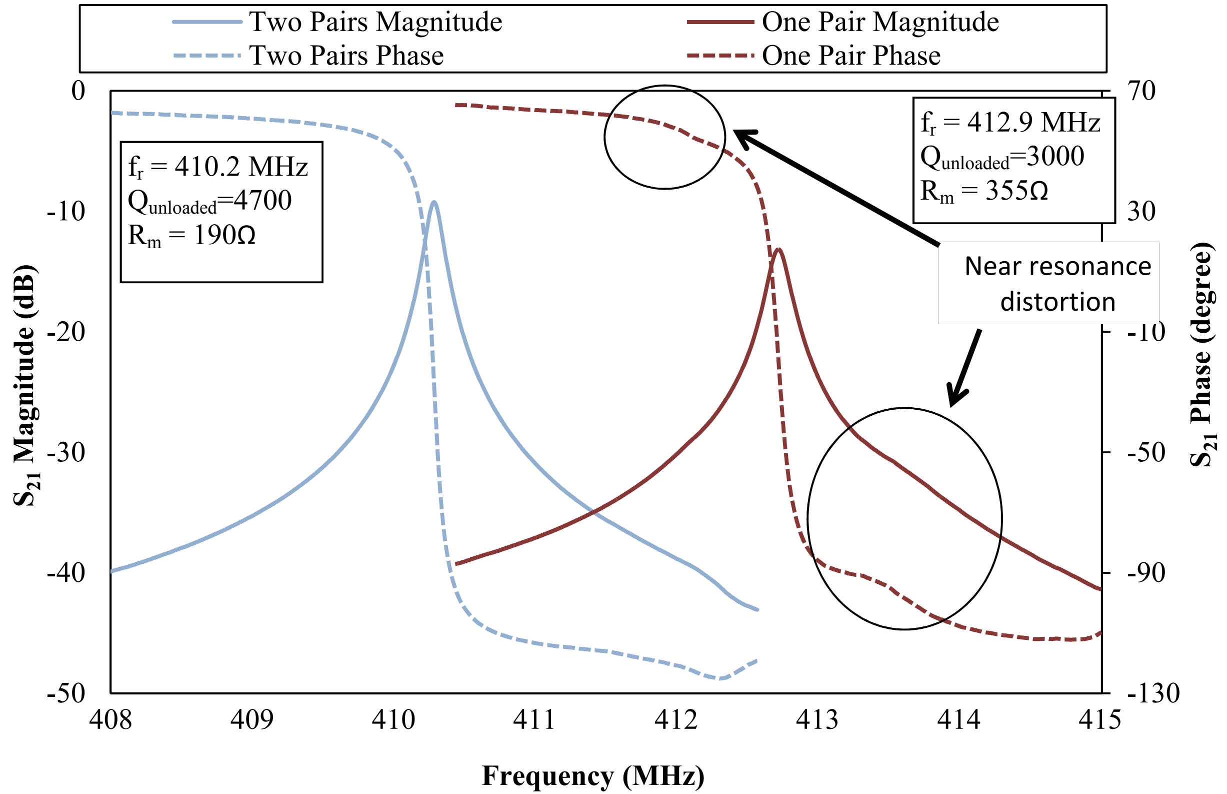

Figure 48. Measured frequency responses (magnitude and phase) of ~410MHz resonators with one and two pairs of tethers.

To analyze the effect on a larger scale, a set of 500MHz resonators were fabricated with various numbers of tether pairs. Over fifteen of each device was tested using a calibrated industrial-level semi-automated probe tester. The average $Q_{unloaded}$ for the devices is plotted in Figure 49. While on average adding tether pairs can have a detrimental effect on the performance, as more tethers are added, the performance soon overcomes the device with one tether pair and results in a 37% performance increase on average.

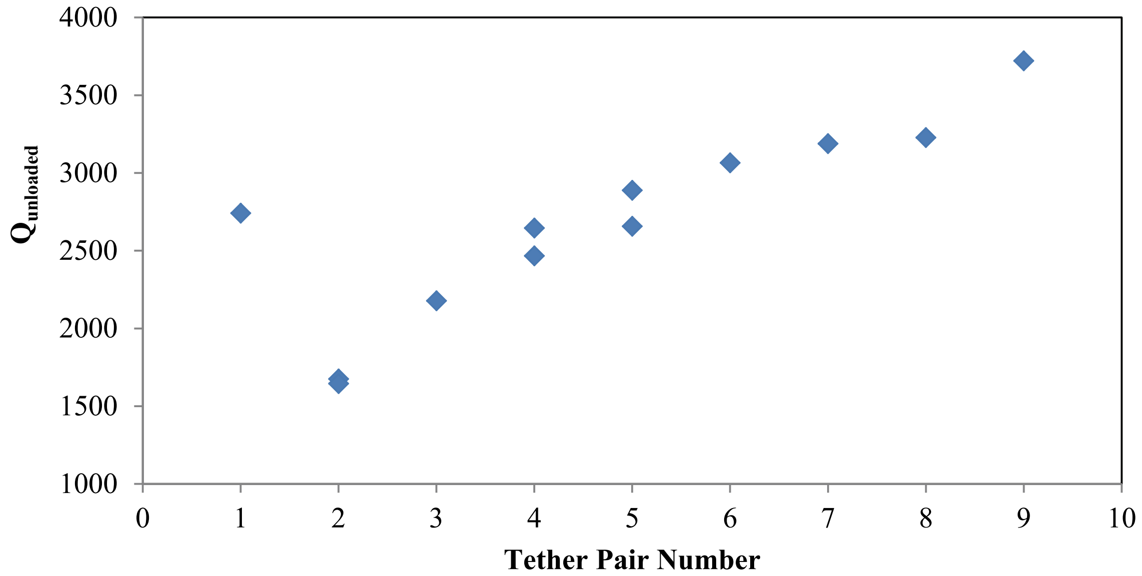

Figure 49. Average $Q_{unloaded}$ for increasing number of tether pairs on 500MHz resonators.

This effect was then extended to 21st harmonic, 1GHz TPoS resonators. Both resonators had significant device lengths (>9λ) and therefore can possess a significant number of spurious modes near the target frequency. Figure 50 shows frequency responses for two resonators, one with one pair of support tethers, the other with 9 pairs of support tethers. Near resonance distortion has been nullified in both the magnitude and phase frequency responses. With only a single pair of tethers, the $Q_{unloaded}$ is 4100 and the R_m is 346Ω. When the additional tether pairs are added to the design (nine tether pairs in total), the $Q_{unloaded}$ is increased to 6700 (63% increase) and the R_m is 162Ω (53% decrease). The result is the largest reported f Q product figure of merit (7.1e12) piezoelectric-transduced resonator at 1GHz [65], [66].

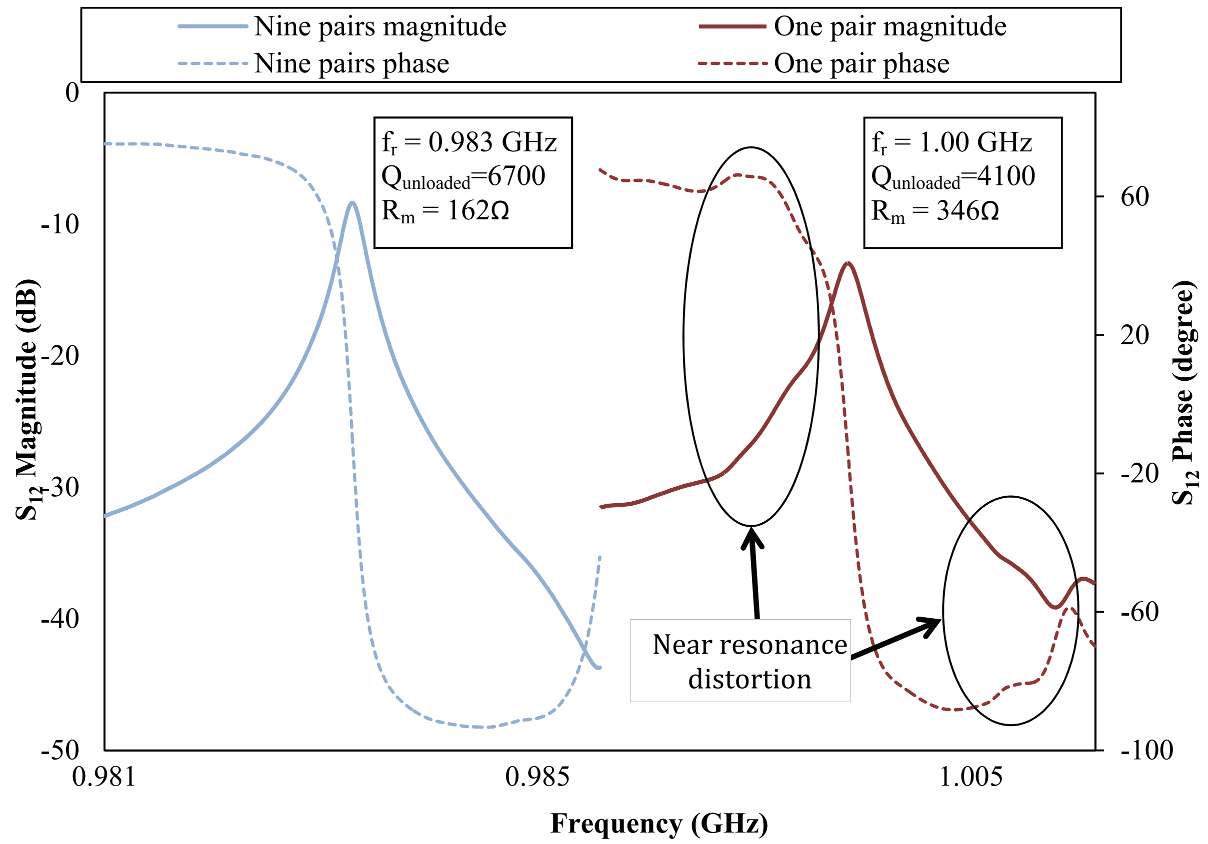

Figure 50. Frequency responses for ~1GHz resonators with one and nine pairs of tethers.

Frequency stability of multi-tether devices.

The frequency stability for these designs was also analyzed. In a timing application, the stability of the oscillator is critical. Having a low frequency shift in response to the environment is desirable. To analyze the temperature coefficient of frequency (TCF), the resonator is mounted on a temperature-controlled chuck in a vacuum probe station. The chamber's atmosphere is removed and the resonator's temperature is adjusted via a proportional-integration-derivative (PID) controller. As the temperature is changed, the resonance frequency is logged (Figure 51). The resonator's frequency shift shows a very linear, -29ppm/°C, shift that is characteristic of a lateral-extensional single crystal silicon resonator [17]. The shift is relatively large in comparison to quartz-based resonators but significant improvements have been made in both active [67], [68] and passive [69] temperature compensation methods for silicon resonators.

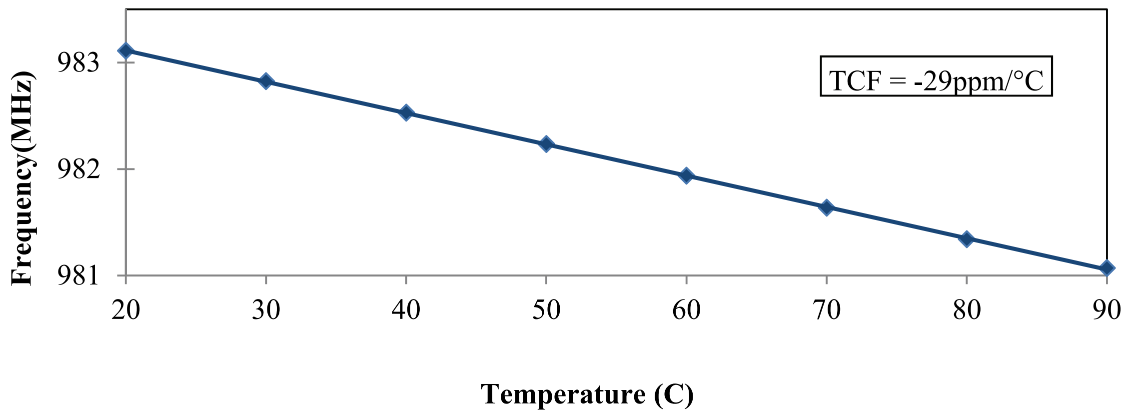

Figure 51. Temperature response for the ~1GHz TPoS resonator with nine support tethers.

CHAPTER VIII

POWER HANDLING OF MULTIPLE TETHER PAIRS

Phase noise is a critical measure of the frequency stability in oscillators. Phase noise is defined as the half the one-sided power spectral density of the phase deviation [70]. In a more physical sense, phase noise represents all random phase fluctuations of the output waveform due to all noise sources. Leeson's model predicts the phase noise-to-carrier ratio in an ideal oscillator as [71]:

$$L(\Delta\omega) = 10log\left[\frac{2k_bT}{E_{Stored}}\frac{Q}{\omega_0}\left(1+\left(\frac{\omega_0}{2Q\Delta\omega}\right)^2\right)\right] \quad (26)$$

where ω_0 is the carrier frequency, $\Delta\omega$ is the offset, Q is quality factor, E_{Stored} is energy stored in the resonator, k_b is Boltzmann constant, and T is equivalent noise temperature. As seen in (2), quality factor and the energy stored in the resonator affect the phase noise. Near-carrier noise is lessened as the stored energy decreases or the quality factor increases. However, noise floor (first term in the brackets) rises when the stored energy is decreased or quality factor is increased. Therefore, presuming all other parameters remain unchanged, a larger Q raises the noise floor.

In lateral-extensional TPoS resonators, the spring constant can be expanded into a nonlinear spring constant $k_e(x) = k_0(1 + k_1x + k_2x^2 + \cdots)$ where k_1 and k_2 are the first and second order anharmonic terms and x is the vibration amplitude. On the other hand, the energy stored in the device reaches its maximum when the device is pushed to hysteresis:

$$E_{stored}^{max} = \frac{1}{2}kX_c^2 \tag{27}$$

where k is the mechanical spring stiffness and X_c is the maximum (critical) vibration amplitude at the edge of hysteresis [72]. Therefore maximum energy stored in the device is proportional to the stiffness constant and square of the maximum vibration amplitude, X_c. In lateral-extensional fundamental mode devices, k and X_c are proportional to thickness, length, width, and quality factor as:

$$\mathrm{k_e} \sim \frac{\mathrm{t \cdot l}}{\mathrm{w}} \quad \text{and} \quad \mathrm{X_c} \sim \frac{\mathrm{w}}{\sqrt{\mathrm{Q}}} \tag{28}$$

$$E_{stored}^{max} \sim \frac{t \cdot l \cdot w}{Q} \tag{29}$$

As illustrated above, maximum energy stored in the device is inversely proportional to the quality factor. In summary, power delivered to the device at X_c determines the maximum energy stored in the device and consequently the phase noise.

The power handling capabilities of resonators were examined. As the device area increases, the resonator is able to handling a greater level of power dissipated in it, since its energy capacity increases. However, as quality factor increases the ability, the amount of energy stored in relation to the amount of energy lost is increased. This increase results in a greater propensity to nonlinearity.

To demonstrate the power handling capabilities of TPoS resonators, a resonator is analyzed at multiple input power levels. As the power increases, the resonant peak will begin to shift. Figure

52 shows a typical spring softening effect. As the input power level is increased, the resonance peak shifts to the level as if the effective spring constant has been lessened (blue and red) from the original resonance shape (in green). Sweeping the frequency in the reverse direction (from high to low) in frequency exhibits a nonlinear, hysteresis from the typical forward direction (from low to high). The point at which this hysteresis occurs is called the bifurcation point and will serve as the point at which the devices move into the nonlinear regime.

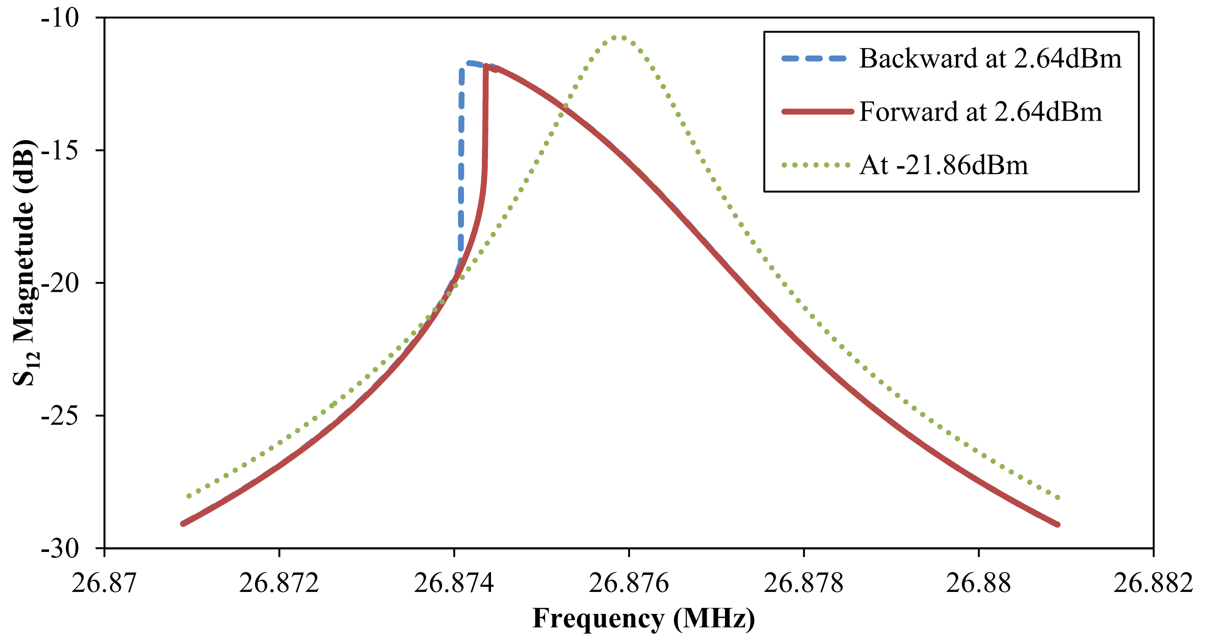

Figure 52. A 27MHz TPoS resonator under varying input power levels.

To quantify the frequency response peak shift, a metric, D_n, is define in Equation (13) to measure the amount of shift relative to the center frequency (f_c). In the case that the peak is symmetric, D_n will be zero.

$$D_n = \frac{f_c - f_p}{f_c} \tag{30}$$

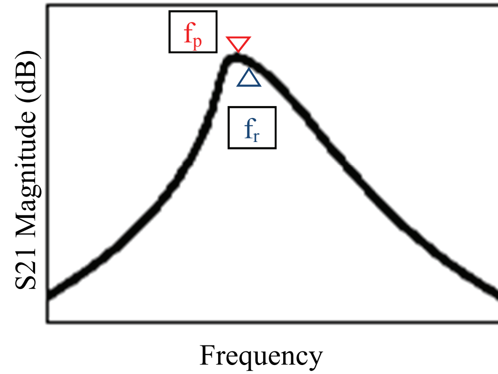

Figure 53. A model of a asymmetric resonance peak from a frequency response. Location of the peak (f_p) and the center (f_r) are noted.

Under this condition, a device that can handle larger power is will have a lower D_n at a given power dissipation than a device with a smaller power handling capability. Caution must be made such that the power delivered to the DUT is normalized in order to make these comparisons.

$$P_{delivered} = 10\log_{10}\left[R_m\left(\frac{V_{in}}{R_m+R_s+R_L}\right)^2\right]\text{(dBm)} \tag{31}$$

Resonators of different dimensions where analyzed to determine the power handling capabilities. The power delivered to the resonator was adjusted and the peak shift was noted. If devices have similar quality factors, devices with larger power handling capability will shift less as the power delivered is increased. Since there is noise in the test configuration, multiple devices were analyzed to find the general trend.

For devices with where the device length was increased from 237µm to 240µm, there was no significant change in the power handling capability (Figure 54) most likely attributed to the small increase in volume. When the volume is increase significantly, in the case of Figure 55 by increase harmonic order, the resonators show an increase in power handling capability.

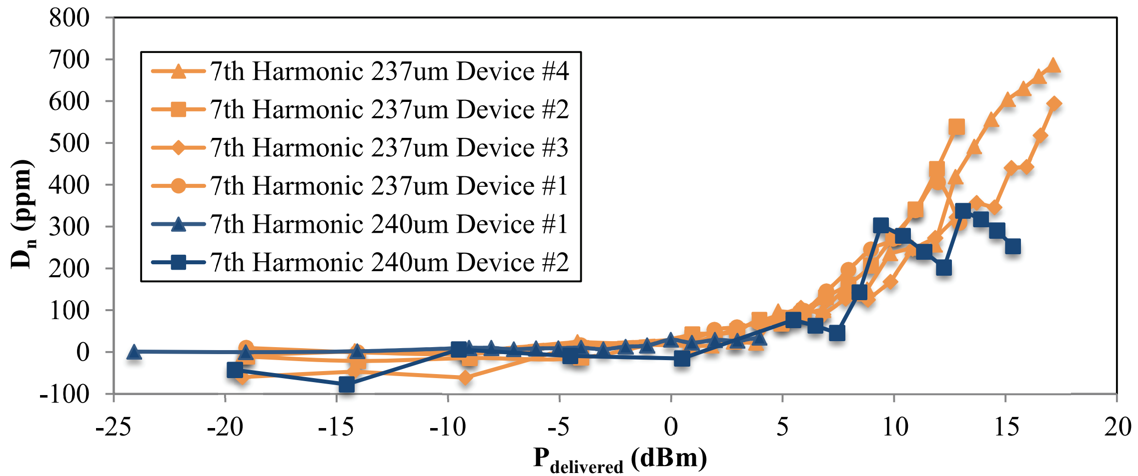

Figure 54. As expected with theory, altering the length does not have a strong dependence on power handling capability.

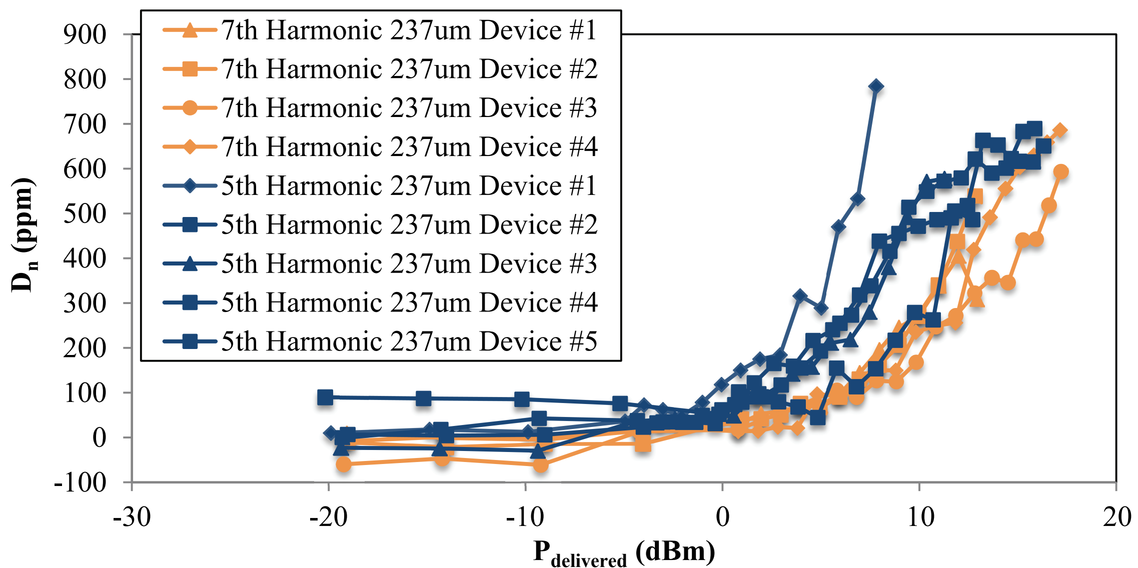

Figure 55. Increasing harmonic order shows a distinct improvement in power handling capability.

Alternatively, when additional tether pairs are added to the structure, the resonator's quality factor and power handling capability are improved Figure 56.

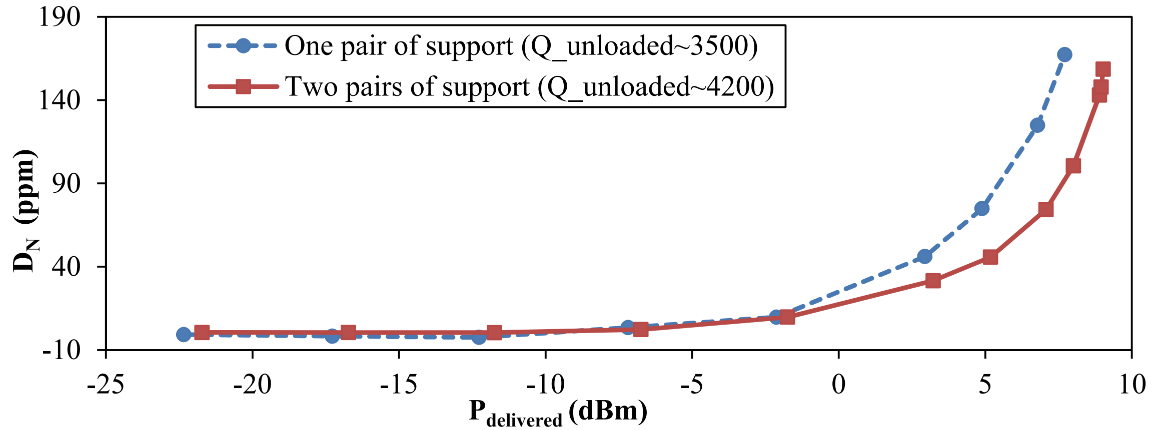

Figure 56. Increasing tether number provides an avenue to increase both the quality factor and power handling capabilities.

A TPoS Resonator with only one tether pair exhibit lower power handling capability even though they have lower quality factors.

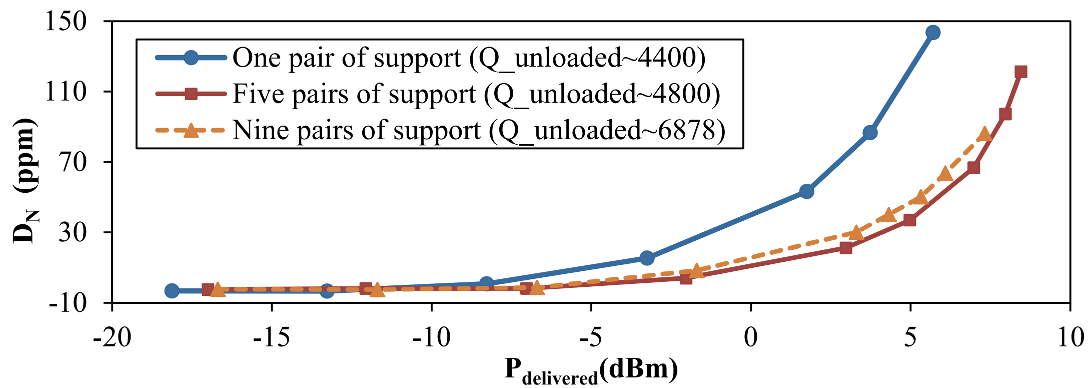

Figure 57. Power handling capability for 1GHz TPoS resonators with different number of tether pairs.

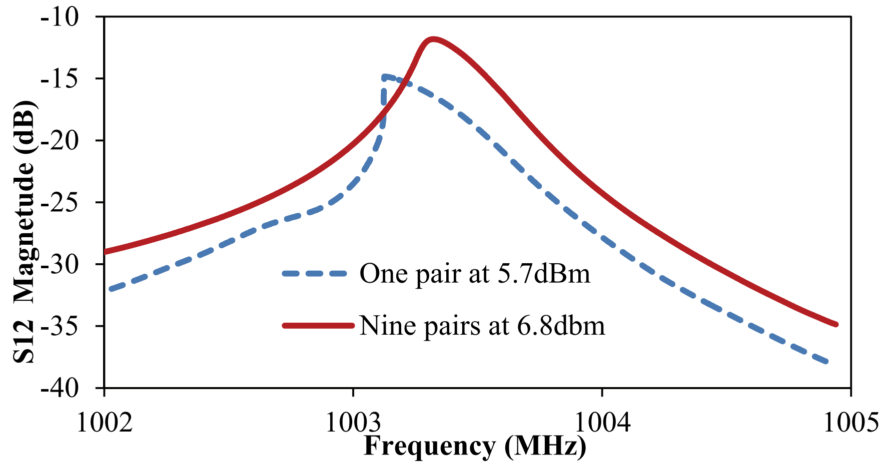

Figure 58. Frequency response for 1GHz resonators.

Gain compression in TPoS resonators

An alternative method to analyze nonlinearity in TPoS resonators is to use a metric traditional employed to measure nonlinearity in amplifiers, gain compression. The P_{-1dB} gain compression point in microwave amplifiers is a figure of merit defined the input power at which nominal gain has reduced by a 1dB (Figure 59).

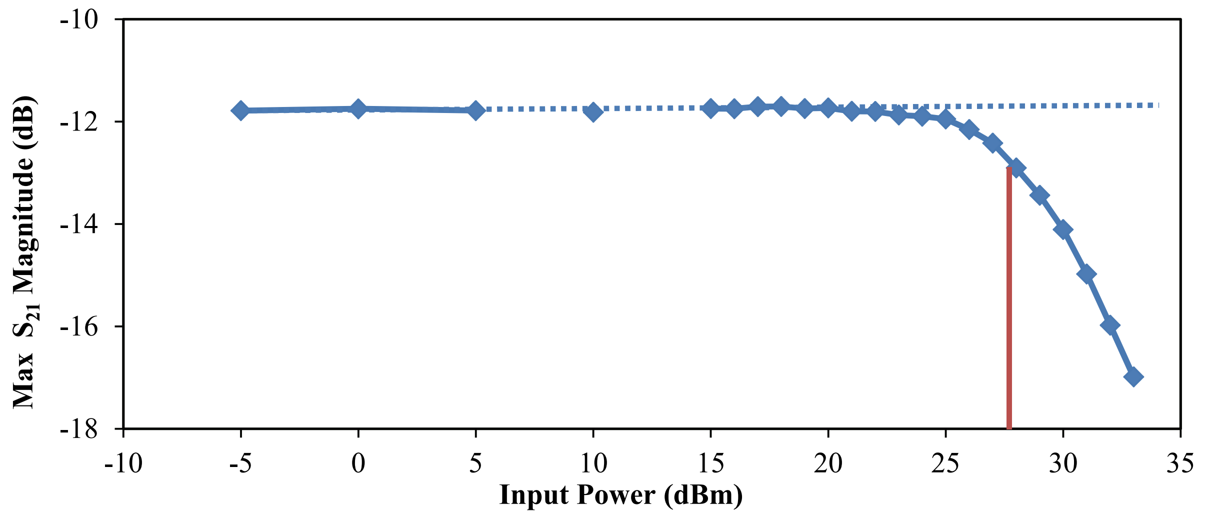

Figure 59. A typical power gain curve showing the 1dB (red) gain compression point at ~28dBm input power as the gain has been desensitized compared to the ideal (dotted blue).

To understand how gain nonlinearity affects the output signal on a system level, a large signal analysis can be done. First, the power gain at the fundamental frequency (22) can be written as the ratio of the output power to the input power at the fundamental frequency:

$$G_{\omega_0} = {P_{o,\omega_0}}/{P_{i,\omega_0}} \tag{32}$$

If the gain is linear, the ideal output signal takes a similar form as the input. However, if the gain is nonlinear, specifically polynomial, the output signal takes the form of a power series (23).

$$V_o = g_1 V_i + g_2 V_i^2 + g_3 V_i^3 + \cdots \tag{33}$$

If the square and cubic terms are expanded with a sinusoidal input, it can be seen that even terms produce a constant and even harmonics while odd terms affects the fundamental and produces higher odd harmonics.

$$V_i = a\cos(\omega t) \tag{34}$$

$$g_2 V_i^2 = g_2 a^2 \cos^2(\omega t) = g_2 a^2 \frac{1}{2}(1 + \cos(2\omega t)) \tag{35}$$

$$g_3 V_i^3 = g_3 a^3 \cos^3(\omega t) = g_3 a^3 \left(\frac{3}{4}\cos(\omega t) + \frac{1}{4}\cos(3\omega t)\right) \tag{36}$$

Since the even terms do not expand to include the fundamental mode, the even harmonics will not affect the apparent gain at the fundamental frequency. On the other hand, the odd terms contain the fundamental frequency, and therefore the odd terms will contribute to the fundamental frequency gain. The resultant gain at the fundamental frequency with the third term included from the nonlinear, polynomial gain is:

$$G_{\omega_0} = \frac{g_1 a + \frac{3}{4} g_3 a^3}{a} = g_1 * \left(1 + \frac{3}{4}\frac{g_3}{g_1} a^2\right) \tag{37}$$

For a positive g_3/g_1, the gain will expand with increasing input signal. In the converse, a negative g_3/g_1 will cause the gain to compress with a stronger input signal.

To test the gain compression in TPoS resonators, the devices were characterized with a manual probe station with a network analyzer. Since the maximum signal power from the network analyzer is not sufficient to drive the devices to nonlinearity, a RF amplifier with +25dB gain was placed in line. The input power on the network analyzer was adjusted and the gain at the resonance was captured. Fifth and seventh order devices with one pair of support tethers and three pairs of support tethers were measured. Figure 43 shows one such device under test, as the power increases from -5 to 10dBm. The device shows spring softening as described in the previous section and gain compression of -0.25dB. As the input power is swept the resulting curve can be seen in Figure 61.

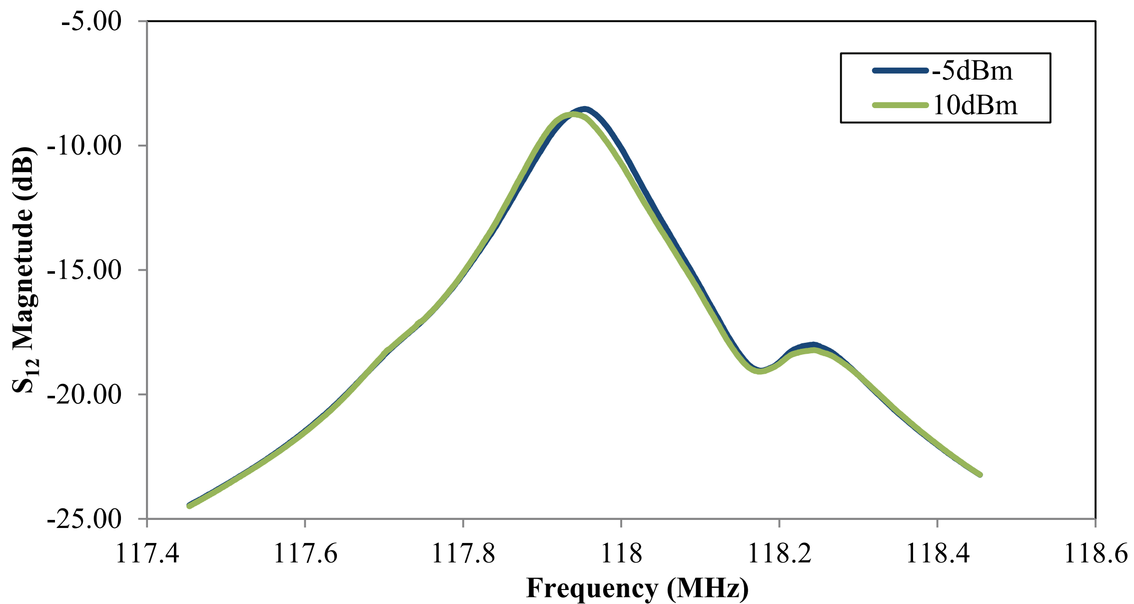

Figure 60. Frequency responses of a fifth order 118MHz TPoS resonator with one pair of supports. The blue curve shows the resonator with a -5dB input power. As the power increases to 10dB, the resonator's peak shifts lower and to the right as seen in green.

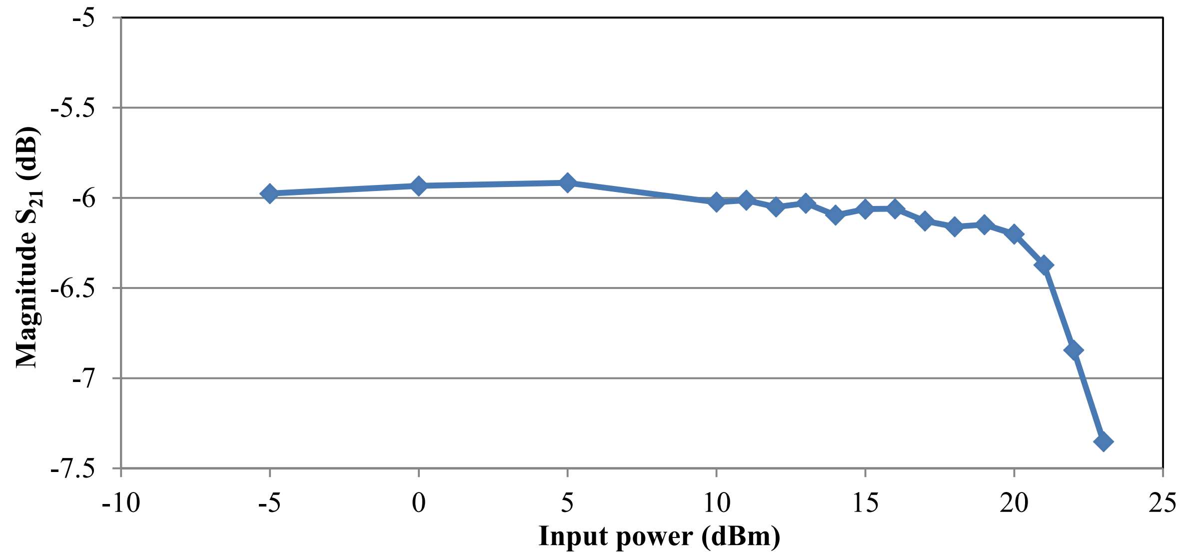

Figure 61. Gain curve for a fifth order 118MHz TPoS resonator with one pair of supports. The device shows definitive gain compression with a P_{-1dB} of ~22dBm

Interestingly, not all the devices exhibit an ever-decreasing curve as seen in Figure 61. For the seventh harmonic order devices with three tether pairs, the gain expands for a small period before it begins to compress.

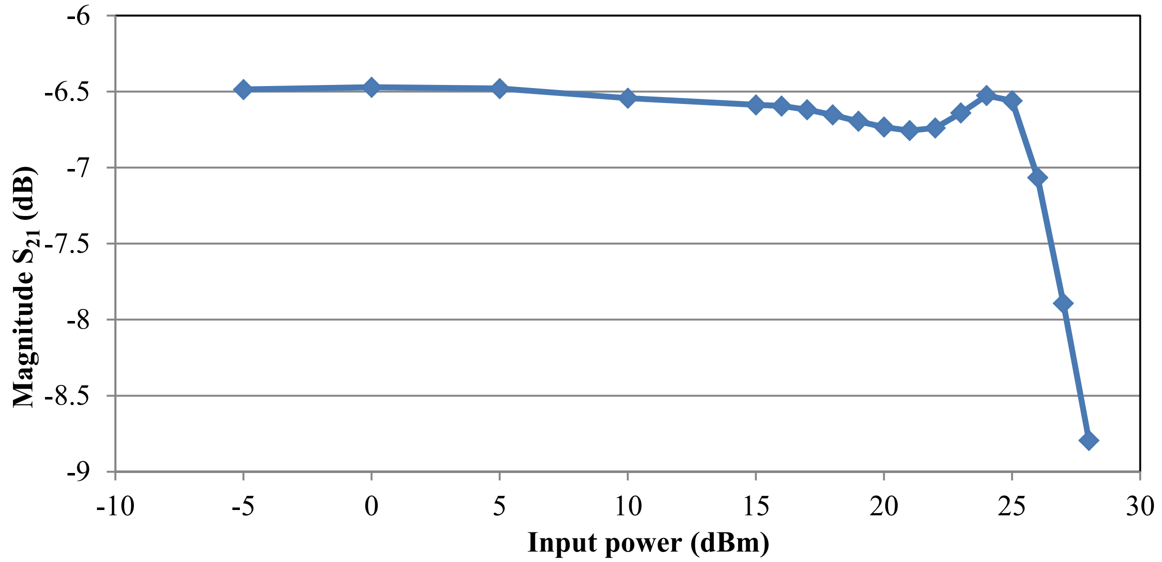

Figure 62. Typical gain curve for seventh harmonic 118MHz TPoS resonators with three pairs of tether pairs. The devices exhibit a period of gain expansion before rapid gain compression.

As with the previous nonlinearity analysis, devices with similar motional impedances should be compared. This ensures that similar power is being delivered to the device and thereby not biasing the results for devices with higher motional impedances. Figure 63 shows the clear effect of the resonator's motional impedance on its gain compression point. At lower motional impedance, less power is dissipated on the device. In addition, as the devices harmonic order increases from 5th to 7th mode, the point at which the gain compresses is distinctly enlarged. The additional tether pairs marginally improve power handling capabilities with respect to gain compression.

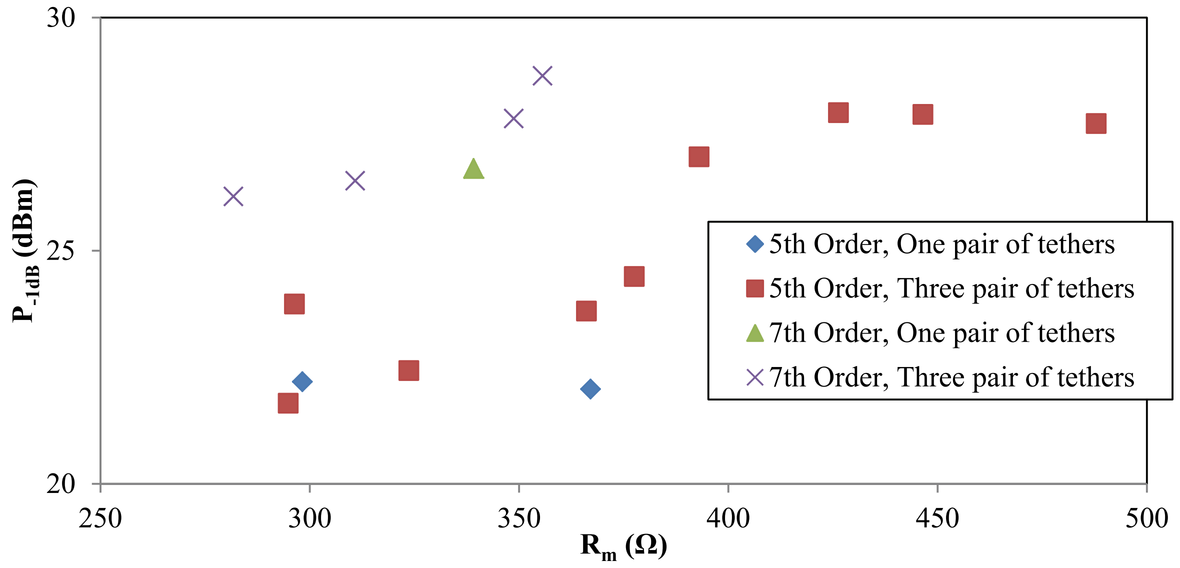

Figure 63.The P_{-1dB} gain compression points for 118MHz TPoS resonators.

CHAPTER IX

CONCLUSION

Thin-film piezoelectric-on-silicon lateral extensional mode resonators are poised to be a large contributor in the real-time clock application space for commercial use. This work describes two distinct approaches for improving the performance of lateral extensional mode, thin-film piezoelectric on silicon resonators, through use of multiple support tether pairs and through the addition of in-plane acoustic reflectors.

During this research, the highest f Q product figure of merit for piezoelectric resonators was produced using the multiple tether pair technique. Multiple tether pairs showed lower motional impedance and cleaner frequency responses with reduced number and magnitude of spurious modes near the target resonance frequency. In addition, quality factors and power handling can be simultaneously improved through the use of multiple support tether pairs. Two methods, frequency shift and gain compression, for comparing nonlinearity showed improvement in nonlinearity for the designs with multiple tether supports.

The thesis is also first reported application of perfectly matching layers to model in-plane acoustic anchor loss. The first in-plane acoustic reflectors for lateral-extensional resonators were

fabricated and characterized. The acoustic reflector measurements showed that the performance of the resonator could be harmed or enhanced by positioning the acoustic reflector at different points on the outgoing wave.

Future work

There is still much work to be done on in the research space though. A few topics are discussed below.

In-plane acoustic reflectors

The microacoustics space can leverage some of the research and work in the optics field to yield interesting results. The acoustic energy can then become a probing mechanism for many experiments that are acoustically sensitive. With the inclusion of in-plane acoustic reflectors, the resonator could become an acoustic source from which energy can be pulsed through a method called Q-switching. If the material in the reflectivity of the in-plane acoustic reflector could be tuned, the cavity can be charged and dumped upon an external signal resulting in a high-energy acoustic pulse.

Additional analysis can also be performed using dynamic white light interferometry. With this technique, the wave motion leaving the device can be seen and its energy quantified. With this insight other more novel structures can be designed reduce the anchor loss.

Gain compression

In the microwave amplifier field, gain compression is a widely known metric for comparing architectures. However, the gain compression is often not directly measured but instead the second and third harmonic intercepts are used to estimate where the gain compression point will lie. The field of nonlinearity in piezoelectric-on-silicon resonators is quite a fresh field and could leverage many topics from the amplifier design community to better understand the devices.

CHAPTER X

APPENDICES

A. Model SEM images of fabricated thin-film piezoelectric-on-silicon (TPoS) resonators.

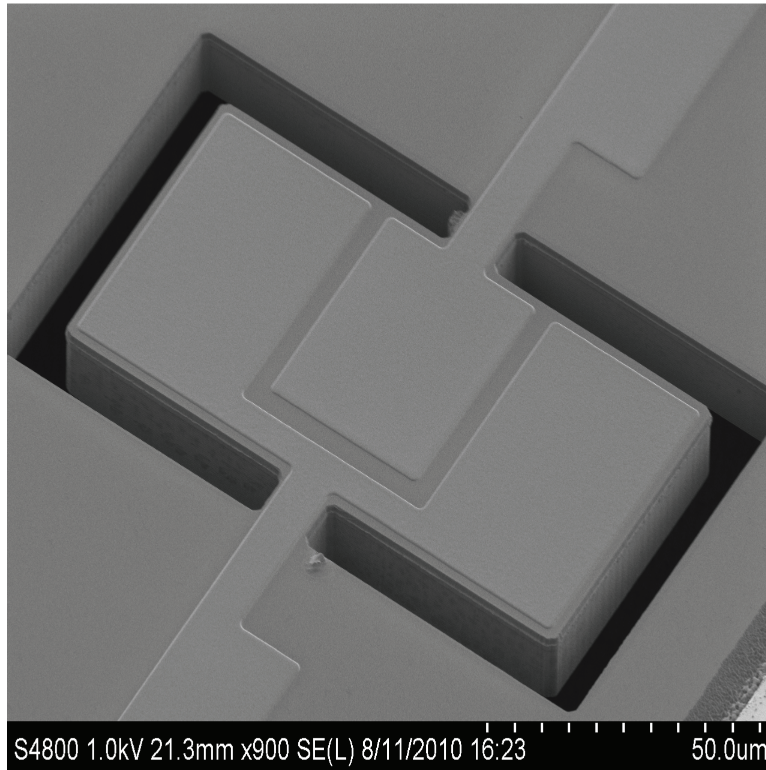

Figure 64. Third harmonic thin-film piezoelectric on silicon resonator with a target frequency of 120MHz.

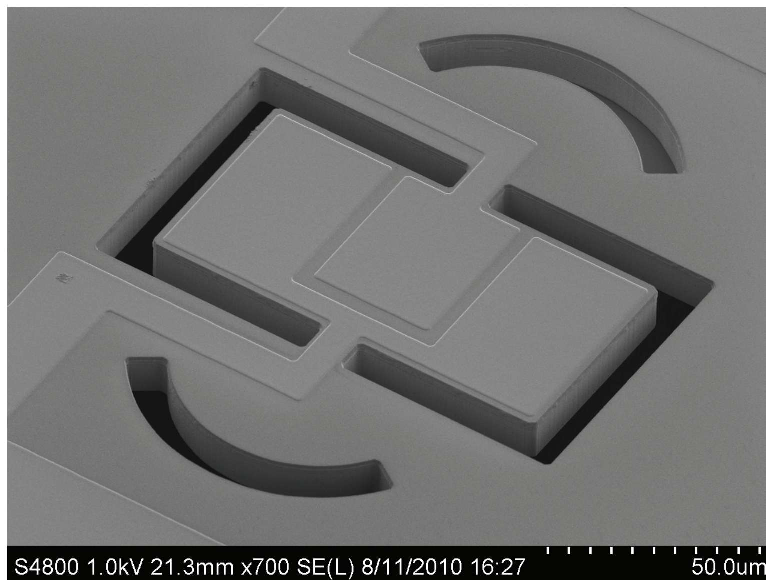

Figure 65. 120MHz, third order thin-film piezoelectric on silicon resonator with acoustic reflectors

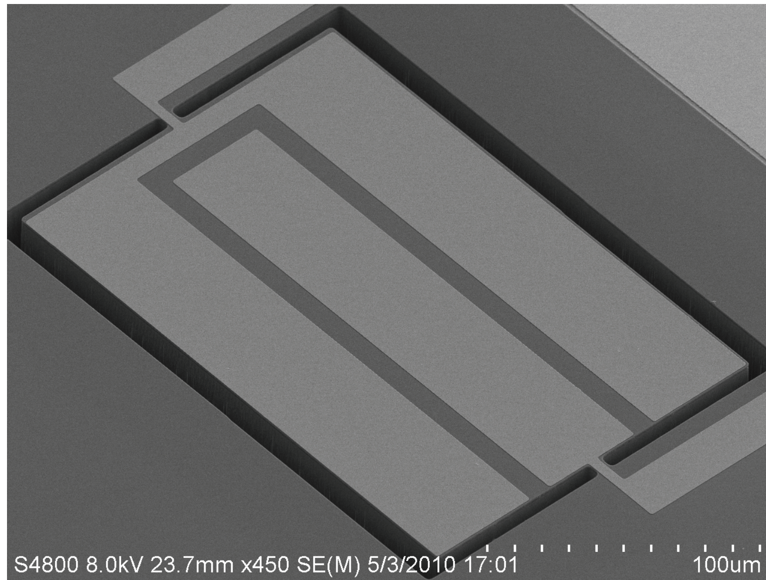

Figure 66. Fundamental order, 27MHz thin-film piezoelectric on silicon resonator.

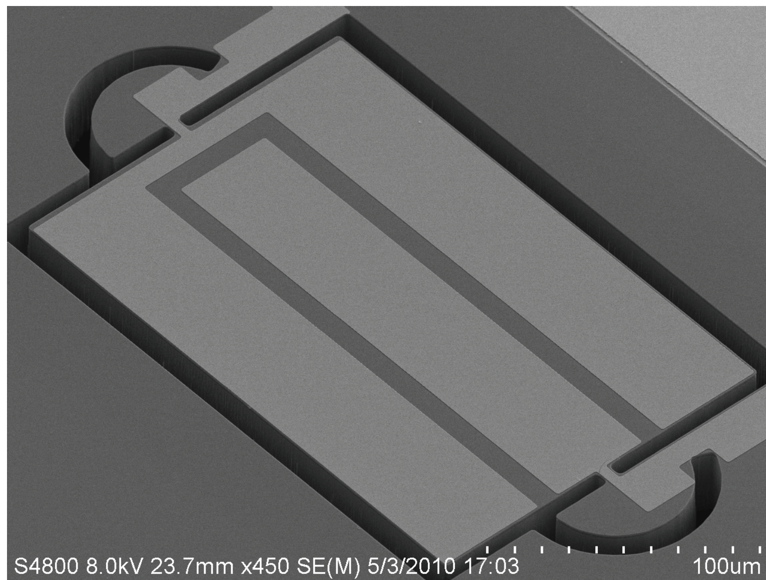

Figure 67.Fundamental order 27MHz thin-film piezoelectric on silicon resonator with acoustic reflectors positioned too close to the resonator.

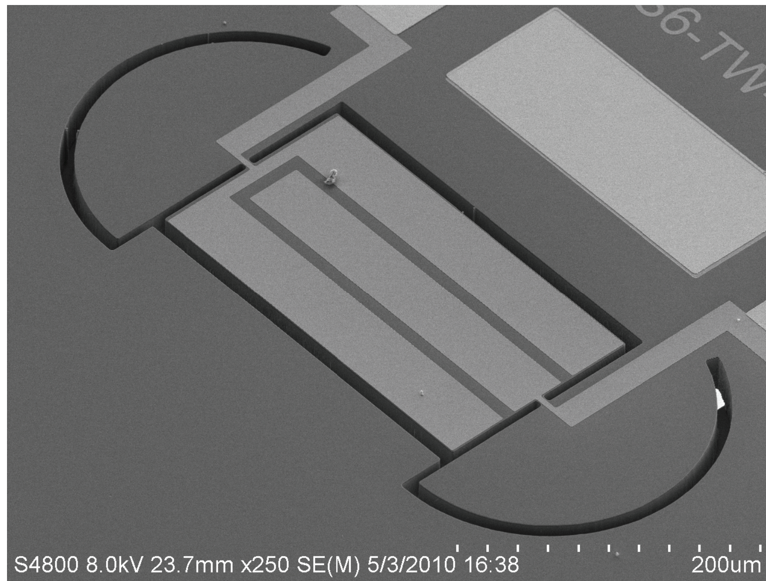

Figure 68. Fundamental mode 27MHz thin film piezoelectric on silicon resonator with acoustic reflectors at the near optimal position.

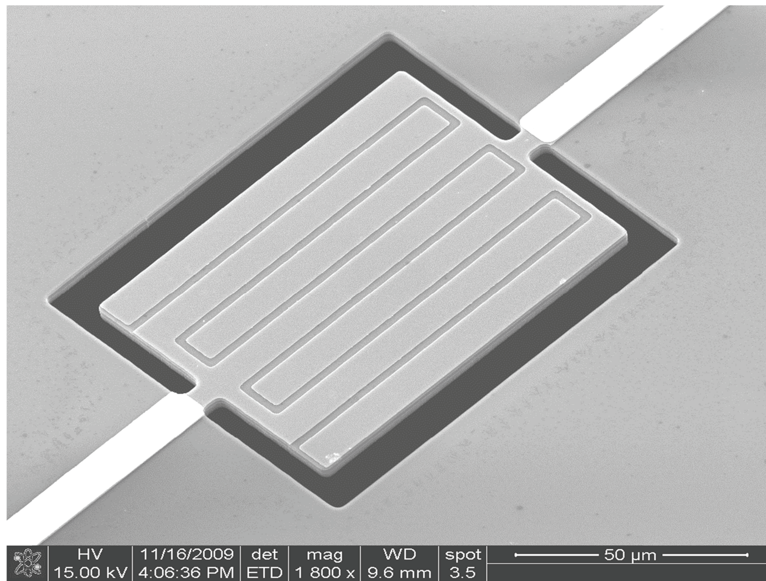

Figure 69.Seven harmonic, 470MHz thin film on piezoelectric on silicon resonator with one tether pair.

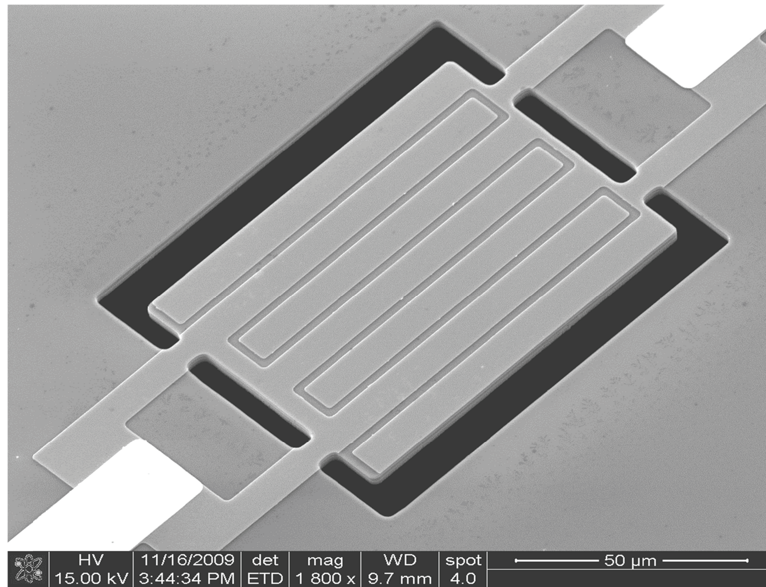

Figure 70. Seventh order thin film piezoelectric on silicon resonator with two tether pairs.

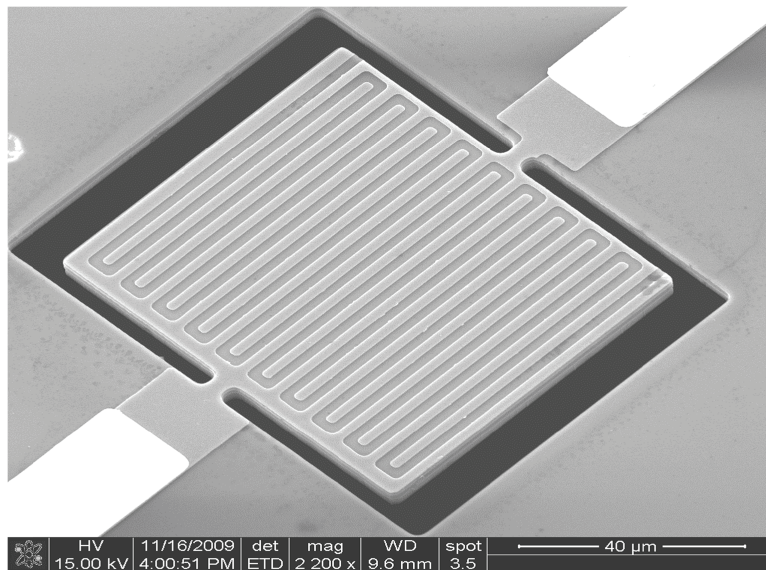

Figure 71. Twenty-first harmonic thin film on piezoelectric on silicon resonator targeting 1GHz with one tether pair.

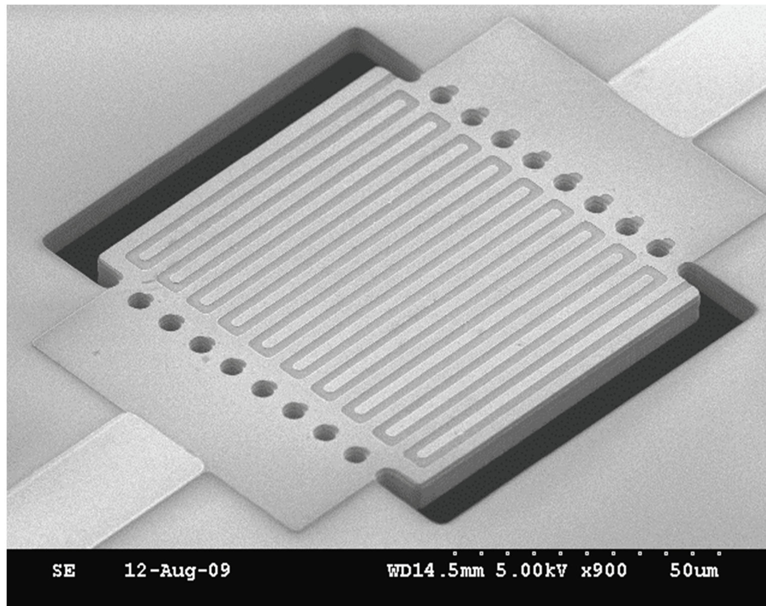

Figure 72. Twenty-first harmonic thin film piezoelectric on silicon resonator with nine tether pairs targeting 1GHz.

B. Power dissipated and gain compression Python code

```
# Imports
# Matlab like graphing capability
import matplotlib.pyplot as plt
#Floating point math operations
import math
#Complex number math operations
import cmath
#Folder and directory operations
import os
#Matrix operations
from scipy import linalg
#Matlab .mat file reader
from numpy import mat
#Excel writer
from pandas import DataFrame, ExcelWriter


#A class to mimic a s2p data file
#Magnitudes are in dB
#Phases are in degree
class s2p:
    def __init__(self):
        self.freq = []
        self.s11mag = []
        self.s11phase = []
        self.s21mag = []
        self.s21phase = []
        self.s12mag = []
        self.s12phase = []
        self.s22mag = []
        self.s22phase = []

#A class of microwave impedances that describe a DUT
class zparam:
    def __init__(self):
        self.z11 = []
        self.z21 = []
        self.z12 = []
        self.z22 = []

#A class of microwave admittances that describe a DUT
class yparam:
    def __init__(self):
        self.y11 = []
        self.y21 = []
        self.y12 = []
        self.y22 = []

#is_number checks to see if the passed in string is a number by seeing if the
```

```
#string can be converted to a complex number
#returns True if the string is a number. False if the string is not a number
def is_number(s):
    try:
        float(s)
        return True
    except ValueError:
        return False

#phase returns a list of phases in radians from the given scattering parameter list
def phase(S21):
    phase = []
    for a in S21:
        phase.append(cmath.polar(a)[1])
    return phase

# readS2P takes in an absolute filename and returns an appropriate s2p class
#representative of the file. All units are preserved such that if the S2P file has units dB and
#degrees the s2p class will have the same
def readS2P(fileName):
    fileHandle = open(fileName, 'r')
    fileList = fileHandle.readlines()
    fileHandle.close()
    s11mag = []
    s11phase = []
    s21mag = []
    s21phase = []
    s12mag = []
    s12phase = []
    s22mag = []
    s22phase = []
    freq = []
    toReturn = s2p()
    for line in fileList:
        lineSplit = line.split(" ")

        if is_number(lineSplit[0]) == True:
            freq.append(float(lineSplit[0]))
            s11mag.append(float(lineSplit[1]))
            s11phase.append(float(lineSplit[2]))
            s21mag.append(float(lineSplit[3]))
            s21phase.append(float(lineSplit[4]))
            s12mag.append(float(lineSplit[5]))
            s12phase.append(float(lineSplit[6]))
            s22mag.append(float(lineSplit[7]))
            s22phase.append(float(lineSplit[8]))

    toReturn.freq = freq
    toReturn.s11mag = s11mag
    toReturn.s11phase = s11phase
    toReturn.s21mag = s21mag
```

```
    toReturn.s21phase = s21phase
    toReturn.s12mag = s21mag
    toReturn.s12phase = s12phase
    toReturn.s22mag = s22mag
    toReturn.s22phase = s22phase

    return toReturn

#Computes the a list of magnitudes in dB from a scattering list
def magdB(S21):
    mag = []
    tempMag = 0
    for a in S21:
        tempMag = cmath.polar(a)[0]
        mag.append(20 * cmath.log10(tempMag))
    return mag

#Converts a scattering matrix to an impedance matrix given a source impedance and load
#impedance
def s2z(s2p, zsrc, zload):
    toReturn = zparam()
    i = 0
    s11Array = combineS21(s2p.s11mag, s2p.s11phase)
    s21Array = combineS21(s2p.s21mag, s2p.s21phase)
    s12Array = combineS21(s2p.s12mag, s2p.s12phase)
    s22Array = combineS21(s2p.s22mag, s2p.s22phase)

    while(i < len(s2p.s21mag)):
        s11 = s11Array[i]
        s21 = s21Array[i]
        s12 = s12Array[i]
        s22 = s22Array[i]

        smat = mat([[s11, s12], [s21, s22]])
        fmat = mat([[math.sqrt(zsrc), 0], [0, math.sqrt(zload)]])
        imat = mat([[1, 0], [0, 1]])

        Z = fmat * (imat + smat) * linalg.inv(imat - smat) * fmat
        toReturn.z11.append(Z[0, 0])
        toReturn.z12.append(Z[0, 1])
        toReturn.z21.append(Z[1, 0])
        toReturn.z22.append(Z[1, 1])

        i += 1
    return toReturn

#Calculates the admittance matrix from a given scattering matrix
def s2y(s2p, zsrc, zload):
    toReturn = yparam()

    i = 0
```

```
    s11Array = combineS21(s2p.s11mag, s2p.s11phase)
    s21Array = combineS21(s2p.s21mag, s2p.s21phase)
    s12Array = combineS21(s2p.s12mag, s2p.s12phase)
    s22Array = combineS21(s2p.s22mag, s2p.s22phase)

    while(i < len(s2p.s21mag)):
        s11 = s11Array[i]
        s21 = s21Array[i]
        s12 = s12Array[i]
        s22 = s22Array[i]

        smat = mat([[s11, s12], [s21, s22]])
        fmat = mat([[1 / (2 * math.sqrt(zsrc)), 0], [0, 1 / (2 * math.sqrt(zload))]])
        gmat = mat([[zsrc, 0], [0, zload]])
        imat = mat([[1, 0], [0, 1]])

        Y = linalg.inv(fmat) * linalg.inv(gmat) * linalg.inv(imat + smat) * (imat - smat) * fmat
        toReturn.y11.append(Y[0, 0])
        toReturn.y12.append(Y[0, 1])
        toReturn.y21.append(Y[1, 0])
        toReturn.y22.append(Y[1, 1])

        i += 1
    return toReturn

#Calculates the DUT's input impedance from a given impedance matrix and load impedance
def zin(zparam, zload):
    toReturn = []
    i = 0
    while(i < len(zparam.z11)):
        z11 = zparam.z11[i]
        z12 = zparam.z12[i]
        z21 = zparam.z21[i]
        z22 = zparam.z22[i]

        zin = z11 - (z12 * z21) / (z22 + zload)
        toReturn.append(zin)

        i += 1
    return toReturn;

#Calculates the input current for the DUT given a certain voltage and input impedance
def iin(vin, zinList):
    toReturn = []
    for zin in zinList:
        temp = vin / zin
        toReturn.append(abs(temp.real))
    return toReturn

#Calculates the load current for the DUT given a certain input voltage and scattering matrix
```

```
def iload(vin, S21):
    toReturn = []
    rload = 50;

    for a in S21:
        temp = vin * a / rload
        toReturn.append(abs(temp.real))
    return toReturn

#Calculates the power dissipated in the system given an input voltage and an input current
def pdis(vin, iinList):
    toReturn = []
    for iin in iinList:
        pdis = vin * iin
        toReturn.append(pdis)
    return toReturn

#Calculates the power dissipated in the DUT given a power dissipated in the system
#the load current and the load impedance
def pdisResonator(pdis, iload, zload):
    toReturn = []
    i = 0
    while(i < len(pdis)):
        pdisResonator = pdis[i] - (iload[i] * iload[i] * zload)
        toReturn.append(pdisResonator)
        i += 1
    return toReturn


#Combines the magnitude (in dB) and phase (in degrees) to a complex number
def combineS21(magDBS21, phaseAngleS21):
    i = 0;
    toReturn = []

    for magDB in magDBS21:

        mag = math.pow(10, (magDB / 20))
        ang = math.pi * phaseAngleS21[i] / 180
        temp = complex(mag * math.cos(ang), mag * math.sin(ang))
        toReturn.append(temp)
        i += 1
    return toReturn

#Converts a given power in dBm to a given power rms
def magtoP(mag):
    toReturn = 1e-3 * math.pow(10, mag / 20)

    return toReturn


#finds the resonance peak in a s2p class, returns the index of the list, the frequency
```

```
#and the s21 magnitude associated with the peak
def findPeak(s2p):
    toReturn = []
    i = 0
    maxS21 = max(s2p.s21mag)


    while(i < len(s2p.freq)):
        if(s2p.s21mag[i] == maxS21):
            toReturn.append(i)
            toReturn.append(s2p.freq[i])
            toReturn.append(s2p.s21mag[i])
        i += 1


    return toReturn

#Takes in a s2p class, a rms power input into the system, a source impedance and load impedance
#returns the DUT's motional impedance, the loss of the device, and the power dissipated in the
#DUT
def processFile(s2p, pin, zsrc, zload):

    peak = findPeak(s2p)
    rm = (zsrc + zload) * (math.pow(10, peak[2] / -20) - 1)

    vin = (math.pow(10,((peak[2])/10)))*(zload)*1e-3
    pDis = pow(vin/(rm +zload+zsrc), 2)*rm

    toReturn = []
    toReturn.append(rm)
    toReturn.append(max(s2p.s21mag))
    toReturn.append(pDis)
    return toReturn

if __name__ == "__main__":

    folder = \\MeasurementFolder\\'

    zsrc = 50
    zload = 50
    amp = 25
    resultArray = {}
    for root, subFolders, files in os.walk(folder):
        for filename in files:
            splitFile = filename.split('.')
            if(len(splitFile) > 1):
                if(splitFile[1] == 's2p'):
                    filePath = os.path.join(root, filename)
                    rootPiece = (root.split('\\'))

                    deviceName = rootPiece[7] + '-' + rootPiece[6] + '-' + rootPiece[5]
```

```
            s2pFile = readS2P(filePath)
            db = (filename.split('db'))[0]
            if(is_number(db)):
                inputP = float(db) + amp
                result = processFile(s2pFile, magtoP(inputP), zsrc, zload)
                result.append(inputP)
                if(deviceName in resultArray):
                    temp = resultArray[deviceName]
                else:
                    temp = []
                temp.append(result)
                resultArray[deviceName] = temp
print(resultArray)
sortedArray = {}
for index, row in resultArray.items():
    i = 0
    dataSet = {}
    x = []
    y = []
    rm = []
    pdis = []
    while (i < len(row)):
        dataSet[int(row[i][3])] = row[i]
        i += 1
    for i in sorted(dataSet.keys()):
        x.append(i)
        y.append(dataSet[i][1])
        pdis.append(dataSet[i][2])
        rm.append(dataSet[i][0])

    temp = DataFrame({'Input power': x, 'Output Power': y, 'Power Dis': pdis, 'Rm': rm})

    sortedArray[index] = temp
    print(x)
    plt.figure(1)
    plt.plot(x, y)
writer = ExcelWriter(ResultExcelSheet.xlsx')
for index, row in sortedArray.items():
    row.to_excel(writer, sheet_name=index, index=False)
writer.save()

plt.show()
```

C. Frequency shift PHP code

```
<?php
require('PHPExcel.php');
date_default_timezone_set('America/Chicago');

initializeExcel();

$startingPoint = "/MeasurementFolder";

$extension = ".s2p";

directoryScan($startingPoint);

//Scan through the input directory looking for s2p files
function directoryScan($directory){
	chdir($directory);
	$dirHandle = dir(".");
	$extension = ".s2p";
	$foundS2P = FALSE;
	while(($file = $dirHandle->read()) !== false){
		if(is_dir($file) AND $file != "." AND $file != ".."){
			directoryScan($file);
		}else if(substr($file, (strlen($file) - 4), 4) == $extension AND !$foundS2P){
			fileScan(".");
			$foundS2P = TRUE;
		}
	}
	chdir("..");

}

//Scan the directory and compose the frequency shift for each power level
function fileScan($directory){
	echo getCWD() ."\n";
	$longDir = getCWD();

	$waferMark = 'wafer';
	$dieMark = 'die';
	$waferPos = strpos($longDir, $waferMark);
	$longDir = substr($longDir, $waferPos, strlen($longDir) - waferPos);
	$slashPos = strpos($longDir, '/');
	$waferNumber = substr($longDir, strlen($waferMark), $slashPos - strlen($waferMark));

	$diePos = strpos($longDir, $dieMark);
	$longDir = substr($longDir, $diePos, strlen($longDir) - $diePos);
	$slashPos = strpos($longDir, '/');
	$dieNumber = substr($longDir, strlen($dieMark), $slashPos - strlen($dieMark));
	$deviceName = substr($longDir, $slashPos + strlen('/'), strlen($longDir) - $slashPos);

	echo "Wafer Number: ".$waferNumber . " Die Number: ".$dieNumber ."\n";
```

```
	echo "Device Name: ".$deviceName ."\n";

	$extension = ".s2p";
	$dirHandle = dir($directory);
	$flag = "#";
	while(($file = $dirHandle->read())!== false){
		$maximum = -120;
		$s2p = array();
		if(substr($file, (strlen($file) - 4), 4) == $extension){
			$fileHandle = fopen($directory.'/'.$file, 'r');
			$read = FALSE;
			while(($line = fgetcsv($fileHandle, ' ')) !== false){
				if($read){
					$freq = findFreq($line[0]);
					$mag = findMag($line[0]);

					$s2p[$freq] = $mag;
					if($mag > $maximum AND is_numeric($mag) AND
						!empty($mag) AND is_numeric($freq)){
						$maximum = $mag;
						$maximumFreq = $freq;
					}
				}else if($line[0][0] == $flag){
					$read = TRUE;
				}
			}
			$s2p['max']  = $maximum;
			$s2p['maxFreq'] = $maximumFreq;
			$s2p['name'] = substr($file, 0 , strlen($file) -4);
			if(is_numeric(substr($file,0,strlen($file) -7))){
				$s2p['loss'] = substr($file,0,strlen($file) - 7);
			}
			$s2p = findQ($s2p);
			if(!empty($s2p['loss'])OR $s2p['loss'] === '0'){
				$voltage = pow(10,((floatval($s2p['loss']) -13)/20));
				$watts = pow((($voltage)/(floatval($s2p['impedance']) + 50 +
					50)),2)*floatval($s2p['impedance']);
				$s2p['powerDelivered'] = (10*log10($watts))+30;

				$s2p['Vin'] = $voltage;
				$order[$s2p['loss']]=$s2p;
			}
		}
	}
	ksort($order);
	foreach ($order as $loss => $result){
		echo "Power: ".$result['Vin']."  Deviation [ppm]: " .$result['deviation'] ."
Impedance: ".$s2p['impedance']."\n";
	}
	echo "\n";
	writeExcel($order, $waferNumber, $dieNumber, $deviceName);
```

```
}

//Find the quality factor of a peak in a s21 signal
function findQ($s2p){
	$below		= TRUE;
	$threshold	= $s2p['max'] - 3;
	$prev		= 0;
	$prevFreq	= 0;
	$foundLeft = FALSE;
	$foundRight = FALSE;
	foreach($s2p as $freq => $mag){
		if($mag > $threshold AND $below AND !$foundLeft){
			$below		= FALSE;
			$slope		= ($mag - $prev)/($freq - $prevFreq);
			$leftPoint	= ($threshold - $prev)/$slope + $prevFreq;
			$foundLeft	= TRUE;
		}else if($mag < $threshold AND !$below AND !$foundRight){
			$below		= TRUE;
			$slope		= ($mag - $prev)/($freq - $prevFreq);
			$rightPoint	= ($threshold - $prev)/$slope + $prevFreq;
			$foundRight	= TRUE;
		}
		$prev		= $mag;
		$prevFreq	= $freq;
	}
	$delta = $rightPoint - $leftPoint;
	$center = ($rightPoint + $leftPoint)/2;
	$qualityFactor = $s2p['maxFreq'] / $delta;
	$s2p['q'] = $qualityFactor;
	$s2p['center'] = $center;
	$deviation = ($s2p['center'] - $s2p['maxFreq'])*1e6/$s2p['maxFreq'];
	$impedance = (pow(10,floatval($s2p['max'])/(-20)))*100 -100;
	$s2p['deviation']=$deviation;
	$s2p['impedance']=$impedance;

	return $s2p;
}

function findMag($line){
	$space = strpos($line, " ");
	$mag = substr($line,$space+1,strlen($line)-$space);
	$space = strpos($mag, " ");
	$mag = substr($mag,$space+1,strlen($mag)-$space);
	$space = strpos($mag, " ");
	$mag = substr($mag,$space+1,strlen($mag)-$space);
	$space = strpos($mag, " ");
	$mag = substr($mag,0,$space);
	return $mag;

}
```

```
function findFreq($line){
	$space = strpos($line, " ");
	$period = strpos($line, ".");
	$break = $space;
	if($space>$period){
//		$break = $period;
	}
	$freq = substr($line, 0, $break);
	return $freq;
}

//Write the results to an excel file
function writeExcel($order, $waferNumber, $dieNumber, $deviceName){
	$fileName = "/Users/bharrington/Dropbox/Multi-tether/reza.xls";
	$fileType = 'Excel5';
	$reader = PHPExcel_IOFactory::createReader($fileType);
	$phpExcelFile = $reader->load($fileName);

	$phpExcelFile->createSheet();

	$sheetCount = $phpExcelFile->getSheetCount();
	$phpExcelFile->setActiveSheetIndex($sheetCount-1);

	$phpExcelFile->getActiveSheet()->setTitle("$sheetCount");

	$phpExcelFile->getActiveSheet()->setCellValue('A1', 'Wafer');
	$phpExcelFile->getActiveSheet()->setCellValue('B1', $waferNumber);
	$phpExcelFile->getActiveSheet()->setCellValue('C1', 'Die');
	$phpExcelFile->getActiveSheet()->setCellValue('D1', $dieNumber);
	$phpExcelFile->getActiveSheet()->setCellValue('E1', 'Device');
	$phpExcelFile->getActiveSheet()->setCellValue('F1', $deviceName);

	$phpExcelFile->getActiveSheet()->setCellValue('A2', 'Power');
	$phpExcelFile->getActiveSheet()->setCellValue('B2', 'Vin');
	$phpExcelFile->getActiveSheet()->setCellValue('C2', 'Power Delivered');
	$phpExcelFile->getActiveSheet()->setCellValue('D2', 'Center Frequency');
	$phpExcelFile->getActiveSheet()->setCellValue('E2', 'Peak Frequency');
	$phpExcelFile->getActiveSheet()->setCellValue('F2', 'Quality Factor');
	$phpExcelFile->getActiveSheet()->setCellValue('G2', 'Loss');
	$phpExcelFile->getActiveSheet()->setCellValue('H2', 'Impedance');
	$phpExcelFile->getActiveSheet()->setCellValue('I2', 'Deviation');

	$count = 3;
	foreach ($order as $power => $s2p){
		$phpExcelFile->getActiveSheet()->setCellValue('A'.$count, $power);
		$phpExcelFile->getActiveSheet()->setCellValue('B'.$count, $s2p['Vin']);

		$phpExcelFile->getActiveSheet()->setCellValue('C'.$count,
			$s2p['powerDelivered']);
		$phpExcelFile->getActiveSheet()->setCellValue('D'.$count, $s2p['center']);
		$phpExcelFile->getActiveSheet()->setCellValue('E'.$count, $s2p['maxFreq']);
```

```
			$phpExcelFile->getActiveSheet()->setCellValue('F'.$count, $s2p['q']);
			$phpExcelFile->getActiveSheet()->setCellValue('G'.$count, $s2p['max']);
			$phpExcelFile->getActiveSheet()->setCellValue('H'.$count, $s2p['impedance']);
			$phpExcelFile->getActiveSheet()->setCellValue('I'.$count, $s2p['deviation']);
			$count++;
		}
		$writer = PHPExcel_IOFactory::createWriter($phpExcelFile, $fileType);
		$writer->save($fileName);
}

//Initialize the excel file
function initializeExcel(){
		$fileName = "data.xls";
		$fileType = 'Excel5';
		$reader = PHPExcel_IOFactory::createReader($fileType);
		$phpExcelFile = $reader->load($fileName);
		$writer = PHPExcel_IOFactory::createWriter($phpExcelFile, $fileType);

		$sheetCount = $phpExcelFile->getSheetCount();
		for($i=0;$i<$sheetCount; $i++){
			$phpExcelFile->removeSheetByIndex(0);
			$writer->save($fileName);
		}
		$writer->save($fileName);
}

?>
```

Chapter XI

BIBLIOGRAPHY

[1] W. Cady, "The piezo-electric resonator," in *Proceedings of the Institute of Radio Engineers*, 1922, vol. 6, pp. 83–114.

[2] J. R. Vig and F. L. Walls, "A review of sensor sensitivity and stability," in *Frequency Control Symposium and Exhibition, 2000. Proceedings of the 2000 IEEE/EIA International*, 2002, pp. 30–33.

[3] R. H. Olsson, J. G. Fleming, K. E. Wojciechowski, M. S. Baker, and M. R. Tuck, "Post-CMOS Compatible Aluminum Nitride MEMS Filters and Resonant Sensors," in *2007 IEEE International Frequency Control Symposium Joint with the 21st European Frequency and Time Forum*, 2007, pp. 412–419.

[4] V. Kaajakari, T. Mattila, A. Oja, J. Kiihamaki, and H. Seppa, "Square-Extensional Mode Single-Crystal Silicon Micromechanical Resonator for Low-Phase-Noise Oscillator Applications," *IEEE Electron Device Letters*, vol. 25, no. 4, pp. 173–175, Apr. 2004.

[5] K. Van Dyke, "The piezo-electric resonator and its equivalent network," *Proceedings of the Institute of Radio Engineers*, 1928.

[6] W. P. Mason, "Wave Filter," 20459911933.

[7] E. Hegazi, H. Sjoland, and A. Abidi, "A filtering technique to lower LC oscillator phase noise," *IEEE Journal of Solid-State Circuits*, vol. 36, no. 12, pp. 1921–1930, 2001.

[8] C. S. Lam, "A review of the recent development of MEMS and crystal oscillators and their impacts on the frequency control products industry," in *2008 IEEE Ultrasonics Symposium*, 2008, pp. 694–704.

[9] Z. Zvonar, P. Jung, and K. Kammerlander, *GSM Evolution Towards 3rd Generation Systems*. Kluwer Academic Publishers, 1999, p. 233.

[10] H. Holma and A. Toskala, *LTE for UMTS: Evolution to LTE-Advanced*. 2011, p. 70.

[11] H. Lavasani, R. Abdolvand, and F. Ayazi, “Low phase-noise UHF thin-film piezoelectric-on-substrate LBAR oscillators,” in *Micro Electro Mechanical Systems, 2008. MEMS 2008. IEEE 21st International Conference on*, 2008, pp. 1012–1015.

[12] F. Ayazi, S. Pourkamali, G. K. Ho, and R. Abdolvand, “High-Aspect-Ratio SOI Vibrating Micromechanical Resonators and Filters,” *Power*, pp. 676–679, 2006.

[13] D. Weinstein and S. A. Bhave, “Internal Dielectric Transduction of a 4.5 GHz Silicon Bar Resonator,” in *2007 IEEE International Electron Devices Meeting*, 2007, pp. 415–418.

[14] S. A. Bhave and R. T. Howe, “Internal electrostatic transduction for bulk-mode MEMS resonators,” in *Solid State Sensor, Actuator and Microsystems Workshop (Hilton Head 2004)*, 2004, pp. 6–10.

[15] G. Piazza, P. J. Stephanou, and A. P. Pisano, “Piezoelectric Aluminum Nitride Vibrating Contour-Mode MEMS Resonators,” *Journal of Microelectromechanical Systems*, vol. 15, no. 6, pp. 1406–1418, Dec. 2006.

[16] G. K. Ho and R. Abdolvand, “High-order composite bulk acoustic resonators,” *Proc. IEEE Micro Electro Mechanical Systems Conference, Japan, Jan*, pp. 791–794, 2007.

[17] R. Abdolvand, H. M. Lavasani, G. K. Ho, and F. Ayazi, “Thin-film piezoelectric-on-silicon resonators for high-frequency reference oscillator applications.,” *IEEE transactions on ultrasonics, ferroelectrics, and frequency control*, vol. 55, no. 12, pp. 2596–606, Dec. 2008.

[18] S. A. Bhave and R. T. Howe, “Silicon nitride-on-silicon bar resonator using internal electrostatic transduction,” in *The 13th International Conference on Solid-State Sensors, Actuators and Microsystems, 2005. Digest of Technical Papers. TRANSDUCERS ’05.*, 2005, vol. 2, no. K 9, pp. 2139–2142.

[19] H. Lavasani, R. Abdolvand, G. K. Ho, and F. Ayazi, “Low phase-noise UHF thin-film piezoelectric-on-substrate LBAR oscillators,” in *MEMS 2008*, 2008, pp. 1012–1015.

[20] H. M. Lavasani, R. Abdolvand, and F. Ayazi, “A 500MHz Low Phase-Noise AlN-on-Silicon Reference Oscillator,” *Optimization*, no. Cicc, pp. 599–602, 2007.

[21] F. Vanhelmont, P. Philippe, a. B. M. Jansman, R. F. Milsom, J. J. M. Ruigrok, and A. Oruk, “A 2 GHz Reference Oscillator incorporating a Temperature Compensated BAW Resonator,” in *2006 IEEE Ultrasonics Symposium*, 2006, pp. 333–336.

[22] A. Jaakkola, P. Rosenberg, S. Asmala, A. Nurmela, T. Pensala, T. Riekkinen, J. Dekker, T. Mattila, A. Alastalo, O. Holmgren, and K. Kokkonen, “Piezoelectrically transduced single-crystal-silicon plate resonators,” in *2008 IEEE Ultrasonics Symposium*, 2008, pp. 717–720.

[23] S. Humad, R. Abdolvand, G. K. Ho, G. Piazza, and F. Ayazi, “High frequency micromechanical piezo-on-silicon block resonators,” in *IEEE International Electron Devices Meeting 2003*, 2003, pp. 39.3.1–39.3.4.

[24] N. Sinha, J. Van der Spiegel, and G. Piazza, “Multi-frequency pierce oscillators based on piezoelectric AlN contour-mode MEMS resonators,” in *2008 IEEE International Frequency Control Symposium*, 2008, pp. 402–407.

[25] C. Zuo, N. Sinha, J. Van der Spiegel, and G. Piazza, “Multifrequency pierce oscillators based on piezoelectric AlN contour-mode MEMS technology,” *IEEE/ASME Journal of …*, vol. 19, no. 3, pp. 570–580, 2010.

[26] K. Wojciechowski and R. Olsson, “Single-chip precision oscillators based on multi-frequency, high-Q aluminum nitride MEMS resonators,” *Solid-State Sensors, …*, pp. 2126–2130, 2009.

[27] O. Mareschal, S. Loiseau, F. Verjus, L. Valbin, G. Lissorgues, R. Bouregba, G. Poullain, S. Saez, and C. Dolabdjian, “Modeling and fabrication of piezoelectric Aluminum Nitride resonator and its application in oscillators,” in *TRANSDUCERS 2009 - 2009 International Solid-State Sensors, Actuators and Microsystems Conference*, 2009, pp. 565–568.

[28] D. Ruffieux, F. Krummenacher, A. Pezous, and G. Spinola-durante, “Silicon Resonator Based 3.2 uW Real Time Clock With +-10 ppm Frequency Accuracy,” *IEEE Journal of Solid-State Circuits*, vol. 45, no. 1, pp. 224–234, 2010.

[29] G. Piazza, R. Abdolvand, G. K. Ho, and F. Ayazi, “Voltage-tunable piezoelectrically-transduced single-crystal silicon micromechanical resonators,” *Sensors and Actuators A: Physical*, vol. 111, no. 1, pp. 71–78, Mar. 2004.

[30] J. E.-Y. Lee, J. Yan, and A. a Seshia, “Study of lateral mode SOI-MEMS resonators for reduced anchor loss,” *Journal of Micromechanics and Microengineering*, vol. 21, no. 4, p. 045010, Apr. 2011.

[31] M. Rinaldi, A. Tazzoli, J. Segovia-Fernandez, V. Felmetsger, and G. Piazza, “High power and low temperature coefficient of frequency oscillator based on a fully anchored and oxide compensated AlN contour-mode MEMS resonator,” *2012 IEEE 25th International Conference on Micro Electro Mechanical Systems (MEMS)*, no. February, pp. 696–699, 2012.

[32] Z. Hao, A. Erbil, and F. Ayazi, “An analytical model for support loss in micromachined beam resonators with in-plane flexural vibrations,” *Sensors and Actuators A: Physical*, vol. 109, no. 1–2, pp. 156–164, 2003.

[33] Z. Hao and F. Ayazi, “Support loss in the radial bulk-mode vibrations of center-supported micromechanical disk resonators,” *Sensors and Actuators A: Physical*, vol. 134, no. 2, pp. 582–593, Mar. 2007.

[34] Y.-H. Park and K. C. Park, “High-Fidelity Modeling of MEMS Resonators—Part I: Anchor Loss Mechanisms Through Substrate,” *Journal of Microelectromechanical Systems*, vol. 13, no. 2, pp. 238–247, Apr. 2004.

[35] R. Abdolvand, G. K. Ho, A. Erbil, and F. Ayazi, “Thermoelastic damping in trench-refilled polysilicon resonators,” in *TRANSDUCERS, Solid-State Sensors, Actuators and Microsystems, 12th International Conference on, 2003*, 2003, vol. 1, pp. 324–327.

[36] B. H. Houston, D. M. Photiadis, M. H. Marcus, J. A. Bucaro, X. Liu, and J. F. Vignola, “Thermoelastic loss in microscale oscillators,” *Applied Physics Letters*, vol. 80, no. 7, pp. 1300 – 1302, 2002.

[37] R. Lifshitz and M. L. Roukes, “Thermoelastic Damping in Micro- and Nano-Mechanical Systems,” *Physical Review B*, vol. 61, no. 8, p. 10, Sep. 1999.

[38] R. N. Candler, H. Li, M. Lutz, W.-T. Park, A. Partridge, G. Yama, and T. W. Kenny, “Investigation of energy loss mechanisms in micromechanical resonators,” in *TRANSDUCERS ’03. 12th International Conference on Solid-State Sensors, Actuators and Microsystems. Digest of Technical Papers*, 2003, vol. 1, pp. 332–335.

[39] B. H. Houston, D. M. Photiadis, M. H. Marcus, J. A. Bucaro, X. Liu, and J. F. Vignola, “Thermoelastic loss in microscale oscillators,” *Applied Physics Letters*, vol. 80, no. 7, p. 1300, 2002.

[40] A. Duwel, R. N. Candler, T. W. Kenny, and M. Varghese, “Engineering MEMS Resonators With Low Thermoelastic Damping,” *Journal of Microelectromechanical Systems*, vol. 15, no. 6, pp. 1437–1445, Dec. 2006.

[41] W. Hemmert, D. Freeman, and J. White, “Air damping in laterally oscillating microresonators: A numerical and experimental study,” *Journal of Microelectromechanical Systems*, vol. 12, no. 5, pp. 557–566, Oct. 2003.

[42] Z. Hao, A. Erbil, and F. Ayazi, “An analytical model for support loss in micromachined beam resonators with in-plane flexural vibrations,” *Sensors and Actuators A: Physical*, vol. 109, no. 1–2, pp. 156–164, Dec. 2003.

[43] C. Zhang, G. Xu, and Q. Jiang, “Characterization of the squeeze film damping effect on the quality factor of a microbeam resonator,” *Journal of Micromechanics and Microengineering*, vol. 14, no. 10, pp. 1302–1306, Oct. 2004.

[44] A. K. Pandey and R. Pratap, “Effect of flexural modes on squeeze film damping in MEMS cantilever resonators,” *Journal of Micromechanics and Microengineering*, vol. 17, no. 12, pp. 2475–2484, Dec. 2007.

[45] H. A. C. Tilmans and R. Legtenberg, “Electrostatically driven vacuum-encapsulated polysilicon resonators,” *Sensors and Actuators A: Physical*, vol. 45, no. 1, pp. 67–84, Oct. 1994.

[46] Z. Hao and B. Liao, “An analytical study on interfacial dissipation in piezoelectric rectangular block resonators with in-plane longitudinal-mode vibrations,” *Sensors and Actuators A: Physical*, vol. 163, no. 1, pp. 401–409, Sep. 2010.

[47] M.-A. Dubois and P. Muralt, "Properties of aluminum nitride thin films for piezoelectric transducers and microwave filter applications," *Applied Physics Letters*, vol. 74, no. 20, p. 3032, 1999.

[48] L. Khine and M. Palaniapan, "Effect of structural thickness, anchor length and number of anchors on performance of micromechanical bulk-mode resonators," *Electronics Letters*, vol. 45, no. 1, p. 37, 2009.

[49] J. A. Judge, D. M. Photiadis, J. F. Vignola, B. H. Houston, and J. Jarzynski, "Attachment loss of micromechanical and nanomechanical resonators in the limits of thick and thin support structures," *Journal of Applied Physics*, vol. 101, no. 1, p. 013521, 2007.

[50] Z. Hao and F. Ayazi, "Support loss in the radial bulk-mode vibrations of center-supported micromechanical disk resonators," *Sensors and Actuators A: Physical*, vol. 134, no. 2, pp. 582–593, Mar. 2007.

[51] H. P. Loebl, C. Metzmacher, R. F. Milsom, P. Lok, F. van Straten, and A. Tuinhout, "RF Bulk Acoustic Wave Resonators and Filters," *Journal of Electroceramics*, vol. 12, no. 1/2, pp. 109–118, Jan. 2004.

[52] C.-J. Chung, Y.-C. Chen, C.-C. Cheng, C.-L. Wei, and K.-S. Kao, "Influence of surface roughness of Bragg reflectors on resonance characteristics of solidly-mounted resonators," *IEEE Transactions on Ultrasonics, Ferroelectrics and Frequency Control*, vol. 54, no. 4, pp. 802–808, Apr. 2007.

[53] G. Rogers, "A diameter 300 µm Bragg reflector for acoustic isolation of resonant micro-actuators," *Journal of Micromechanics and Microengineering*, vol. 21, no. 4, p. 042001, Apr. 2011.

[54] M. Pandey, R. B. Reichenbach, A. T. Zehnder, A. Lal, and H. G. Craighead, "Reducing Anchor Loss in MEMS Resonators Using Mesa Isolation," *Journal of Microelectromechanical Systems*, vol. 18, no. 4, pp. 836–844, Aug. 2009.

[55] G. Piazza, V. Felmetsger, P. Muralt, R. H. Olsson III, and R. Ruby, "Piezoelectric aluminum nitride thin films for microelectromechanical systems," *MRS Bulletin*, vol. 37, no. 11, pp. 1051–1061, Nov. 2012.

[56] M. Wasilik and A. P. Pisano, "Low frequency process for silicon on insulator deep reactive ion etching," in *SPIE*, 2001, pp. 462–472.

[57] K.-L. Chen, H. Chandrahalim, A. B. Graham, S. A. Bhave, R. T. Howe, and T. W. Kenny, "Epitaxial Silicon Microshell Vacuum-Encapsulated CMOS-Compatible 200 MHz Bulk-Mode Resonator," in *2009 IEEE 22nd International Conference on Micro Electro Mechanical Systems*, 2009, pp. 23–26.

[58] C. T.-C. Nguyen, "High-Q micromechanical oscillators and filters for communications," in *Proceedings of 1997 IEEE International Symposium on Circuits and Systems. Circuits and Systems in the Information Age ISCAS '97*, 2002, vol. 4, pp. 2825–2828.

[59] D. T. Blackstock, *Fundamentals of Physical Acoustics*. New York: John Wiley & Sons, 2000, p. 47.

[60] V. Taş, S. Olcum, M. D. Aksoy, and A. Atalar, "Reducing anchor loss in micromechanical extensional mode resonators.," *IEEE transactions on ultrasonics, ferroelectrics, and frequency control*, vol. 57, no. 2, pp. 448–54, Jan. 2010.

[61] P. C. Magnusson, A. Weisshaar, V. K. Tripathi, and G. C. Alexander, *Transmission lines and wave propagation*, 4th ed. Boca Raton: CRC, 2000, p. 519.

[62] F. Ihlenburg, *Finite element analysis of acoustic scattering*, vol. 65, no. 7. Springer Verlag, 1998, pp. 1–20.

[63] J.-P. Berenger, "A perfectly matched layer for the absorption of electromagnetic waves," *Journal of Computational Physics*, vol. 114, no. 2, pp. 185–200, Oct. 1994.

[64] D. S. Bindel and S. Govindjee, "Elastic PMLs for resonator anchor loss simulation," *International Journal for Numerical Methods in Engineering*, vol. 64, no. 6, pp. 789–818, Oct. 2005.

[65] H. M. Lavasani, W. Pan, B. P. Harrington, R. Abdolvand, and F. Ayazi, "A 76 dBΩ 1.7 GHz 0.18 um CMOS Tunable TIA Using Broadband Current Pre-Amplifier for High Frequency Lateral MEMS Oscillators," *IEEE Journal of Solid-State Circuits*, vol. 46, no. 1, pp. 224–235, 2011.

[66] J. T. M. van Beek and R. Puers, "A review of MEMS oscillators for frequency reference and timing applications," *Journal of Micromechanics and Microengineering*, vol. 22, no. 1, p. 013001, Jan. 2012.

[67] H. M. Lavasani, W. Pan, B. P. Harrington, R. Abdolvand, and F. Ayazi, "Electronic Temperature Compensation of Lateral Bulk Acoustic Resonator Reference Oscillators Using Enhanced Series Tuning Technique," *IEEE Journal of Solid-State Circuits*, vol. 47, no. 6, pp. 1381–1393, Jun. 2012.

[68] S. Rai, Y. Su, W. Pang, R. Ruby, and B. Otis, "A digitally compensated 1.5 GHz CMOS/FBAR frequency reference.," *IEEE transactions on ultrasonics, ferroelectrics, and frequency control*, vol. 57, no. 3, pp. 552–61, Mar. 2010.

[69] A. K. Samarao, G. Casinovi, and F. Ayazi, "Passive TCF compensation in high Q silicon micromechanical resonators," in *2010 IEEE 23rd International Conference on Micro Electro Mechanical Systems (MEMS)*, 2010, pp. 116–119.

[70] "IEEE Standard Definitions of Physical Quantities for Fundamental Frequency and Time Metrology — Random Instabilities." IEEE-SA Standards Board, 1999.

[71] D. Leeson, "A simple model of feedback oscillator noise spectrum," *Proceedings of the IEEE*, no. February, pp. 329–330, 1966.

[72] V. Kaajakari, T. Mattila, A. Lipsanen, and A. Oja, “Nonlinear mechanical effects in silicon longitudinal mode beam resonators,” *Sensors and Actuators A: Physical*, vol. 120, no. 1, pp. 64–70, Apr. 2005.

VITA

Brandon Paul Harrington

Candidate for the Degree of

Doctor of Philosophy

Thesis: PERFORMANCE ENHANCEMENT OF MICROMACHINED THIN-FILM PIEZOELECTRIC-ON-SILICON LATERAL-EXTENSIONAL RESONATORS THROUGH SUBSTRATE AND SUPPORT TETHER MODIFICATIONS

Major Field: Electrical Engineering

Biographical:

Education:

Completed the requirements for the Doctor of Philosophy in Electrical Engineering at Oklahoma State University, Tulsa, Oklahoma in July 2013.

Completed the requirements for the Master of Science in Electrical and Computer Engineering at Georgia Institute of Technology, Atlanta, Georgia in May 2008.

Completed the requirements for the Bachelor of Science in Computer Engineering at Georgia Institute of Technology, Atlanta, Georgia in May 2005.

Experience:

Senior MEMS Engineer, Knowles Electronics, June 2012 – Current

Graduate Research Assistant, Oklahoma State University, May 2008 – June 2012

Electrical Engineer, Microelectronics Research Center, July 2005 – May 2008